UNIONE EUROPEA
Fondo Sociale Europeo

Ministero dell'Università e della Ricerca

PON RICERCA E INNOVAZIONE 2014 - 2020

UNIVERSITÀ DEGLI STUDI FIRENZE
Da un secolo, oltre.

NTNU
Norwegian University of Science and Technology

DOTTORATO DI RICERCA IN
CIVIL AND ENVIRONMENTAL ENGINEERING

CICLO XXXVII - PON ex DM1061

THE USE OF LOW ENTHALPY GEOTHERMAL ENERGY THROUGH THE INSTALLATION OF MICROPILES

Settore Scientifico Disciplinare
CEAR-05 /A GEOTECNICA

Dottoranda

Dott.ssa Melissa Fabiola Yozy Kepdib

Supervisori

Prof. Johann Antonio Facciorusso
Prof. Claudia Madiai
Prof. Rao Martand Singh

Coordinatore

Prof. Luca Solari

To my beloved children

Believe in yourself

Acknowledgements

This PhD journey has been one full of hard work, late nights, and moments of doubt, but also growth, learning, and many good memories. It would not have been possible without the support, guidance, and encouragement of many individuals and institutions to whom I am deeply grateful.

Firstly, I would like to express my sincere gratitude to the Italian Ministry of University and Research (MUR) for funding this work through the National Operative Plan (PON) program (D.M. No. 1061, 2021).

This research was carried out in collaboration between the University of Florence in Italy and the Norwegian University of Science and Technology (NTNU). I thank both institutions for granting me the opportunity to pursue this PhD. I am grateful to my professors and supervisors at both universities for their continuous guidance and insightful feedback.

I extend heartfelt thanks to the companies that contributed to this research with their technical expertise, materials, or collaboration: Axer Srl (Italy), Friedr. Ischebeck GmbH (Germany), Fundamentering AS (Norway), Separatus AG (Switzerland), Jansen AG (Switzerland), and Sisgeo (Italy).

To my parents, Mr Abel and Mrs Henriette KEPDIB, my siblings, family, friends, colleagues, and acquaintances, thank you for your continuous support, for the words of encouragement, for listening ears, for standing by me when things seemed to fall apart.

Throughout this journey, I met wonderful people and expanded my professional and personal network. I am thankful for your encouragement and support.

To you, the reader, thank you for your interest. May you find insight and inspiration within these pages.

Above all, I thank God Almighty for His continuous strength, made perfect in my weaknesses. His Grace has been and continues to be sufficient for me.

May this research contribute to the fields of foundation design, energy micropiles, energy geotechnics, and geothermal energy, and support the broader goal of a more sustainable future.

Table of contents

List of symbols

CPT	Cone penetrometer test
DIN	Deutsches Institut für Normung
IGU	Injection gravitaire unitaire
IRS	Injection répétée et sélective
RTD	Resistant temperature detectors
SLS	Serviceability limit state
ULS	Ultimate limit state
UNEP	United Nations Environment Programme
Q	Actions
R	Resistances
X	Material properties
γ_A	Partial factors applied to actions
γ_X	Partial factors applied to the materials X
γ_R	Partial factors applied to the resistances R
$\tan \varphi'$	Angle of shearing resistance
c'	Cohesion intercept
c_u	Undrained shear strength
γ	Unit weight
γ_b	Partial factor for base resistance
γ_s	Partial factor for resistance of shaft in compression
γ_t	Partial factor for total resistance
$\gamma_{s,t}$	Partial factor for resistance of shaft in tension
Q_{lim}	Total bearing capacity of pile

Q_b	Ultimate base resistance of pile
Q_s	Ultimate base resistance of pile
q_s	Unit shaft resistance
L	Pile length
α	Adhesion coefficient
σ_h'	Effective horizontal stress
σ'_{v0}	Effective vertical stress
k	Empirical coefficient of horizontal stress
δ	Friction angle at the pile soil interface
φ	Soil friction angle
p_g	Grouting pressure
p_L	Limit pressure from Menard pressuremeter test
D_s	Effective diameter
D_d	Perforation diameter
L_s	Length of the injected portion of the micropile
s	Shear resistance at the interface between the soil and the injected portion of the pile
s_{PT}	Standard penetrometer (SPT) blow count
$Q_{d,GEO}$	Design geotechnical bond capacity
$Q_{d,STR}$	Design structural load
A_b	Grout-steel interface area
A_s	Steel area
$q_{a,bond}$	Grout-to-ground bonding strength
$q_{a,y}$	Yielding stress of reinforcement

γ_m	Safety factor for structural failure
E_A	Action effect
C_A	Limiting settlement
w_s	Settlement
w_g	Group settlement
Q	Applied power
A	Area
ΔT	Temperature difference
k	Thermal conductivity
T	Temperature
T_{in}	Inlet temperature
T_{out}	Outlet temperature
m	Mass flow rate
C	Specific heat capacity
α	Thermal diffusivity
T_g	Undisturbed ground temperature
v	Velocity
E	Young's modulus
A	Cross-sectional area
δl_M	Deformation due to the mechanical load
ε_{T-Free}	Free axial thermal strain in the absence of restraint
α_c	Coefficient of isotropic thermal expansion or contraction of concrete
ΔT	Temperature difference
ε_{T-Rstr}	Restrained axial strains

P_T	Thermally induced axial load
σ_T	Thermally induced axial stress
ε_{T-Obs}	Observed axial strain
u	Fluid velocity
p	Pressure field [Pa]
μ	Dynamic viscosity
∇	Gradient operator
·	Dot product
g	Gravity
τ	Viscous stress tensor
F	Volume force vector
S	Strain-rate tensor
Q_{ted}	Thermoelastic damping
S	Second Piola-Kirchhoff stress tensor
t_b	Hollow tube thickness
t_{pw}	Partition wall thickness
h_{pw}	Partition wall height
X	Parameter
$\bar{\bar{Y}}_{X_i}$	Average response at level i
$Y_{X_{i,j}}$	Response from the j^{th} experiment with parameter X at level i
n_i	Number of experiments at level i
ΔX	Range of parameter X
Δ	Davisson offset
P_{ag}	Allowable group capacity of pile

P_a	Allowable capacity of a single isolated pile
N	Number of piles
η	Pile group efficiency factor
m	Number of rows of piles in a group
n	Number of piles per row in a group
t_0	Initial/reference time
t_i	Elapsed time
R_0	Raw reading at time t_0
R_i	Raw reading at time t_i
S_0	Strain reading at time t_0
S_i	Strain reading at time t_i
G	Strain gauge factor

List of figures

List of tables

Abstract

The global drive to decarbonize the built environment has intensified interest in renewable heating and cooling technologies, particularly in dense urban settings and retrofit projects. This doctoral research investigates the application of energy micropiles as a combined solution for structural support and low-enthalpy geothermal heating and cooling. The study combines full-scale field experiments with numerical modeling to evaluate both the thermal performance and the thermo-mechanical behavior of energy micropiles under realistic operating conditions.

Six energy micropiles were installed in saturated soft and sensitive clay at a test site at the NTNU Dragvoll campus in Trondheim, Norway. Each micropile was 15 meters long and had a diameter of 240 mm or 300 mm. The micropiles were equipped with either a corrugated coaxial pipe or a split-pipe heat exchanging loop. Thermal tests were performed by circulating a heat transfer fluid through the pipes at a temperature of 25 ± 2 °C for several days. Mechanical tests, hereafter referred to as creep tests, involved applying a constant tensile load of 550 kN, while thermo-mechanical tests combined both thermal and mechanical loading conditions.

The thermal power outputs ranged from 32.91 to 80.41 W/m, confirming that micropiles can deliver efficient thermal performance and represent a viable solution for heating and cooling buildings. The coefficients of performance (COP) varied between 1.73 and 3.87, which are lower than typical values reported for geothermal systems (3- 5). This reduced efficiency is attributed to the use of an air-source heat pump during testing, rather than a geothermal heat pump, and to the oversizing of the heat pump for single micropile operation. These factors increased the compressor workload and energy consumption, thereby lowering the COP. An air-source heat pump was used solely for test purposes, hence the COP values obtained should not be considered for geothermal systems. Under real operating conditions, a geothermal heat pump would be employed.

During the thermo-mechanical test on micropile 5 and the thermal test on micropile 6, expansive strains were observed along most of the micropile length, representing between 53.54% and 65.66% of the free thermal strains. The maximum thermally induced compressive stress, calculated from the blocked strains, was 132.42 kPa/°C, which represented 3% of the grout´s compressive strength. However, two sensors recorded contractive strains which led to the development of localized thermally induced tensile stresses during heating. This unusual behavior is hypothesized to result from sensor malfunction. Nevertheless, given the complex behavior of clay, further investigation is recommended. Additionally, micropile head

displacement was observed to increase rapidly at the start of thermal loading and later stabilized with temperature. The thermally induced displacement of 3 mm was approximately three times larger than those caused by creep alone (0.94 mm). Nevertheless, the total displacement was lower than 10 mm which is satisfactory for most building and civil engineering structures provided that the group settlement is not excessive. Upon unloading and cooling, strains values returned to near-zero suggesting a predominantly thermo-elastic response of the micropile under the tested conditions.

To complement the findings of the experimental campaign, a numerical parametric study was conducted. The Taguchi method, a statistical approach for design optimization, was adopted to systematically explore the influence of key design variables. An orthogonal array was used to efficiently plan the simulation matrix, significantly reducing the number of required simulations. The level average analysis method was employed to assess the relative impact of each factor and to identify the optimal configuration. The results highlight that micropile length, grout thermal conductivity, and fluid flow rate are the most influential factors affecting the system performance.

The practical feasibility of energy micropiles was further validated through a realistic case study involving the simulation of a foundation system for a heating-dominated building located in the Nordic region. In the case study, 48 micropiles were designed to serve both as structural support and as a geothermal heat exchanger. A detailed numerical model was developed using COMSOL Multiphysics, incorporating local climatic data, building heat demand, and subsoil thermal properties. The results showed that the energy micropile system could meet approximately 17.06% of the building's monthly heating demand, highlighting its potential as a supplemental low-carbon energy source. Furthermore, a 30-year life-cycle cost analysis was performed, comparing the energy micropile system with conventional electric heating. The analysis revealed that, despite higher initial investment costs, long-term operating expenses are comparable, with potential benefits in terms of energy efficiency and environmental impact.

In conclusion, this research demonstrates the technical and economic feasibility of energy micropiles as a suitable solution for heating and cooling buildings, particularly in space-constrained dense urban environment or retrofit applications. However, several aspects, such as long-term thermal performance and thermo-mechanical behavior in sensitive clays, groundwater variation, ground temperature changes, cyclic loading effects, and group interactions between micropiles, require further investigation to inform reliable and efficient design strategies.

1. Introduction

1.1. Problem statement

Buildings account for nearly 32% of global energy demand (IEA, 2024; UNEP, 2025), with heating and cooling representing about half of the demand (IEA, 2023). According to the United Nations Environment Programme (UNEP), the building sector is responsible for 34% of energy related CO_2 emissions. As the built environment continues to grow, especially in urban areas, there is a corresponding rise in energy demand for space heating and cooling. The global transition towards sustainable energy systems has placed increasing emphasis on the development of efficient, low-carbon heating and cooling technologies. The European Union in its energy performance of buildings directive, aims to achieve a fully decarbonised building stock by 2050, that is all buildings should meet « nearly zero-energy buildings » requirements by 2050. The United Nations Environment Programme (UNEP, 2021) recognizes building retrofitting as an important measure to the decarbonisation of buildings. In fact, deep retrofitting of buildings, alongside the construction of highly efficient buildings could reduce cooling intensity by 25% by 2030 and 50% by 2050. As the urgency to decarbonize the building sector intensifies, low enthalpy geothermal energy is emerging as a reliable and sustainable source of low-carbon heating and cooling.

Low-enthalpy geothermal systems exploit the relatively stable temperatures of the shallow subsurface - typically up to 200 meters deep - to exchange heat with the ground. While borehole heat exchangers are the most widely used geothermal technology, they often involve high drilling costs, spatial constraints in urban environments, and complex permitting processes. As an alternative, energy geostructures, such as energy piles, sheet piles, diaphragm walls and tunnels, were introduced in the 1980s. These systems integrate conventional structural elements with thermal exchange functionality by embedding heat exchanger pipes within the concrete, enabling the geostructure to act simultaneously as a structural support and a ground-source heat exchanger (Brandl, 2006). The installation of energy geostructures requires no additional drilling resulting in both economic and environmental benefits. However, most energy geostructures are designed for new constructions and may not be suitable in retrofitting projects. In such cases, energy micropiles offer a practical and efficient alternative.

Micropiles, typically characterized by diameters less than 300 mm, are particularly well-suited for sites with limited access, existing infrastructure, environmentally sensitive surroundings, or complex subsurface conditions. Their installation causes minimal ground disturbance and is adaptable to a wide range of soil types, including soft soils. Originally developed for providing load-bearing capacity and foundation reinforcement, micropiles have recently gained attention as dual-purpose systems for both structural support and heat exchange, where they are referred to as energy micropiles. As with other energy geostructures, the design of energy micropiles must account not only for structural requirements but also for thermal performance and thermo-hydro-mechanical behavior. From a thermal design perspective, achieving efficient heat exchange at minimal cost requires careful consideration of numerous parameters. These include the thermal properties of the ground, concrete, pipes, and circulating fluid; the geometry and configuration of the pile and embedded pipes; and the operational parameters such as fluid flow rate and inlet temperature. Ideally, the integration of energy functionality should not require significant modification of the original geotechnical and structural design of the micropile. However, the introduction of thermal loading inevitably alters the mechanical response of the system. Heat exchange between the ground and the structure induces temperature fluctuations within the pile, which can lead to thermal strains and stresses, vertical displacements (heave or settlement), and axial expansion or contraction of the micropile. Additionally, there may be changes in ground water pressure and ground temperature. It is therefore critical that the thermal function does not compromise the structural integrity or exceed design limits.

While extensive research has been conducted on energy piles, including their thermal performance and coupled thermo-mechanical behavior (Akrouch et al., 2014; Amatya et al., 2012; Batini et al., 2015; Cecinato & Loveridge, 2015a; Faizal et al., 2016; Fang et al., 2022; Gao et al., 2008; Mimouni & Laloui, 2015; Olgun et al., 2015; Rotta Loria & Laloui, 2017, 2018; Suryatriyastuti et al., 2013; Sutman et al., 2015), comparatively limited research has focused on energy micropiles. Due to their smaller diameter and end-bearing capacity, the behavior of micropiles under thermal and mechanical loading may be different from that of conventional energy piles (Ronchi et al., 2018). Although a number of studies have explored some aspects of energy micropiles (Casagrande et al., 2022; Jalaluddin et al., 2011; Lupattelli et al., 2023; Ronchi et al., 2018), some knowledge gaps remain. Most existing studies focus on micropiles under compression loads. To the best of our knowledge, no published research has yet addressed the performance energy micropiles subjected to tensile loads, as would be the case for uplift applications. Furthermore, the current body of literature has largely concentrated on Type A and Type B micropiles equipped with conventional U-shaped heat exchanger pipes. To the best of our knowledge, there are no studies investigating Type E self-drilling energy micropiles in saturated sensitive clay. Innovative pipe configurations such as the corrugated coaxial pipe and the split-pipe system, with the potential of enhancing thermal performance by improving heat transfer efficiency have not yet been investigated.

1.2. Scope and research

With a growing demand for renewable heating and cooling technologies, energy micropiles offer a promising and cost-effective solution, especially in densely populated areas where energy boreholes and other energy geostructures may not be feasible. Despite their potential, the behavior and performance of energy micropiles remain underexplored, particularly in soft soil conditions and mechanical tensile loads. The present thesis aims to address this gap by evaluating both the thermal efficiency and the thermo-mechanical response of Type E self-drilling micropiles equipped with innovative heat exchanger pipes, including the split-pipe and the coaxial corrugated pipe. These configurations are investigated for the first time in the context of energy micropiles, piles and energy geostructures. The research focuses on quantifying thermal power output under heating conditions, the coefficient of performance, the strains and axial stresses along the micropile, and vertical displacement of the micropile, during thermal test, creep test and thermo-mechanical test. Additionally, a comprehensive parametric study is conducted to evaluate the influence of design variables such as flow rate, grout body dimensions, pipe configuration, and ground thermal conductivity, on the thermal performance. To further demonstrate the feasibility of energy micropiles for heating buildings in the Nordic region, a realistic project scenario was considered, with system performance evaluated through numerical modeling. This was followed by a 30-year cost analysis comparing energy micropiles to conventional electric heaters. Through this work, the thesis aims to address current knowledge gaps and support the development of design guidelines for energy micropiles, enabling their broader application in the transition towards low-carbon, energy-efficient buildings.

1.3. Methodology

Assessing the thermal performance and the thermo-mechanical behavior of energy micropiles requires comprehensive experimental and numerical investigation. Six Type E self-drilling energy micropiles were installed at a test site in Dragvoll, Trondheim, Norway, where saturated soft clay is predominant. Each micropile was 15 m long, with diameters of 240 mm or 300 mm, and equipped with one of two pipe configurations: a spilt-pipe or a corrugated coaxial pipe, through which the heat exchange fluid was circulated. The experimental campaign was divided into creep test, thermal only and thermo-mechanical test series. Four micropiles denoted as micropiles 1,5,6, and 3 were tested in this order. A preliminary pull-out load test was conducted on a reference micropile (micropile 1) to assess the ultimate capacity of the micropiles. A second pull-out test was performed on micropile 5, followed by creep test at a tensile load of 550 kN and thermo-mechanical testing during which both mechanical and thermal loads were applied to the micropile. Micropiles 6 and 5 were tested in thermal loading only. Thermal loading consisted of circulating the heat transfer fluid at a temperature of 25 ± 2 °C though the plastic pipes which were connected to a 2.3 kW exhaust air heat pump. The micropiles were tested for an average duration of 05 days during which temperatures stabilized. Each micropile, except the reference micropile, was instrumented with thermistors and strain gauges along its length and resistance temperature detectors at the inlet and outlet. Flow rates, inlet and outlet temperatures, and electric power consumption were continuously recorded to determine the thermal output and coefficient of performance. Ground temperature and pore water pressure at varying distances from the micropile were intended to be monitored; however, this was not possible during the testing period reported in this thesis and will therefore not be discussed. To extend the findings beyond the experimental setup, a numerical model was developed using COMSOL Multiphysics. The model was used to conduct parametric analyses involving key parameters such as grout conductivity, pipe geometry, fluid flow rate, micropile geometry, to provide insights into ways to optimize efficiency of the system. Furthermore, the applicability of energy micropiles for heating buildings was demonstrated through a realistic case study in which the numerical model was used to assess the performance of the system in heating buildings in heating dominated countries like Norway. Additionally, the energy micropile system was compared with conventional electric heaters. Together, this methodology provides both an in-depth understanding of the behavior and performance energy micropiles and practical insights for future design applications.

1.4. Thesis outline

This thesis is organized into six chapters. Building on the background, objectives and methodology outlined above, it proceeds as follows. Chapter 2 presents a comprehensive literature review on the classification, design principles, and engineering aspects of micropiles, followed by a detailed discussion on energy geostructures. Emphasis is placed on the design, thermal behavior, and thermo-mechanical behavior of energy micropiles, as well as recent technological advancements. The chapter concludes with a synthesis of existing knowledge and the identification of current research gaps. Chapter 3 describes the experimental investigation, detailing the site conditions, materials, instrumentation setup, installation procedures, testing program, and presents the results. Measurements of fluid inlet and outlet temperatures, micropile temperature distribution, strains, and displacements are analyzed to evaluate the thermal performance and the thermo-mechanical behavior of the micropiles. Chapter 4 outlines the numerical modelling approach and key assumptions adopted for the parametric analysis of the thermal performance of energy micropiles equipped with a split-pipe system. The simulations are performed using COMSOL Multiphysics, and the parametric study is conducted using the Taguchi method. Chapter 5 presents a practical case study demonstrating the application of energy micropiles for both foundation support and heating of a building. It also includes a comparative life-cycle cost analysis between the energy micropile system and conventional electric heater. Finally, chapter 6 summarizes the key findings of the research, discusses their broader implications for the design and implementation of energy micropiles in geotechnical engineering practice, and proposes recommendations for future research directions.

2. Energy micropiles

2.1. Introduction

During the 20th century and especially during the second world war, the historic buildings and monuments of Italy sustained damage with time. In response to the demand for innovative techniques for underpinning of these structures, an Italian specialty contractor called Fondedile, for whom Dr. Fernando Lizzi was the technical director, developed the *palo radice*, or root pile. The *palo radice* was a small-diameter, drilled, cast-in-place, lightly reinforced, grouted pile. This *palo radice* has evolved over the years and today is what we call "Micropiles". Initially, micropiles were developed for underpinning and retrofitting existing structures especially in dense urban environments and challenging geological conditions, such as karst formations and restricted areas. Starting in 1957, evolving engineering demands led to the development of reticulated root pile systems utilized for various purposes, including slope stabilization, reinforcement of quay walls, protection of buried structures, and other soil and structure support and ground reinforcement applications (Sabatini et al., 2005).

Micropiles are slender replacement piles typically less than 300 mm in diameter (Bruce et al., 1997; Sabatini et al., 2005; Tomlinson & Woodward, 2015; Viggiani et al., 2012), although small displacement piles are sometimes considered as micropiles (Tomlinson & Woodward, 2015). These small-diameter piles are generally constructed by drilling a borehole, inserting steel reinforcement, and filling the hole with grout, a cementitious material. The use of advanced drilling and grouting techniques enables high grout-bond values around micropiles, which significantly enhance their load-bearing capacity. The steel reinforcement, occupying a substantial portion of the borehole's diameter, serves as the primary load-bearing element, while the grout ensures efficient load transfer through friction between the soil and steel. This configuration allows micropiles to sustain very high loads. The axial capacities are in the range of 50 – 500 kN and up to 1000 kN when installed using pressure grouting techniques (Tomlinson & Woodward, 2015), with minimal movement (Bruce et al., 1997). High compression loads of up to 5000 kN have been recorded (Bruce et al., 1997). Hence, the small size of micropiles do not confer to them a low structural capacity like in the case of conventional piles where loads are predominantly borne by concrete (Bruce et al., 1997).

Micropile construction (Figure 2.1) involves three primary steps: drilling, placing reinforcement, and grouting, which should be performed continuously and efficiently to prevent adverse effects and maintain soil's integrity. The casing may be completely removed after the micropile is completed or it may be left in the soil. The chosen drilling technique must ensure stable borehole dimensions with minimal disruption, considering soil characteristics, existing structures, and project constraints. Grouting, typically with neat cement-water mixes of water-cement ratio of 0.4 - 0.5, significantly impacts micropile capacity and protection against corrosion. Additives like sand or high-range water reducers may be used to enhance grout properties and pumpability. Bentonite is used sparingly as it can weaken grout strength. Drinkable water is used for grouts to minimize corrosion risks to reinforcement. Properly manufactured grouts can achieve compressive strengths of 28 to 35 MPa, transferring loads, forming part of the load-bearing section, and protecting steel from corrosion. The grout must exhibit appropriate fluidity, strength, stability, pumpability, and durability. The grouting method should be carefully chosen as it significantly influences the grout/ground bond strength. The structural strength of micropiles relies on high-capacity steel elements such as concrete reinforcing steel bars (rebars), continuous-thread steel bars, continuous-thread hollow-core steel bars, steel pipe casing, and composite reinforcement. Reinforcement is installed either before grouting or inserted into the grout-filled borehole before removing temporary support. It is essential that reinforcement is free from contaminants like soil and mud to ensure proper grout adhesion and bond development.

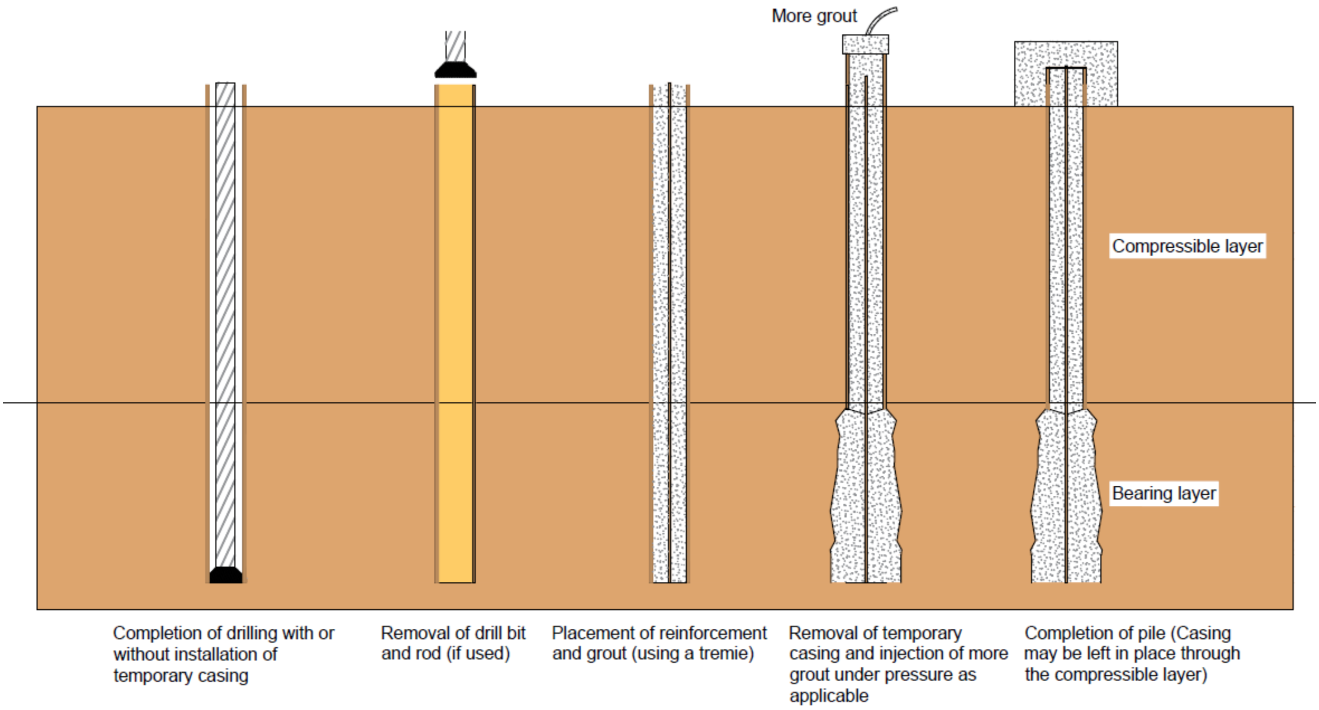

Figure 2.1: *Micropile construction sequence (modified from Sabatini et al., 2005).*

Micropiles can be installed as either floating piles or end-bearing piles. However, because of the small base area, end-bearing resistance is neglected in soil or weak rock. They rely mainly on shaft resistance unless a base enlargement can be constructed (Tomlinson & Woodward, 2015). Skillful installation can significantly enhance their bearing capacity, often achieving approximately 1.5 to 2.0 times that of a footing supported only by a raft. The high slenderness ratio of micropiles necessitates careful checks for buckling, especially when installed in soft soils as illustrated in Figure 2.2.

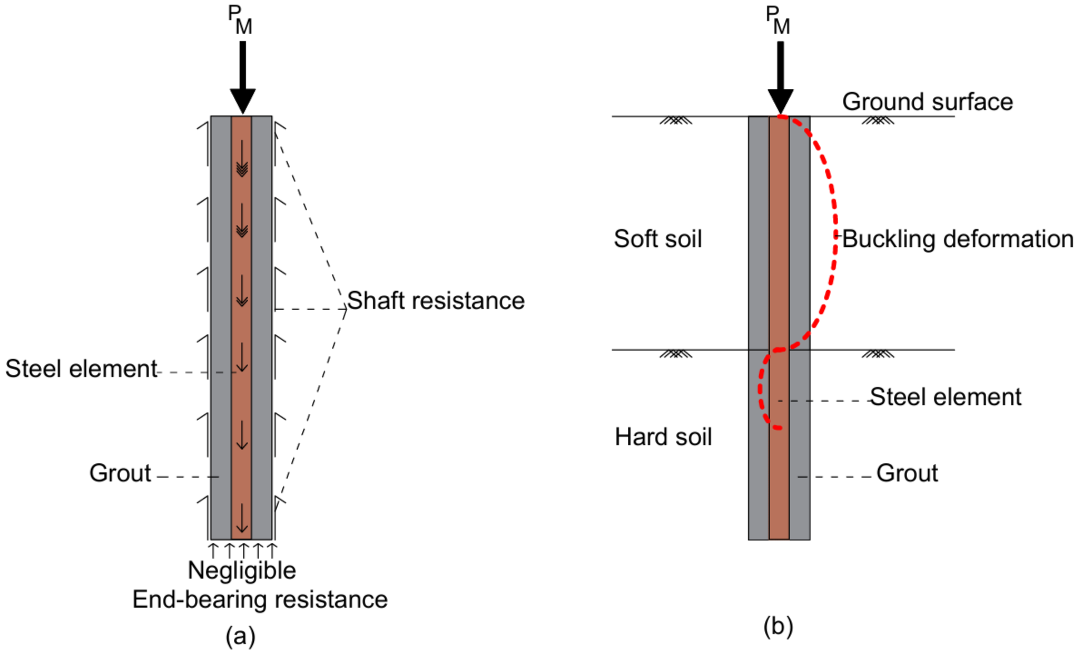

Figure 2.2: *Structural mechanisms in micropiles. (a) Load support. (b) Buckling.*

Micropiles serve as a cost-effective alternative to large diameter drilled shaft foundations, particularly in challenging ground conditions. Their ability to be installed quickly and with minimal disturbance makes them an attractive option for retrofitting and underpinning existing foundations, especially in urban areas where space is limited. They are also used for slope stabilization and earth retention, providing additional support to prevent landslides and enhance the stability of retaining walls and other earth retention systems. In new construction projects, micropiles offer a practical solution where traditional piles are impractical due to space constraints or ground conditions. Additionally, the installation of micropiles results in minimal disturbance to existing structures and reduced noise and vibration levels, making them an ideal solution for urban environments. The small size of micropiles and the use of advanced drilling techniques generate less spoil during installation compared to conventional drilled piles, making them an environmentally friendly option.

Micropiles can also be used as energy micropiles if they can exchange heat with the surrounding soil through embedded heat exchange loops, contributing to the heating and cooling of buildings. This dual functionality offers a sustainable solution for energy-efficient building systems.

2.2. Types and classifications of micropiles

Two criteria have been used by the U.S. Federal Highway Administration (FHWA) (Sabatini et al., 2005) to classify micropiles: the method of grouting or the construction type classification, and the philosophy of behavior or the design classification.

2.2.1. Construction type classification

Depending on the grouting technique used during construction, micropiles can either be type A, B, C, D or E (Figure 2.3). The method of grouting defines the grout/ground bond strength (or side resistance), which generally controls micropiles capacity. Micropiles may be installed either by gravity grouting, pressure grouting or post grouting (Bruce & Juran, 1997). The first method is used for type A micropiles. A tremie pipe is used to introduce grout in the drilled hole and grouting is done by gravity only, without applying excess pressure. Neat cement grout or sand-cement mortars can be used. Type A micropiles are suitable for installation in scenarios where the pile is embedded in rock or when low-capacity piles are being placed in stiff or hard cohesive soils, making the use of pressure grouting to achieve sufficient bond unnecessary. Type B micropiles are installed by pressure grouting through casing, wherein additional grout is injected during the removal of the casing or auger, often under excess pressure, after the primary grout has been placed (Bruce & Juran, 1997; Sabatini et al., 2005). Pressure between 0.5 and 1 MPa ensures thorough penetration into voids, fissures, and cracks within the surrounding soil or rock. This method reinstates lateral pressure which may have been reduced during the drilling process (Bruce & Juran, 1997). When pressure grouting through the casing is not possible, for example due to leakage around the casing or absence of the casing, the post grouting method can be used. Both types C and D micropiles are installed by post grouting where in the first phase, neat cement grout is placed in the hole as in type A. However, in type C micropiles similar grout is injected through a tube or reinforcing pipe from the head, without packers, at a pressure of at least 1 MPa, before hardening of the primary grout (typically within 15 to 25 minutes). This is also referred to as *injection globale unitaire*. Whereas type D micropiles involve injecting similar grout after several hours, through a sleeved pipe or sleeved reinforcement using packers, repeating the process as needed to achieve proper bond. Higher pressure values of 2 – 8 MPa are used. This is referred to as *injection répétitive et sélective*. Type E micropiles are self-drilled micropiles which require no casing. Drilling is done with grout injection (flushing) through a continuous-thread, hollow-core steel bar. When the desired depth is reached, the initial grout is then replaced by thicker grout (Caltrans, 2015). Typically, a pressure of 0.5 - 2 MPa is used during flushing and 2 - 6 MPa during grouting.

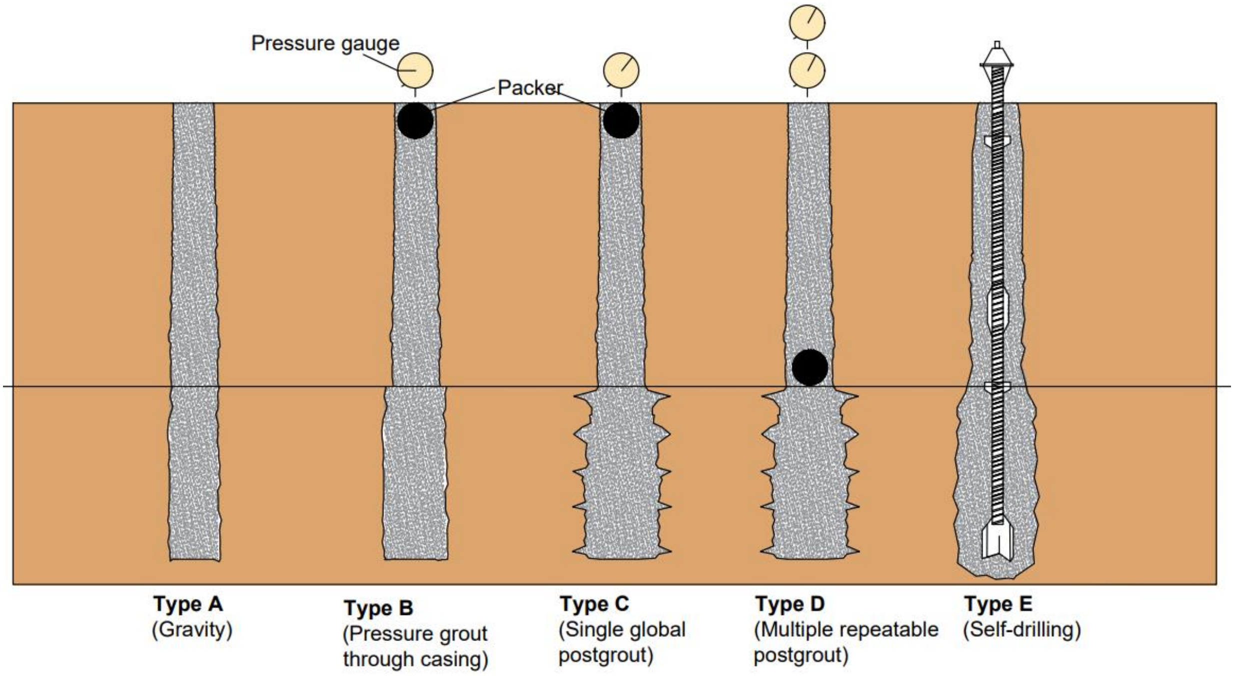

Figure 2.3: *Types of micropiles based on method of grouting (from Sabatini et al., 2005).*

2.2.2. Design classification

The classification of micropiles based on the design, or philosophy of behavior, differentiates between Case 1 and Case 2 micropiles (Sabatini et al., 2005), owing to their distinct behaviors in individual versus group applications. Case 1 micropiles are directly loaded, with most of the applied load resisted primarily by the steel reinforcement within the micropiles. Structurally, these micropiles transfer loads to deeper, more stable layers, both axially (in compression and tension) and laterally. Geotechnically, the load is supported through side resistance developed along a "bond zone" of the individual micropiles. This classification allows Case 1 micropiles to function similarly to traditional piles, acting independently or in groups to support structural loads. Their effectiveness in transferring structural loads to competent strata makes them suitable for structural support; foundations for new structures, underpinning of existing foundations, seismic retrofitting, and earth retaining structure foundations (Sabatini et al., 2005).

In contrast, Case 2 micropiles are designed to encompass and reinforce the soil internally, creating a composite structure capable of withstanding applied loads. Unlike Case 1, where the reinforcement within each micropile bears the load, Case 2 micropiles rely on the entire reinforced soil mass to resist loads. These micropiles typically form networks of interconnected piles, providing stability and support through a reticulated structure. Lightly reinforced compared to Case 1, Case 2 micropiles are mainly utilized for in situ reinforcement; ground strengthening, settlement reduction, slope stabilization and earth retention, and structural stability (Sabatini et al., 2005).

2.3. Design and Engineering Considerations for Micropiles

The design of micropiles, like other types of foundation, follows a series of logical steps. Firstly, the feasibility of using micropiles should be evaluated. Where deep foundations are required, both piles and micropiles should be considered. Usually, the installation of micropiles will be more costly compared to piles (drilled and driven), except in projects with specific technical constraints such as difficult access, limited space, vibration limits, subsurface voids (collapsible ground, karstic formation), underpinning of existing foundations, difficult and expensive installation of piles, such as ground containing significant amounts of boulders, cobbles, or other large debris (Sabatini et al., 2005). Then, a proper site investigation and assessment should be carried out to obtain all available information and geotechnical data. This can be done through visual site inspection, subsurface evaluation, laboratory testing, review of both published and unpublished information at and near the site. The different loads to which the micropile will be subjected should then be calculated. These loads, usually provided by the structural engineer, include the maximum compression and tension loads, transverse and overturning moments. Depending on the project, seismic loads, lateral loads and loads due to downdrag may also be of interest (Sabatini et al., 2005). The geotechnical engineer can then proceed with the preliminary design of the micropile. Individual micropiles should be spaced at a center-to-center distance of at least 760 mm or three diameters, whichever is greater. The length of the micropile will be dictated by the required friction resistance, the resistance to downdrag, uplift and any lateral loads. The cost-effective length limit is 30 m. Eurocode requires that the foundation should be verified for ultimate limit state (ULS) and serviceability limit state (SLS).

2.3.1. Ultimate limit state design (ULS)

The ultimate limit state is associated to the concept of failure or danger. The ultimate limit state can occur under the following conditions (Tomlinson & Woodward, 2015):

1. Loss of overall equilibrium of the structure and ground, considered as a rigid body. It typically applies to scenarios in which the strengths of the structural materials and the ground are not significantly mobilized within the failure mechanism (State EQU).
2. Internal failure or excessive deformation of a structure and its foundation (State STR).
3. Failure or excessive deformation of the ground in which the strengths of the soil or rock are significant in providing resistance (State GEO).
4. Loss of equilibrium of a structure due to uplift by water pressure or other vertical actions (State UPL).
5. Hydraulic heave, internal erosion and piping caused by hydraulic gradients (State HYD).

To avoid any failure, the sum of the applied actions (loads) must be less than or equal to the resistances.

$$\sum Q \leq R(X) \tag{2.1}$$

where Q denotes the actions, R the resistances and X the material properties.

In order to take into account the uncertainties associated with the determination of the parameters, partial (safety) factors are used to modify the three terms, to give the design values.

$$\sum \gamma_A Q \leq \frac{R\left(\frac{X}{\gamma_X}\right)}{\gamma_R};\ \gamma_A, \gamma_R\ and\ \gamma_r \geq 1 \tag{2.2}$$

Where γ_A are partial factors applied to the actions Q, γ_X are partial factors applied to the materials X and γ_R are partial factors applied to the resistances R. The numerator of the right term of the inequality gives the characteristic value of resistances, which when divided by the partial factors for the resistance (the denominator), the design value is obtained.

$$R_k = R\left(\frac{X}{\gamma_X}\right) \tag{2.3}$$

$$R_d = \frac{R_k}{\gamma_R} \tag{2.4}$$

The values of the factors given in Tables 2.1, 2.2, and 2.3 are chosen depending on the design approach being used. In Eurocode 7, three design approaches are proposed.

Design approach 1 (DA1) uses two combinations:

- Combination 1 (DA1-1): A1 + M1+ R1 factoring actions only
- Combination 2 (DA1-2): A2 + (M1 or M2) + R4 factoring materials only

Design approach 2 (DA2) uses sets A1 + M1 + R2, factoring actions and resistances (not materials). This approach is similar to the load and resistance factor design (LRFD) method of the US standards.

Design approach 3 (DA3) uses sets A2 + M2 + R3, factoring structural actions and materials (Geotechnical actions from the soil are unfactored).

Table 2.1: *Partial factors on actions for STR and GEO limit states.*

Action (Q)	Symbol	A1	A2
Permanent unfavorable action	γ_A	1.35	1.00
Variable unfavorable action		1.50	1.30
Permanent favorable action		1.00	1.00
Variable favorable action		0	0
Accidental action		1.00	1.00

Table 2.2: *Partial factors for soil parameters (material properties) for STR and GEO limit.*

Material property (X)	Symbol	M1	M2
Angle of shearing resistance, tan φ'	γ_A	1.00	1.25
Cohesion intercept, c'	γ_c	1.00	1.25
Undrained shear strength, c_u	γ_{cu}	1.00	1.40
Unit weight*, γ	γ_γ	1.00	1.00

M1 factors are used for structural actions while M2 are applied for unfavorable geotechnical actions caused by ground movements such as downdrag and transverse loading. M2 factors are not used to modify the adopted soil parameters for the design of axially loaded piles (Tomlinson & Woodward, 2015).

Table 2.3: *Partial resistance factors for bored piles and CFA piles for STR and GEO limit states (modified from Tomlinson & Woodward, 2015).*

Resistance (R)	Symbol	R1 and R3	R2	Set	
				R4 without explicit verification of SLS[A]	R4 with explicit verification of SLS[A]
Base	γ_b	1.00	1.40	2.00	1.70
Shaft (compression)	γ_s	1.00	1.40	1.60	1.40
Total combined (compression)	γ_t	1.00	1.40	2.00	1.70
Shaft in tension	$\gamma_{s,t}$	1.00	1.40	2.00	1.70

Note A - the lower γ values in R4 set may be adopted:

(a) If serviceability is verified by load tests (preliminary and/or working) carried out on more than 1% of the constructed piles to loads not less than 1.5 times the representative load for which they were designed

(b) If settlement is explicitly predicted by means no less reliable than in (a)

(c) If settlement at the SLS is of no concern

(It is suggested that current empirical design methods would satisfy the requirement in (b) where data exist for comparable ground and pile type).

In foundation engineering, the ultimate limit state results from a bearing capacity failure of the foundation, but also from excessive differential settlement leading to partial or full structural collapse.

2.3.1.1. Axial bearing capacity

Like piles, the axial bearing capacity of micropiles is the sum of the ultimate base resistance and shaft resistance.

$$Q_{lim} = Q_b + Q_s \tag{2.5}$$

Where Q_{lim} is the total bearing capacity, Q_b is the ultimate base resistance, Q_s is the ultimate base resistance.

Q_b and Q_s can be evaluated through several methods: methods based on fundamental soil properties (α and β method, Bustamante and Doix method), methods based on in-situ tests (standard penetrometer test and cone penetrometer test) and load tests.

- **α and β method (for types A and B micropiles)**

In the α and β method, the base resistance Q_b is often neglected as it is small as $\frac{L}{D} > 10$.

$$Q_s = \pi \cdot D \cdot \int_0^L q_s \cdot dz \qquad (2.6)$$

Where D is the perforation diameter, L is the micropile length, q_s is the unit shaft resistance.

$$q_s = a + \sigma_h \cdot \mu \qquad (2.7)$$

In undrained conditions (for cohesive soils) (Viggiani et al., 2012):

$\mu = 0$, and $q_s = a = \alpha \cdot c_u$

where α is the adhesion coefficient as given in Table 2.4.

Table 2.4*: Values of α (from Viggiani et al., 2012)*

Type of pile	c_u	α
Driven	$C_u \leq 25$	1.0
	$25 < C_u < 70$	$1 - 0.011(C_u - 25)$
	$C_u \geq 70$	0.5
Drilled	$C_u \leq 25$	0.7
	$25 < C_u < 70$	$0.7 - 0.008(C_u - 25)$
	$C_u \geq 70$	0.35

In drained conditions (cohesionless soils) (Viggiani et al., 2012):

$a = 0$ and $q_s = \sigma_h' \cdot \mu = \sigma'_h \cdot tan\delta$

It can also be written as $q_s = k \cdot tan\delta \cdot \sigma'_{vo} = \beta \cdot \sigma'_{v0}$

where σ_h' is the effective horizontal stress, σ'_{v0} is the effective vertical stress, $k = \frac{\sigma_h'}{\sigma_v'}$ is the earth pressure coefficient as given in Table 2.5, δ is the friction angle at the pile soil interface, and $\beta = ktan\delta$.

Table 2.5: *Values of* k *(from Viggiani et al., 2012)*

Type of pile	k - loose soil	k – dense soil	δ
Driven steel H section	0.7	1.0	20°
Driven closed end pipe	1.0	2.0	20°
Driven precast concrete	1.0	2.0	$3\varphi/4$
Driven cast in place concrete	1.0	3.0	φ
Drilled shaft	0.5	0.4	φ
CFA	0.6	0.6	φ
Where φ is the friction angle of the soil			

The α and β method is usually utilized for the design of types A and B micropiles.

- **Bustamante and Doix (1985) method (for types C and D micropiles)**

The Bustamente and Doix (1985) method is appropriate for the design of type C (IGU) and type D (IRS) micropiles (Viggiani et al., 2012). The soil characterization is made preferably by Ménard pressuremeter, but also by standard penetration test (SPT). It is further assumed that the shaft grouting pressure, p_g, falls within the following ranges with respect to the Menard pressuremeter limit pressure, p_L:

- $p_g > p_L$ for IRS micropiles
- $0.5p_L \leq p_g \leq p_L$ for IGU micropiles

and that the injection is carried out at a rate in the range 0.3 to 0.6 m^3/h in cohesive soils, and 0.8 to 1.2 m^3/h in cohesionless soils (Viggiani et al., 2012). Then the shaft resistance is calculated using the expression

$$Q_s = \pi \cdot D_s \cdot L_s \cdot s \tag{2.8}$$

$$D_s = \varphi D_d \tag{2.9}$$

$$Q_b = (0.15 \div 0.20) \cdot Q_s \tag{2.10}$$

where D_s is the effective diameter, D_d is the perforation diameter, L_s is the length of the injected portion of the micropile, and s is the shear resistance at the interface between the soil and the injected portion of the pile. s is given as a function of p_L or N_{SPT} by the following expressions (Viggiani et al., 2012):

$$s = a + b \cdot p_L \tag{2.11}$$

$$s = \alpha + \beta \cdot N_{SPT} \tag{2.12}$$

where N_{SPT} is the standard penetration (SPT) blow count.

The values of φ, a, b, α, and β are given in Tables 2.6 and 2.7.

Table 2.6: *Values of φ to obtain the effective diameter of the micropile (Viggiani et al., 2012).*

<table>
<tr><th rowspan="2">Type of soil</th><th colspan="2">Values of φ</th><th rowspan="2">Minimum suggested grout volume</th></tr>
<tr><th>IRS</th><th>IGU</th></tr>
<tr><td>Gravel</td><td>1.8</td><td>1.3 – 1.4</td><td>1.5 V_s</td></tr>
<tr><td>Sandy gravel</td><td>1.6 – 1.8</td><td>1.2 – 1.4</td><td>1.5 V_s</td></tr>
<tr><td>Gravelly sand</td><td>1.5 – 1.6</td><td>1.2 – 1.3</td><td>1.5 V_s</td></tr>
<tr><td>Coarse sand</td><td>1.4 – 1.5</td><td>1.1 – 1.2</td><td>1.5 V_s</td></tr>
<tr><td>Medium sand</td><td>1.4 – 1.5</td><td>1.1 – 1.2</td><td>1.5 V_s</td></tr>
<tr><td>Fine sand</td><td>1.4 – 1.5</td><td>1.1 – 1.2</td><td>1.5 V_s</td></tr>
<tr><td>Silty sand</td><td>1.4 – 1.5</td><td>1.1 – 1.2</td><td>IRS: (1.5 – 2) V_s ; IGU: 1.5 V_s</td></tr>
<tr><td>Silt</td><td>1.4- 1.6</td><td>1.1 – 1.2</td><td>IRS: 2 V_s ; IGU: 1.5 V_s</td></tr>
<tr><td>Clay</td><td>1.8 – 2.0</td><td>1.2</td><td>IRS: (2.5 – 3) V_s ; IGU: (1.5 – 2) V_s</td></tr>
<tr><td>Marl</td><td>1.8</td><td>1.1 – 1.2</td><td>(1.5 – 2) V_s for stiff layers</td></tr>
<tr><td>Marly limestone</td><td rowspan="2">1.8</td><td rowspan="2">1.1 – 1.2</td><td rowspan="2">(2 – 6) V_s or more for fractured layers</td></tr>
<tr><td>Weathered or fractured limestone</td></tr>
<tr><td>Weathered and/or fractured rock</td><td>1.2</td><td>1.1</td><td>(1.1 – 1.5) V_s for slightly fractured layers
2 V_s or more for fractured layers</td></tr>
<tr><td colspan="4">$V_s = \frac{\pi D_s^2}{4}$
V_s is the perforation volume</td></tr>
</table>

Table 2.7: *Values of the coefficients a, b, α, and β (Viggiani et al., 2012).*

Soil type	Micropile type	a (MPa)	b	α (MPa)	β (MPa)
Sand and gravel	IGU	0	0.10	0	0.005
	IRS	0.05	0.10	0.05	0.005
Silt and clay	IGU	0.04	0.06	0.04	0.004
	IRS	0.10	0.084	0.1	0.006
Weathered and fractured	IGU	0.04	0.10		

- **CPT-based method**

The bearing capacity of micropiles can also be evaluated from cone penetration test (CPT) data. It is assumed that (Viggiani et al., 2012):

$$q_b = c_p \cdot q_{cL} \text{ and } q_{s,i} = c_{s,i} \cdot q_{c,i} \tag{2.13}$$

where c_p and $c_{s,i}$ are empirical coefficients that depend on soil type and pile type; q_{cL} is the value of the cone resistance representative of the pile base level; $q_{c,i}$ is the cone resistance representative of the layer i. The value of q_{cL} is obtained by averaging q_c in a suitable interval of depth around the pile base: for instance, between (L–1.5d) and (L+1.5d), provided there are no strong stratigraphic changes within a range of five to eight pile diameters above the pile base. The value of $q_{c,i}$ is the average of q_c over the layer i. The values of c_p and $c_{s,i}$ are given in Tables 2.8, 2.9, 2.10 and 2.11. For driven piles in sand, c_p may be assumed equal to 1.

Table 2.8: *Pile base resistance q_b vs CPT cone resistance q_c for piles in sand (Viggiani et al., 2012)*

Pile type	c_p	Notes	Source
Displacement	$0.3 \div 0.5$	Database of high-quality pile load tests	Chow (1997)
	$0.20 \div 0.35$	Computed	Lee and Salgado (1999)
	$0.32 \div 0.47$	Test data	
	0.4	Reinterpretation of the Chow (1997) data	Randolph (2003)
	0.4 for Franki piles 0.57 for precast concrete piles	Data from pile load tests; Q_{lim} by Van der Veen's criterion	Aoki and Velloso (1975)
	0.2	Load tests on drilled shafts	Franke (1989)
Replacement	$0.13 \div 0.02$	Calibration chamber load tests	Ghionna et al. (1994)
	0.23 exp $(-0.0066D_R)$	FEM analyses and calibration chamber tests	Salgado (2006)
	$0.20 \div 0.26$	Test data	Lee and Salgado (1999)

Table 2.9: *Pile base resistance q_b vs CPT cone resistance q_c for piles in clay (Viggiani et al., 2012)*

Pile type	c_p	Notes	Source
Displacement	0.9 ÷ 0.10	Soft to lightly OC clays	State of the art
	0.35 for driven piles 0.30 for jacked piles	Stiff clays	Price and Wardle (1982)
Replacement	0.47 for pure clay 0.52 for silty clay 0.78 for silty clay with sand 0.71 for sandy clay with silt 0.83 for sandy clay	Medium to stiff clays	Aoki and Velloso (1975)
	0.34 for pure clay and silty clay 0.41 for silty clay with sand and sandy clay with silt 0.66 for sandy clay	Medium to stiff clays	Lopes and Laprovitera (1988)

Table 2.10*: Pile shaft resistance q_s vs CPT cone resistance q_c for piles in sand (Viggiani et al., 2012)*

c_s	Source
0.008 for open ended steel pipe piles 0.012 for precast concrete and closed-ended steel pipe piles	Schmertmann (1978)
$0.004 \div 0.006$ per $D_R \leq 50\%$ $0.004 \div 0.007$ per $50\% < D_R \leq 70\%$ $0.004 \div 0.009$ per $70\% < D_R \leq 90\%$ Closed-ended pipe piles	Lee et al. (2003)
0.0040 for clean sand 0.0057 for silty sand 0.0069 for silty sand with clay 0.0080 for clayey sand with silt 0.0086 for clayey sand Driven piles: for Franki piles: multiply number above by 0.7 For drilled shafts: multiply number above by 0.5	Aoki and Velloso (1975) Aoki et al. (1978)
0.0027 for clean sand 0.0037 for silty sand 0.0046 for silty sand with clay 0.0054 for clayey sand with silt 0.0058 for clayey sand Replacement piles	Lopes and Laprovitera (1988)
$0.0034 \div 0.006$ This method uses a corrected value of cone resistance $q_c - u$, where u is the pore pressure at depth considered	Eslami and Fellenius (1997)

Table 2.11: *Pile shaft resistance q_s vs CPT cone resistance q_c for piles in clay (Viggiani et al., 2012)*

c_s	Source
$0.074 \div 0.086$ for sensitive clay $0.046 \div 0.056$ for soft clay $0.021 \div 0.028$ for silty clay or stiff clay Driven piles This method uses a corrected value of cone resistance $q_c - u$, where u is the pore pressure at depth considered	Eslami and Fellenius (1997)
0.025 Displacement piles	Thorburn and MacVicar (1971)
0.017 for pure clay 0.011 for silty clay 0.0086 for silty clay with sand 0.0080 for sandy clay with silt 0.0069 for sandy clay Driven piles: for Franki piles: multiply number above by 0.7 For drilled shafts: multiply number above by 0.5	Aoki and Velloso (1975) Aoki et al. (1978)
0.012 for pure clay 0.011 for silty clay 0.010 for silty clay with sand 0.0087 for sandy clay with silt 0.0077 for sandy clay Non displacement piles	Lopes and Laprovitera (1988)

2.3.1.2. Design of type E micropiles (self-drilling micropiles)

Unlike Type A, B, C, and D micropiles, the design of Type E micropiles has not been widely documented. The German standard, EA – Pfähle (German Geotechnical Society, 2013) provides empirical values for skin friction in tubular grouted micropiles for both non-cohesive (Table 2.12) and cohesive soils (Table 2.13). However, the standard notes that the database of load tests for this type of micropile is limited. Therefore, depending on site-specific conditions, higher load capacities may be expected. Additionally, base resistance is typically considered negligible in design due to the high L/D ratio.

Table 2.12: E*mpirical data ranges of skin friction $q_{s,k}$ for tubular grouted micropiles in non-cohesive soil (German Geotechnical Society, 2013)*

Mean CPT cone resistance q_c [MN/m²]	Ultimate limit state value $q_{s,k}$ of pile skin friction [kN/m²]
7.5	170 - 210
15	255 - 320
≥ 25	305 - 365
Intermediate values may be interpolated.	

Table 2.13: E*mpirical data ranges of skin friction $q_{s,k}$ for tubular grouted micropiles in cohesive soil (German Geotechnical Society, 2013)*

Shear strength C_u of the undrained soil [kN/m²]	Ultimate limit state value $q_{s,k}$ of pile skin friction [kN/m²]
60	70 - 80
150	115 - 125
≥ 250	140 - 150
Intermediate values may be interpolated.	

2.3.1.3. Structural failure

Structural failure in micropiles can be due to the grout-reinforcement failure, failure of the reinforcement, buckling or failure of the connection to the structure. It occurs at a load higher than the GEO failure load, that is:

$$Q_{d,GEO} \leq Q_{d,STR} \tag{2.14}$$

where $Q_{d,GEO}$ is the design geotechnical bond capacity and $Q_{d,STR}$ the design structural capacity. $Q_{d,STR}$ is calculated as follows.

- For grout-reinforcement failure (compression-tension), $Q_d = {A_b q_{a,bond}}/{\gamma_m}$
- For reinforcement failure (compression-tension-bending), $Q_d = {A_s q_{a,y}}/{\gamma_m}$

where A_b is the grout-steel interface area, A_s is the cross-sectional steel area, $q_{a,bond}$ is the grout-to-steel bonding strength, $q_{a,y}$ is the steel yield stress, and $\gamma_m = 1.05$ is the safety factor.

Buckling verification is done only for end-bearing micropiles installed through soft soils or voids.

$$Q_d \leq 0.04\, N_{cr,E} \tag{2.15}$$

$$N_{cr,E} = \frac{\pi^2 E \cdot I_{x,y}}{L^2_{0,x,y}} \tag{2.16}$$

where E is the steel elastic modulus, $I_{x,y}$ is the second moment of area about the x or y axis, $L^2_{0,x,y} = K \cdot L =$ effective length for buckling about the corresponding axis. K is the effective length factor as given in Figure 2.4.

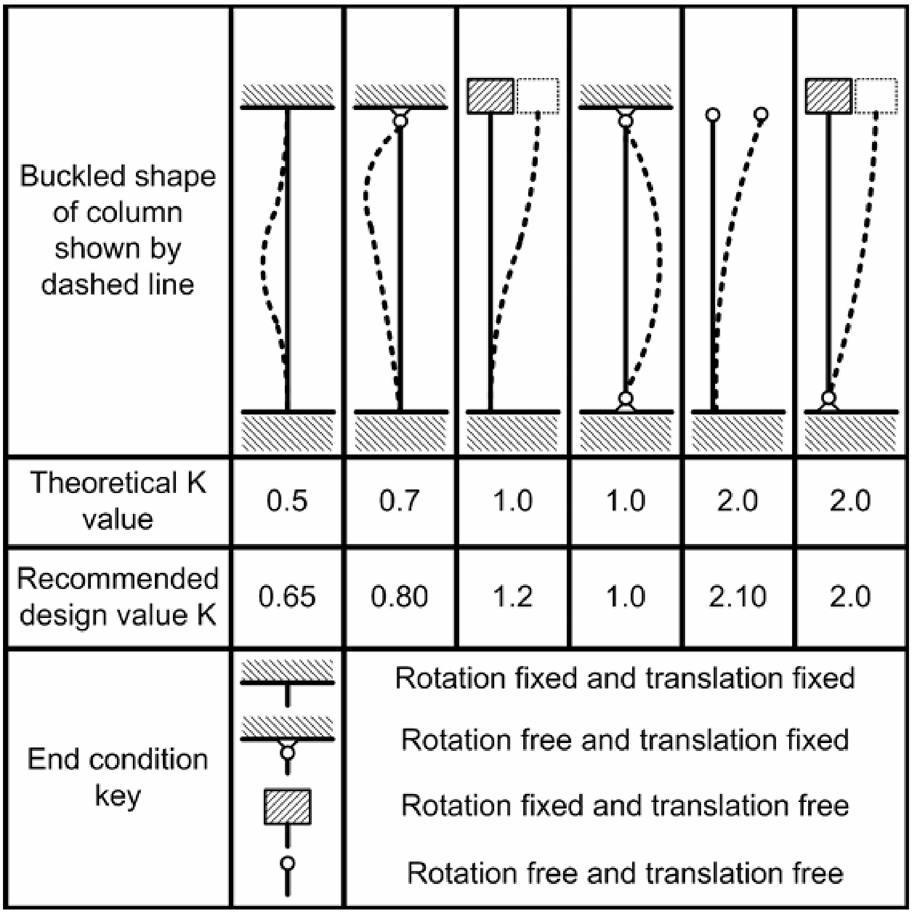

Figure 2.4: *Values of the effective length factor K.*

2.3.1.4. Group design of piles

When piles are installed in groups, their interaction with the surrounding soil and with each other can affect their performance. The load-carrying capacity of a group is not simply the sum of the capacities of individual piles but is reduced by the group efficiency factor (η) (Coduto, 2001). This factor depends on various parameters, including the number, length, diameter, spacing, and arrangement of piles, the method of load transfer (side friction versus end bearing), the installation technique, the type and condition of the soil, the time elapsed since installation, and the interaction between the pile cap and the soil (Coduto, 2001). The allowable group capacity, P_{ag}, can then be computed using the equation (Coduto, 2001):

$$P_{ag} = \eta N P_a \quad (2.17)$$

where P_{ag} is the allowable pile group capacity, N is the number of piles, and P_a is the allowable capacity of a single pile.

A widely used empirical method to estimate the group efficiency factor is the Converse-Labarre equation, which accounts for pile geometry and arrangement. It is given by:

$$\eta = 1 - \theta \cdot \frac{(\eta-1)m+(m-1)n}{90mn} \quad (2.18)$$

where η is the number of piles per row, m is the number of rows, and $\theta = tan^{-1}(B/s)$, with B being the diameter of the pile and s the center-to-center spacing between the piles.

2.3.2. Serviceability limit state design

Serviceability limit states (SLSs) are concerned with ensuring that the deformations of a structure due to ground movements below the foundations do not reduce the useful life of the structure, do not cause discomfort to people or cause damage to finishes, non-structural elements, machinery or other installations in the structure (Tomlinson & Woodward, 2015). The design against serviceability limit states requires that the overall and differential displacement of a foundation be kept below the corresponding admissible values (Viggiani et al., 2012). To satisfy this state, the effects of the applied actions, E_A (action effect) must be less than or equal to a limiting value of the action effect, C_A (limiting settlement).

$$E_A \leq C_A \quad (2.19)$$

There is no single universal allowable head displacement for micropiles. This limit is usually defined by the design engineer. According to Poulos et al., 2001, acceptable settlement values could be 50 – 75 mm for buildings on sand and 75 – 135 mm for those on clay. Eurocode 7, specifically Clause 7.6.4.1, indicates that when piles bear on medium-dense to dense soils, ULS design safety requirements generally suffice to prevent SLS issues in the supported structure. This implies that the combination of EC7 ULS partial factors results in an effective global safety factor between 2 and 3 for single piles. This range, dependent on the design approach used and the applied variable action, is adequate for limiting settlement to within 10 mm (Tomlinson & Woodward, 2015). To achieve economic efficiency in pile design, the settlement at the applied load should closely approach the acceptable limit set by the structural designer, typically involving the full mobilization of shaft resistance (Tomlinson & Woodward, 2015). Settlement of pile foundations may be neglected especially for small piles (diameter less than 600 mm) (Tomlinson & Woodward, 2015; Viggiani et al., 2012).

Various methods can be used for the calculation of settlement values; load-settlement curves from load tests, load transfer curves, boundary element methods, finite element methods, and analytical methods empirical methods. The settlement w_s of a single pile subjected to an axial load may be calculated as (Viggiani et al., 2012):

$$w_s = \frac{d}{M}\frac{Q}{Q_{lim}} = \frac{d}{M}\frac{1}{FS} \tag{2.20}$$

where d is the pile diameter, M is a factor related to the surrounding soil, Q is the applied load, Q_{lim} the bearing capacity and $FS = \frac{Q_{lim}}{Q}$ the factor of safety. Values of M given in Table 2.14 applies for $FS \geq 2.5$.

Table 2.14: *Suggested values of M (Viggiani et al., 2012)*

Pile type	Soil type	M
Displacement	Cohesionless	80
	Cohesive	120
Small displacement (driven H or tube; large stem auger piles)	Cohesionless	50
	Cohesive	75
Replacement	Cohesionless	25
	Cohesive	40

For piles in a group, the settlement of individual piles and the average settlement of the group w_g is always larger than the settlement of a single pile w_s subjected to an axial load equal to the average load per pile of the group. (Viggiani et al., 2012) attributes this to the effect of the interaction among the piles in a group via the surrounding soil.

$$w_g = R_s w_s = nR_G w_s \tag{2.21}$$

where w_s is the settlement of a single pile under the average working load Q /n of the group (Q = total load applied to the foundation, n = the number of piles in the group), R_s is an amplification factor called 'group settlement ratio', quantifying the effect of interaction between piles, $R_G = \frac{R_s}{n}$ is the group reduction factor, $1 \leq R_s \leq n$, $\frac{1}{n} \leq R_G \leq 1$. R_s may be estimated by the expression (Viggiani et al., 2012):

$$R_s = \frac{w_g}{w_s} = 0.29 \cdot n \cdot R^{-1.35} \tag{2.22}$$

where $R = \sqrt{\frac{ns}{L}}$ is the group aspect ratio, s the center-to center spacing between piles and L the length of each pile.

2.4. Overview of geothermal energy and energy geostructures

At few meters beneath the surface, typically around 8-10 meters, the ground temperature fluctuates and is influenced by daily and seasonal weather patterns (Barla, 2022; Florides & Kalogirou, 2005; Sani et al., 2019) . However, beyond this depth, the temperature remains relatively stable and exhibits an average increase of 2.5-3°C for every 100 meters. This temperature gradient ensures that the ground is warmer than the external air in winter and cooler in summer (Barla, 2022; Busby, 2015; Sani et al., 2019) (Figure 2.5). Historically, this heat referred to as geothermal heat has been harnessed for bathing in hot springs and for spiritual practices for over 10,000 years. Today, it is utilized for a variety of modern applications including electricity production and agricultural heating.

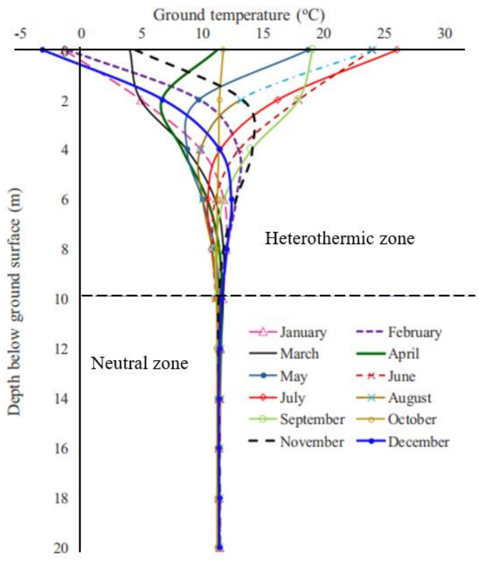

Figure 2.5: *Variations in ground temperature with depth for London clay (after Sani et al., 2019).*

Geothermal energy refers to the thermal energy harnessed from beneath the Earth's surface. Low enthalpy geothermal energy refers to heat stored in the ground at temperatures typically under 90 °C and found at relatively shallow depths, usually less than 400 meters (Sethi and Casasso, 2020). Geothermal systems are environmentally friendly, emitting little to no greenhouse gases, and are cost-effective as they require minimal to no fuel. The choice between open loop and closed loop geothermal systems is made depending on the presence of aquifer water. While the former exchange heat to/from aquifer water through pipes inserted in boreholes making them less costly, there is no pumping of water in the latter. The pipes in closed loop geothermal systems are inserted in the heat exchanger. Although not efficient and cost-effective as open loop systems, closed loop systems have many advantages amongst which; no clogging and contamination, little maintenance, longer life span, long term economic benefits and lower long-term risks permitting their installation under many types of ground conditions. Vertically installed systems are less affected by shallow ground temperatures, they require little space, have a higher heat efficiency with lower pumping costs however they are more expensive than horizontally installed systems (De Moel et al., 2010) which are only about 1.5 - 3 m in the ground (Figure 2.6).

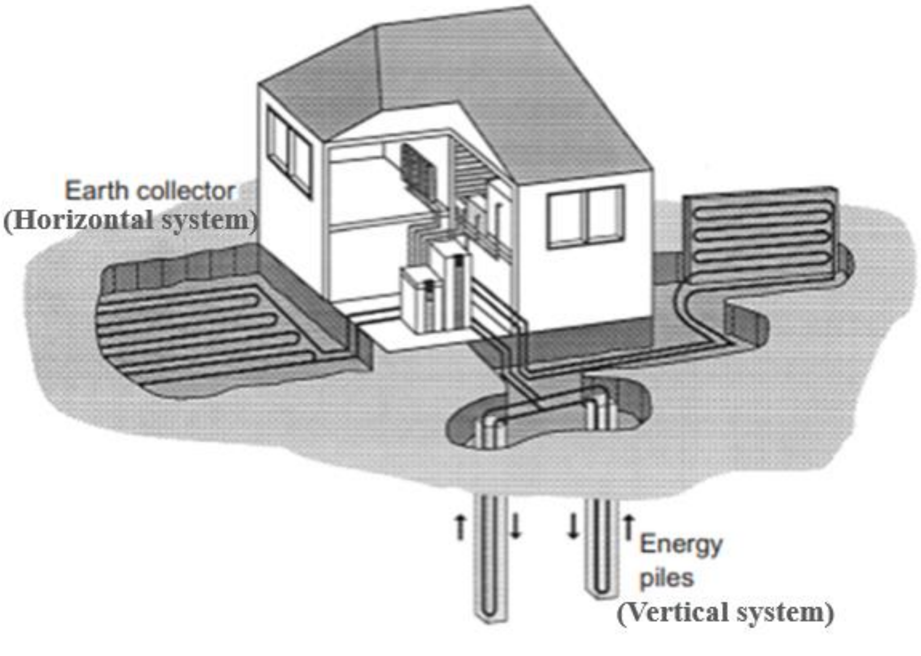

Figure 2.6: *Schematic representation of the heating/cooling of a small house with both horizontal and vertical geothermal systems (Brandl, 2006).*

Geothermal energy is a renewable, season independent, and base-load source of energy. However, the high initial costs associated with geothermal installations pose a significant barrier to its widespread adoption. Currently, financial incentives from public authorities are the most common form of support to promote and expand the use of geothermal energy for renewable heating (REN21, 2022). Nevertheless, energy geostructures are a cost-effective method of extracting geothermal energy for heating and cooling of structures.

2.4.1. Definition and types of energy geostructures

Until the 1980s, geothermal energy extraction was primarily achieved through wells. However, the introduction of energy geostructures marked a significant advancement in harnessing renewable energy from the ground. Energy geostructures, also referred to as thermo-active ground structures, are structures initially designed for structural or geotechnical roles, to which an energy role has been added. These innovative systems encompass a variety of built elements such as foundations (including piles and slabs), retaining walls (such as diaphragm walls and sheet walls), and underground structures like tunnels and basements.

The extraction of geothermal energy through energy geostructures is done by inserting plastic pipes in the structural element (concrete, steel or grout). These pipes serve as conduits for a heat exchange fluid, such as water, water mixed with glycol, or saline solutions. By circulating this fluid through the pipes, heat exchange between the ground and the structure is facilitated. This process allows buildings to be heated in winter and cooled in summer by utilizing the stable thermal properties of the earth beneath them. Energy geostructures systems comprise a primary unit, a secondary unit and a heat pump. The primary unit is the part of the system embedded in the ground consisting of a heat exchange fluid circulating in plastic pipes inserted in the micropiles. The pipes are inserted in the micropiles just before grouting. This primary unit is connected to the secondary unit via the heat pump. The primary unit is linked to the secondary unit via the heat pump. The secondary unit comprises the underfloor pipe network responsible for transferring heat energy into or out of the building. A schematic representation of a geothermal energy micropiles system is shown in Figure 2.7.

Energy geostructures are designed to optimize energy efficiency while minimizing environmental impact. They are easily combined with other renewable energy systems like solar systems and district systems. They have the potential to achieve savings of up to two-thirds in conventional heating costs as additional drilling costs are not included (Brandl, 2006).

2.4.1.1. Energy foundations

Energy foundations are the first type of energy geostructures that were used. They were introduced in the 1980s with the energy slabs and energy piles in Austria and Switzerland (Brandl, 2006). Since then, successful implementation of these foundations has been recorded

(Bourne-Webb et al., 2009; Laloui et al., 2006; Nagano, 2007; Prodan et al., 2020; Sani et al., 2019). Energy foundations are a type of energy geostructure that integrates the structural support functions of conventional foundations with the ability to harness geothermal energy for heating and cooling purposes. Energy foundations typically consist of deep foundations such as piles, drilled shafts, or caissons, into which heat exchanger pipes are embedded. Energy piles are the most common energy foundation used (Loveridge et al., 2020). They have a specific heat flux typical between 20 W/m and 80 W/m (Loveridge et al., 2020; Ronchi et al., 2018). Base slabs have a lower heat flux between 10 - 30 W/m^2 of earth-contact area (Brandl, 2006). A lot of research has been done as far as energy piles are concerned. Both analytical and numerical models have been developed to capture the thermo-mechanical behaviour of energy piles. Generally, the thermal performance of an energy pile system is affected by many factors; ground and concrete thermal conductivity, pipe length, diameter and configuration, pile length, type of thermal loading (cyclic or continuous), flow rate inside pipes, etc… It is also required that the additional stresses and strains developed because of the added thermal load, should not exceed the design limits. Energy foundations are highly durable and reliable, with low maintenance requirements.

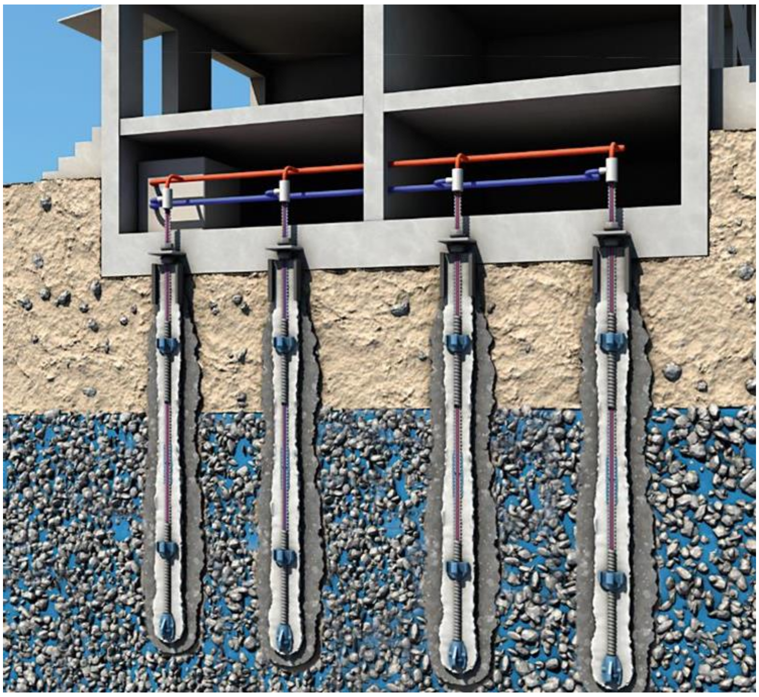

Figure 2.7*: TITAN geothermal energy micropile system (Friedr. Ischebeck GmbH, 2014).*

2.4.1.2. Energy walls

The first use of energy walls was in 1996 with the introduction of diaphragm walls (Brandl, 2006). Energy walls are employed in diverse settings ranging from residential and commercial buildings to infrastructure projects like underground tunnels and bridge abutments.

Diaphragm walls are underground structural elements commonly used as retention systems and permanent foundation walls. Their width and depth usually range between 0.8m to 1.2m and 10m to 40m respectively. Thermally activating diaphragm walls implies inserting pipes either on one side or both sides of the wall. Important factors to consider in the design of energy walls are the undisturbed ground temperature, the groundwater flow velocity, and the ground thermal conductivity (Di Donna et al., 2017). The long term exchanged power per square meter of diaphragm wall surface is about 15 – 20 W/m^2 (Bourne-Webb et al., 2016; Di Donna et al., 2017).

The exploitation of renewable energy of the shallow subsurface and especially of open waters can also be achieved through the thermal activation of sheet pile walls. In fact, energy sheet pile walls can provide a high heat exchange rate of 285 W/m and up to 430 W/m without and with open water streams respectively, at volumetric flow rates between 1.0 m^3/h and 2.5m^3/h (Martin. Ziegler et al., 2019).

2.4.1.3. Energy tunnels

Recently, attention has been paid to using tunnels for heating and cooling purposes. Energy tunnels are constructed underground, typically beneath buildings or transportation routes, and incorporate a network of piping systems for heat exchange. This allows the tunnel to act as a large-scale heat exchanger, transferring geothermal energy to buildings or other infrastructure above. Compared to piles and walls, tunnels involve a larger volume of ground and surface for heat exchange. Tunnels are particularly well-suited as heat exchangers in urban areas, where the exchanged heat can directly be utilized by adjacent buildings (Figure 2.8) and integrated into district heating and cooling systems (Barla & Di Donna, 2018). However, city scale planning, interference evaluation and regulation are required for enhanced geothermal exploitation by the means of tunnels (Barla & Di Donna, 2018). The specific heat exchange power obtained from energy tunnels can be 10 – 20 W/m2 in the absence of groundwater flow and 50 - 60 W/m2 in the case of relevant groundwater flow (Barla & Insana, 2023).

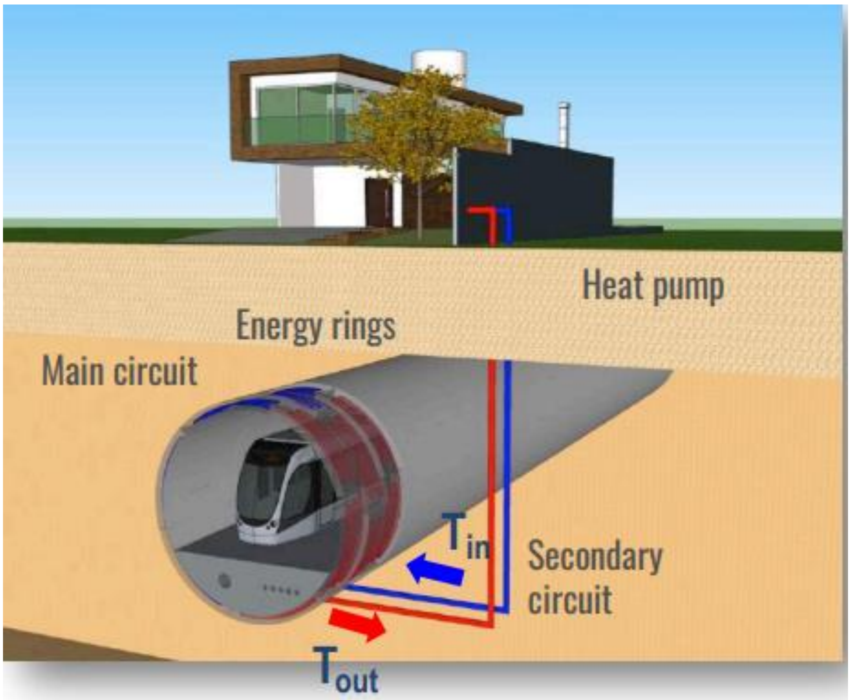

Figure 2.8: *Schematic representation of an energy tunnel providing heating/cooling to a house (Barla, 2023).*

2.4.2. Additional design and engineering considerations for energy piles and micropiles

Energy piles and micropiles serve dual purposes, providing structural support while facilitating heat exchange between the ground and the built environment. This dual functionality introduces additional design and engineering considerations beyond those required for conventional piles described in section 2.3. The integration of thermal and structural design elements necessitates a thorough understanding of both geotechnical and thermal properties of the site, as well as advanced modeling techniques to predict and optimize performance. The following sections outline key considerations, including site investigation, thermal response testing, structural and thermal design integration, and numerical modeling.

2.4.2.1. Site investigation and thermal Response Testing

For the effective design and implementation of energy piles and micropiles, a thorough site investigation is crucial. This process involves evaluating the thermal and geotechnical properties of the soil and rock at the site. Key thermal parameters include the undisturbed soil temperature, soil specific heat capacity, thermal diffusivity, soil thermal conductivity, the borehole thermal resistance, and the ground water flow direction and velocity which influence the efficiency of heat transfer between the energy piles and the ground (Brandl, 2006; Cecinato & Loveridge, 2015).

The undisturbed soil temperature is commonly measured by placing temperature sensors in the borehole or by circulating the heat exchange fluid without heating for 10 to 30 minutes before any test is performed. The mean fluid temperature corresponds to the undisturbed ground temperature (Zhang et al., 2014). The soil specific heat capacity can be measured in the laboratory by mixing water and soil of different temperatures. Test temperatures of 0°C for soil and 20°C for water are commonly used, and the steady-state temperature of the mixture is measured (Brandl, 2006). If the total thermal energy remains constant and the specific heat capacity of water is known, the specific heat capacity of soil can be calculated using the formula:

$$c_s(T_s)T_s m_s + c_w(T_w)T_w m_s = [c_s(T_{min})m_s + c_w(T_{min})m_w]T_{min} \tag{2.23}$$

where T_s is the temperature of the cooled soil (°C); T_w is the temperature of the water before mixing (°C); T_{min} is the minimum temperature of the mixture (°C); m_s, m_w are the mass of the soil and the water (g); and c_s, c_w are the specific heat capacities of the soil and the water (J/g/K).

The soil thermal conductivity, k (W/mK) can be obtained from laboratory or in situ tests. In the laboratory, steady state methods or transient methods can be used. Steady state methods for example the thermal cell method (Clarke et al., 2008), involves applying a thermal gradient to a soil sample and using Fourier's law to determine the thermal conductivity. The Power and temperature difference are known. Fourier's law is mathematically expressed as:

$$Q = \frac{k \cdot A \cdot \Delta T}{\Delta X} \tag{2.24}$$

where Q is the applied power (W), A is the area of the soil sample, ΔT is the temperature difference and ΔX is the thickness of the soil sample.

Commonly used transient methods for the determination of the ground thermal conductivity are the needle probe method and the thermal response test (TRT) in the laboratory and in-situ (Sanner et al., 2005) respectively. TRT involves circulating a heat carrier fluid through the installed pipes within a test pile or borehole and measuring the temperature response of the ground over time. A known and constant heat power Q is injected into the borehole heat exchanger. The heat power is typically supplied using an electric heater connected to a circulating pump that ensures a constant flow rate of the heat carrier fluid. The inlet and outlet temperatures of the heat carrier fluid are continuously monitored over time. Several authors (Gehlin, 2002; Sanner et al., 2005) recommend a minimum test duration of 50 hours for boreholes. However, for small diameter piles (less than 300 mm) constructed with cementitious materials like micropiles, a test duration of 70 - 100 hours is expected to be reliable (Loveridge et al., 2014). A schematic representation of the thermal response test setup is shown in Figure 2.9.

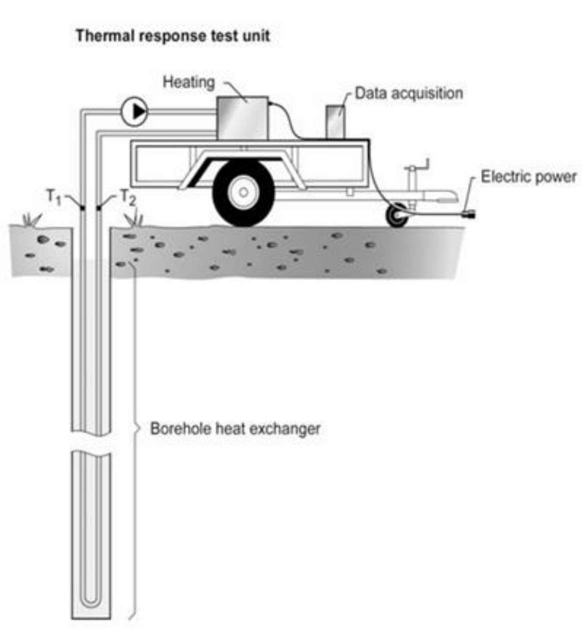

Figure 2.9: *Thermal response test setup (from Gehlin, 2002).*

TRT data is interpreted using the line source model. Ingersoll and Plass (Ingersoll & Plass, 1948) improved the line source model to the design of ground heat exchangers. This model assumes that the heat source in the borehole can be approximated to an infinite line source embedded in a homogenous medium (Loveridge et al., 2020; Sanner et al., 2005). The average temperature of the inlet and outlet fluid $T_{mean} = \frac{T_{in}+T_{out}}{2}$ is plotted against the natural logarithm of time (in seconds), $\ln t$. The thermal conductivity is then calculated as (Gehlin, 2002; Loveridge et al., 2014; Ronchi et al., 2018; Sanner et al., 2005):

$$k = \frac{Q}{4\pi L g} \tag{2.25}$$

where k is the ground thermal conductivity (W/mK), Q is the injected power (W), L is the length of the pile (m), and g is the gradient of the curve. Q can be measured directly or using the equation:

$$Q = mC\Delta T \tag{2.26}$$

where m is the mass flow rate (kg/s), C the specific heat capacity of the fluid (J/kgK), and ΔT is the difference between the inlet and outlet temperature (K).

The thermal resistance of the borehole, R_b or the pile can then be calculated from (Gehlin, 2002):

$$T_{f(t)} = \frac{q}{4\pi k} \cdot \left(\ln \left(\frac{4\alpha t}{r_b^2} \right) - \gamma \right) + q \cdot R_b + T_g \tag{2.27}$$

where $T_{f(t)} = T_{mean}$ is the average fluid temperature, α is the thermal diffusivity of the ground, r_b is the borehole radius, $\gamma = 0.5772$ is the Euler constant, $q = \frac{Q}{L}$ (W/m) is the specific heat rate, and T_g is the undisturbed ground temperature.

Knowledge about the groundwater flow direction and velocity is also important for a proper design of energy piles. The presence of groundwater can enhance convective heat transfer, increasing the efficiency of heat exchange between the piles and the ground. A high groundwater flow rate is desirable when the system is used for either heating or cooling only as ground water provides a better regeneration of the soil (Brandl, 2006; Katzenbach et al., 2008). However, if used for seasonal operations, a low permeability soil, a low groundwater flow rate, and a low hydraulic gradient are more favorable (Brandl, 2006). Ground water level at different points can be obtained with piezometric measurements. From this data, the direction and gradient of the ground water flow can be determined using Darcy's law:

$$Q = K_H A \frac{\Delta H}{\Delta l} \tag{2.28}$$

$$q_H = \frac{Q}{A} \tag{2.29}$$

$$v_H = \frac{q_H}{n_e} \tag{2.30}$$

where Q is the total discharge (m^3/s), K_H is the hydraulic conductivity (m/s), A is the cross-sectional area (m^2), ΔH is the difference in hydraulic head (m), Δl is the distance between the piezometers, q_H is the specific discharge or Darcy flux (m/s), v_H is the flow velocity, and n_e is the effective porosity (dimensionless).

2.4.2.2. Integration of structural, geotechnical and thermal design

The integration of structural and thermal design is a fundamental aspect of energy geostructures. Unlike conventional piles, energy piles must accommodate both mechanical loads and thermal loads induced by the heat exchange process. The dual functionality requires a holistic design approach to ensure structural integrity while optimizing thermal performance. It is essential to note that energy piles are primarily designed to fulfill structural and geotechnical roles, and their structural aspects, such as length, diameter, and number, should not be altered to suit thermal requirements.

The thermal design of energy micropiles involves optimizing the heat exchanger configuration to enhance heat transfer efficiency while minimizing any adverse impact on structural performance. This process includes selecting suitable pipe materials, determining the optimal pipe diameters and lengths, and setting the appropriate flow velocity and conditions (laminar or turbulent flow). Additionally, the layout must be configured to ensure uniform heat distribution and effective operation under varying seasonal and operational. The outcome of the thermal design is the determination of the system's thermal potential, typically expressed in terms of the heat transfer rate. Brandl (2006) suggests pre-design heat transfer values of about 40-60 W/m for energy piles with diameters of 0.3-0.5 m. However, specific guidelines for smaller piles or micropiles are not provided. The heat transfer rate of the pile can be evaluated using equation 2.26.

For more complex projects, especially those with intricate ground properties and pile groups, numerical modeling is recommended. Brandl (2006) recommends numerical modeling for projects with heating and cooling demands exceeding 50 kW, or where continuous cooling of more than 20 kW is required. Other factors must be considered for a comprehensive system design, including climatic conditions (air temperature, heating and cooling demands, peak demand, operation plan), building physics (insulation thickness, window size), and installation details (available space, position of the header block, heat pump, and technical service center) (Brandl, 2006).

On the structural and geotechnical side, the design must address the additional thermal stresses and strains arising from the heating and cooling of the piles. These thermal effects can cause expansion and contraction, potentially leading to fatigue or failure if not properly managed (Bourne-Webb et al., 2009). This consideration may necessitate adjustments in pile configuration and spacing to avoid thermal interference and enhance thermal performance. Additionally, thermal processes in the ground can lead to soil expansion or contraction, freezing or thawing, changes in pore water pressure, effective stress, shear resistance, and load-bearing capacity of piles, potentially causing settlements in buildings. While previous studies have indicated that thermally induced settlements are generally negligible, they must be considered for buildings that are highly sensitive to differential settlements (Brandl, 2006).

2.4.2.3. Numerical modeling

Several authors have used numerical simulations for the design and analysis of energy piles and micropiles (Cecinato & Salciarini, 2022; Gao et al., 2008; Gashti et al., 2014; Katzenbach et al., 2008; Laloui et al., 2006; Lupattelli et al., 2023; Park et al., 2013; Suryatriyastuti et al., 2013). Advanced computational tools enable detailed simulation of the thermo-mechanical interactions between the piles and the surrounding soil. Such models are crucial for predicting system behavior under various loading conditions, including thermal cycling, mechanical loads, and different operational modes.

Finite element modeling (FEM) is commonly used to simulate the complex interactions between the structural and thermal aspects of energy piles. FEM can effectively model heat transfer processes, including conduction, convection, and radiation, along with mechanical responses such as stress distribution, deformation, and potential failure points. These simulations provide critical insights into the performance and reliability of energy piles, allowing engineers to optimize designs and identify potential issues before construction begins. Additionally, numerical models can integrate site-specific data obtained from thermal response tests (TRT) and geotechnical investigations, resulting in more accurate and customized designs. By simulating various scenarios and design configurations, engineers can assess the impact of different parameters on system performance, leading to more informed and effective design decisions. Moreover, numerical simulation can evaluate the long-term effects of thermo-active deep foundations on adjacent soil properties and groundwater. This is increasingly important as local authorities demand calculations of temperature distribution in the ground due to energy foundations for environmental risk assessments (Brandl, 2006). These simulations help ensure that the environmental impact is minimized, maintaining the integrity of surrounding ground conditions and groundwater over the lifespan of the project. Hence by utilizing these advanced modeling techniques, engineers can design more efficient and reliable energy piles and micropiles, ensuring their structural integrity and thermal performance meet the required standards while mitigating potential environmental risks.

2.4.3. Heat transfer mechanisms in energy piles and micropiles

Energy micropiles (EMPs) facilitate heat exchange with the surrounding ground through the temperature gradient that exists between them. This process continues until thermal equilibrium is achieved, at which point the heat exchange stabilizes. However, the persistent temperature difference between the inlet and outlet heat carrier fluids ensures a steady and efficient heat transfer (Sani et al., 2019). Like energy piles, geothermal energy micropiles (EMPs) rely on three primary heat transfer mechanisms as illustrated in Figure 2.10:

- Thermal convection: this occurs between the fluid (A) and the pipe wall (B).
- Thermal conduction: this process happens within various materials including the pipe (B), steel (D), and grout (E).
- Thermal conduction in the ground (F): this mechanism facilitates the transfer of heat through the soil surrounding the micropiles.

Additionally, other thermal phenomena might take place, such as thermal radiation at the soil surface and convective heat transfer within the pore water when groundwater is moving (Cecinato & Loveridge, 2015). A unique aspect of energy micropiles is the hollow nature of their reinforcement, which introduces another layer of heat transfer. In coaxial pipe configurations (Figure 2.11), heat transfer occurs within the space between the walls of the hollow tube and the pipe. The filling material, usually the heat carrier fluid, enhances convective heat transfer (C) due to the large volume of water in the pipe (Jalaluddin et al., 2011). For configurations like U-tube and multi-tube pipes (Figure 2.11), the space between pipes is often filled with grout, silica sand, or mortar. In these cases, heat transfer predominantly occurs through conduction in solids or porous media (Jalaluddin et al., 2011; Lautkankare et al., 2020; Ronchi et al., 2018; Ciardi et al., 2023).

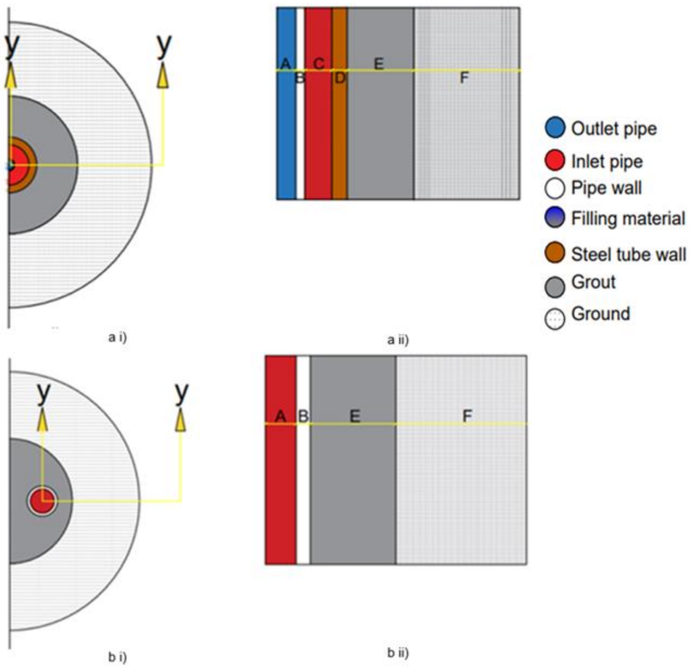

Figure 2.10: *Heat transfer mechanisms within energy micropiles (a) and energy piles (b) and the ground. Plan view (a i,b i,) and section y-y (a ii, b ii).*

2.4.4. Thermal performance of energy micropiles

The performance of geothermal energy micropiles (EMPs) is influenced by several critical design parameters, notably pile length, concrete thermal conductivity, and pipe diameter (Cecinato & Salciarini, 2022). Pile length and concrete thermal conductivity are well-established factors in the design of energy piles (EPs) as well (Cecinato & Loveridge, 2015). However, for EMPs, the pipe diameter also plays a significant role due to the large surface area occupied by the pipes, which directly affects thermal performance. Unlike EPs, the performance of EMPs is minimally impacted by the number of pipes they can accommodate, given their smaller size constraints. To date, only U-shaped pipes and coaxial pipes have been used in energy micropiles, whereas energy piles can utilize a broader range of pipe configurations (Figure 2.11). To avoid thermal interference between the pipes, a minimum shank spacing of 25 mm is required. Increasing this spacing can further enhance thermal performance. Spacers can be used to maintain the minimum distance, thereby reducing thermal interference and resistance (Gerola et al., 2023). In the coaxial annular (centered) pipe configuration (E in Fig 2.11), the pile itself serves as the inlet (outlet pipe) and a central pipe serves as the outlet (inlet pipe). This setup is particularly recommended for energy micropiles due to an expanded surface area for efficient heat exchange and enhanced heat transfer facilitated by convective heat transfer from the substantial volume of water within the pipe. Compared to U-shaped pipes, this configuration results in a higher heat exchange rate (Jalaluddin et al., 2011). Moreover, the micropile can be used as a thermal storage tank thanks to the considerable amount of heat required to increase the temperature of the water inside the pile, as water has a high specific heat capacity (Abbasi & Abbadi, 2022; Jalaluddin et al., 2011).

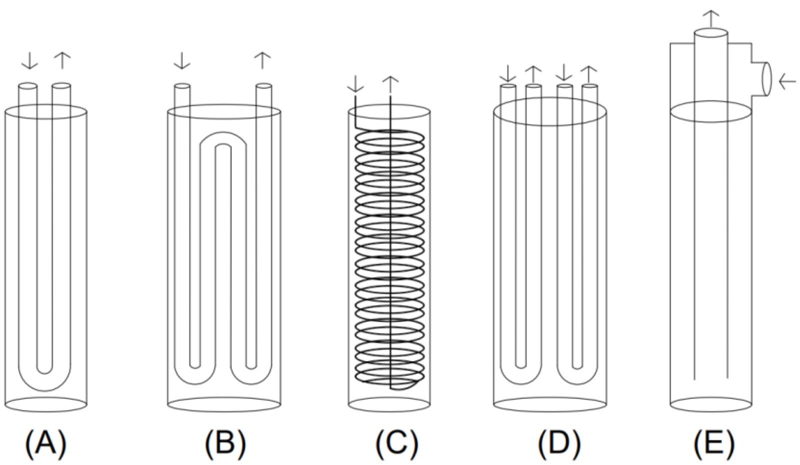

Figure 2.11: *Examples of pipe configurations for energy piles: (A) U-shaped pipe, (B) W-shaped pipe, (C) spiral or helix pipe, (D) double U-shaped pipe, (E) coaxial pipe.*

Energy micropiles (EMPs) exhibit specific heat flux values typically ranging between 30 W/m and 50 W/m, which are comparable to those of energy piles (EPs) that range between 20 W/m and 80 W/m (Ronchi et al., 2018). However, these values can be higher depending on several factors. For instance, tests conducted on TITAN 73/53 energy micropiles installed in wet sediments showed a heat extraction capacity of about 111 W/m, surpassing the double-U-pipe energy wells which had a heat extraction capacity of approximately 105 W/m. In another test conducted in Hamburg, specific heat flux values between 60 W/m and 80 W/m were observed (Friedr. Ischebeck GmbH, 2014) . Several factors contribute to the variations in specific heat flux:

- Soil Properties: The thermal conductivity of the soil significantly impacts the specific heat flux, playing a dominant role in maximizing the performance of EMPs (Ronchi et al., 2018).
- Temperature Differences: The difference between the inlet water temperature and the ground temperature is critical. For example, an increase in the inlet water temperature by +10°C was observed to increase the heat exchange power of a steel energy micropile by approximately 1 kW (Kong et al., 2021).
- Operation Modes and Cycles: Continuous operation modes lead to a rapid increase in pile temperature during early stages which is not recovered over time, affecting efficiency (Ren et al., 2020). Intermittent operation modes, however, result in higher efficiency and performance (Ren et al., 2020; You et al., 2014).
- Inlet Fluid Velocity: While an increase in inlet fluid temperature and velocity can enhance heat exchange rates in summer, it can also raise the pile temperature and operation costs (Kong et al., 2021; You et al., 2014).

The specific heat flux of EMPs tends to be insensitive to variations in mass flow rate, pipe material, and the material used to fill the tank (Ronchi et al., 2018). EMPs are effective irrespective of whether the space above the foundation is indoors or outdoors, as the impact of air temperature on the exchanged power is minimal. However, the presence of an insulating layer between the ground and the building space above can reduce the thermal efficiency of EMPs (Cecinato & Salciarini, 2022) . This characteristic makes EMPs suitable for retrofitting old buildings that typically lack modern exterior insulation solutions (Cecinato & Salciarini, 2022).

The performance of energy micropile systems can be significantly affected by the configuration and number of micropiles in a group. While increasing the number of micropiles in a group generally enhances the overall heat exchange rate of the geothermal system, it also introduces complexities that need to be addressed in the design phase. Increasing the number of micropiles in a group results in a higher total heat exchange capacity due to the collective thermal contribution of each individual micropile (Kong et al., 2021). This increase in overall heat exchange rate stems from the fact that each additional micropile contributes to the heat extraction or dissipation process, thereby improving the efficiency of the geothermal system as a whole. However, it is important to note that this increase in total heat exchange capacity comes with a trade-off: as the number of micropiles increases, the average heat exchange rate per individual micropile decreases (Kong et al., 2021). In their study, (Kong et al., 2021) found that the position of energy micropiles within a group had a negligible impact on the average heat exchange rate of each micropile, provided that all micropiles were uniformly distributed around the boundary of the raft. However, this observation is specific to the configuration where micropiles are arranged at the perimeter of the foundation. It is essential to recognize that this finding might not extend to all configurations, as the thermal performance can vary with different arrangements of micropiles within the group.

One critical consideration in the design of energy micropile groups is the phenomenon of thermal interference. When micropiles are placed too closely together, the heat exchange processes between adjacent piles can interfere with one another, leading to a significant reduction in the overall efficiency of the system (Lupattelli et al., 2023). This thermal interference results from overlapping thermal influence zones, where the heat extracted or dissipated by one micropile affects the performance of its neighbors. Previous studies have highlighted the importance of managing this thermal interference. (Salciarini et al., 2015) observed that the efficiency of a central pile in a group diminished over time as the temperature gradient around the central pile became negligible, leading to reduced thermal performance. This finding underscores the need for careful consideration of pile spacing and arrangement to prevent significant thermal interference. Moreover, Lupattelli et al. (2023) emphasize that closely spaced micropiles can experience thermal interference that compromises their functionality over time. This issue is particularly pertinent when designing systems for long-term applications where sustained thermal performance is crucial. The thermal influence radius, which defines the distance within which the heat exchange from one pile affects another, varies depending on construction materials and installation methods. For example, (You et al., 2014) reported a thermal influence radius of approximately 4 meters for cement-fly ash-gravel (CFG) piles, which is larger compared to the 2-meter radius observed by (Bourne-Webb et al., 2009) for bored piles. This variation highlights the significant impact of material properties and construction techniques on the thermal performance of energy piles and micropiles (Kong et al., 2021). Hence, to ensure that the structural integrity and thermal efficiency of the energy micropile system are maintained, it is essential to integrate careful design considerations.

2.4.5. Thermo-mechanical behavior of energy micropiles

A thorough understanding of the thermo-mechanical behavior of these energy piles and micropiles is important for optimizing their design and ensuring their long-term performance. This section reviews the complex interactions between thermal and mechanical loads in energy micropiles, building on the foundational principles established for energy piles.

2.4.5.1. Conventional piles subjected to thermo-mechanical loads

When subjected solely to downward vertical loading, traditional vertical foundation piles experience compressive forces. These forces cause the pile to settle into the underlying soil, with resistance occurring at the interface between the pile and the soil. This resistance counteracts the applied load, assuming the load is primarily borne by the pile shaft. The resistance remains relatively consistent along the shaft length, implying a uniform rate of change in axial load with depth (Bourne-Webb et al., 2009, 2012), as illustrated in Figure 2.12a. Therefore, both mechanical strains and mechanical loads decrease linearly with depth and can be mathematically expressed as follows (Amatya et al., 2012):

$$\varepsilon_M = \frac{\Delta L_M}{L} \tag{2.31}$$

$$P_M = -EA\varepsilon_M \tag{2.32}$$

where ΔL is the deformation due to the mechanical load, L is the original pile length, E the Young's modulus, and A the cross-sectional area of the pile.

When heated, piles expand, and the axial strain induced in a free-standing homogeneous concrete column varies linearly with its thermal characteristics according to the equation (Amatya et al., 2012):

$$\varepsilon_{T-Free} = \alpha_c \Delta T \tag{2.33}$$

where ε_{T-Free} describes the free axial thermal strain in the absence of restraint, α_c denotes the coefficient of isotropic thermal expansion or contraction of concrete and ΔT represents the net temperature change experienced by the pile.

However, in the ground, foundation piles cannot expand freely due to restraints at the top by the superstructure, at the toe by a stiff bearing layer, and/or at the side by the surrounding soil. These restrained axial strains (ε_{T-Rstr}) produce thermal stresses in the pile and must be considered during structural design. These stresses are estimated as follows (Amatya et al., 2012; Bourne-Webb et al., 2009):

$$\varepsilon_{T-Rstr} = \varepsilon_{T-Free} - \varepsilon_{T-Obs} \tag{2.34}$$

where ε_{T-Obs} is the observed axial strain.

Given a specific increase in axial strain caused by temperature variation, the thermally induced axial load can be approximated using the following equation (Amatya et al., 2012):

$$P_T = -EA\varepsilon_{T-Rstr} = -EA(\alpha_c \Delta T - \varepsilon_{T-Obs}) \tag{2.35}$$

where E refers to the Young’s modulus of the pile material, while A denotes the pile cross-sectional area. The negative sign indicates that the restrained strain resulting from the interaction between the pile and the soil acts as a counterforce, limiting the deformation of the pile.

As soil stiffness and strength increase, so do the restraints provided by the soil, leading to a decrease in expansive strains in the pile when heated and an increase in the resulting compressive axial load. This, in turn, increases the axial load in the pile (Amatya et al., 2012; Bourne-Webb et al., 2009, 2012; Salciarini et al., 2015, 2017). The magnitude of these loads depends on soil characteristics. For a floating pile in uniform soil, the axial load will be largest at mid-depth (Amatya et al., 2012; Bourne-Webb et al., 2009, 2012) (Figure 2.12b.). Conversely, during cooling, the opposite phenomenon occurs, as shown in Figure 2.12c. Mechanical loads decrease with depth, while thermal loads propagate more within the soil (Laloui et al., 2006). At the pile base, thermal effects can induce significantly higher axial stresses compared to the minimal stresses caused by the building's weight. Unlike heating, cooling leads to contraction and the development of tensile loads (Amatya et al., 2012; Bourne-Webb et al., 2009; Salciarini et al., 2015, 2017). Higher soil stiffness results in increased compressive and tensile loads for both heated and cooled piles (Bourne-Webb et al., 2009).

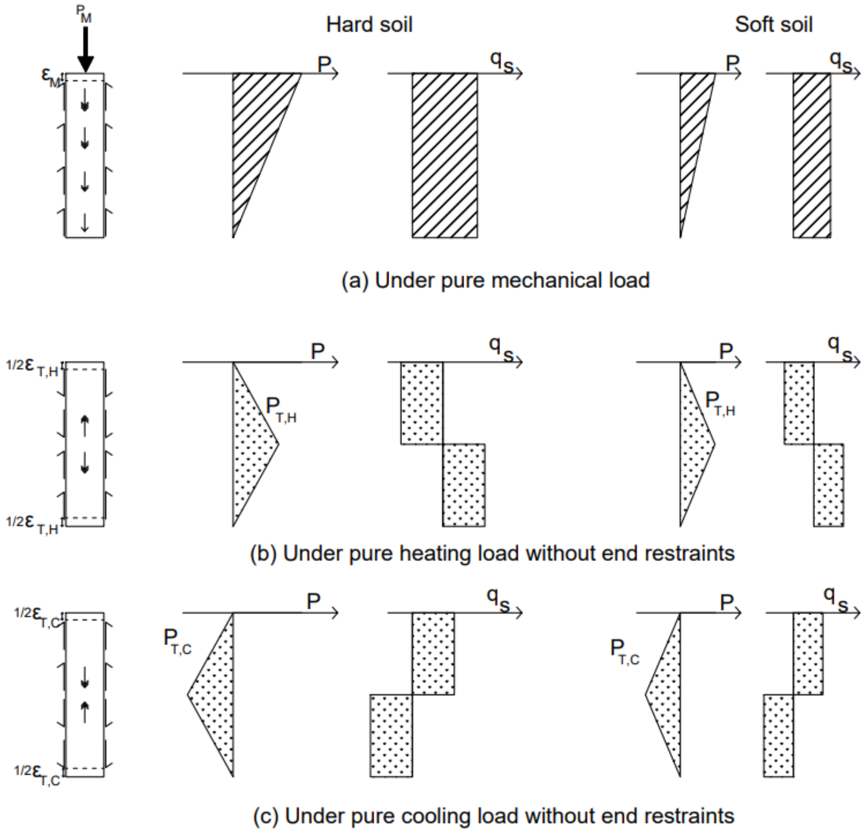

Figure 2.12: *Mechanisms for response of piles to pure mechanical, cooling and heating loads, without end restraints (adapted from Amatya et al., 2012; Bourne-Webb et al., 2009; Sani et al., 2019).*

Restraints, whether from the soil or the ends, are crucial in the design of energy piles. End restraints significantly increase compressive loads in heated piles and tensile loads in cooled piles (Figure 2.13a and Figure 2.13b). If an additional axial load is applied, the compressive load on the heated pile further increases (Figure 2. 13c). However, the compressive axial load will decrease the tensile load on the cooled pile, resulting in tension at the bottom and compression at the top (Figure 2.13d) (Bourne-Webb et al., 2009, 2012).

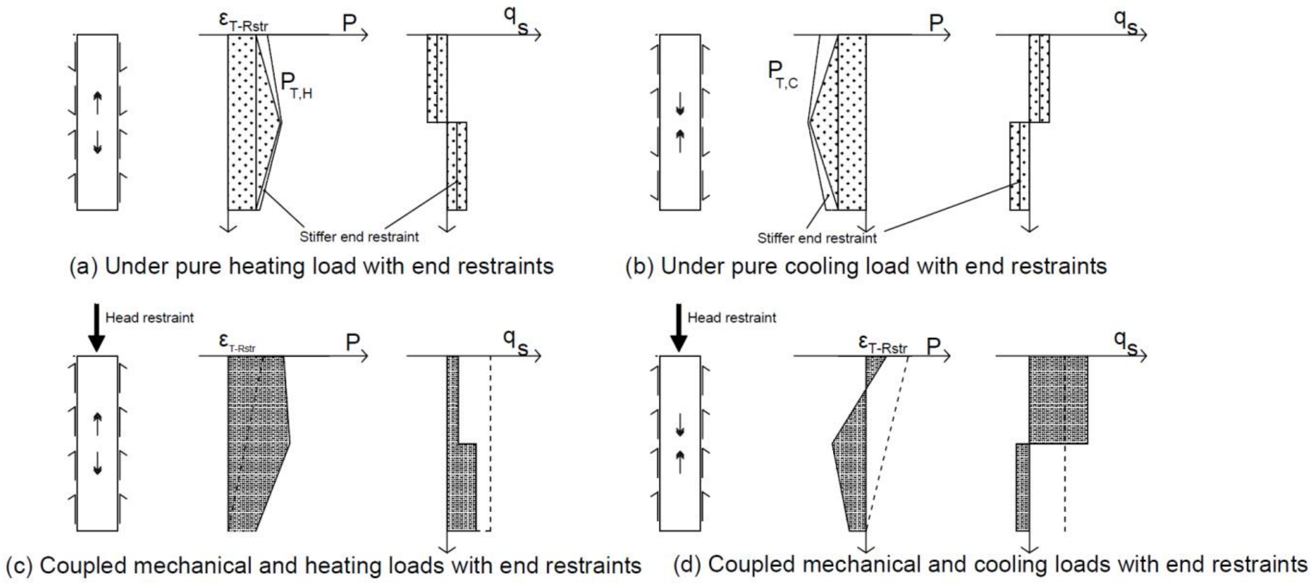

Figure 2.13: *Mechanisms for response of piles to pure heating, pure cooling and coupled thermo-mechanical loads with end-restraints (adapted from* Bourne-Webb et al. (2009, 2012 *).*

The strain profiles observed during the heating and cooling of energy piles indicate predominantly thermo-elastic behavior. This means that variations in the pile's response during thermal cycles are primarily due to the pile's contraction or expansion, and these effects appear to be reversible (Bourne-Webb et al., 2009; Laloui et al., 2006). However, the response at the pile head remains thermo-elastic only if the mechanical load is below 40% of the ultimate resistance. Beyond this threshold, irreversible settlement develops (Tang et al., 2013). Temperature fluctuations within the pile can increase or decrease shaft resistance, primarily influenced by the axial head load (Amatya et al., 2012; Bourne-Webb et al., 2009, 2012).

Energy piles are often installed in groups, which necessitates considering "group effects" for efficient foundation design. Increasing the number of thermally loaded piles not only increases vertical strains (Rotta Loria & Laloui, 2017) and displacements (raft movements) (Salciarini et al., 2017), but also significantly alters pile behavior, particularly in soils with higher thermal expansion coefficients than the piles themselves. Generally, piles under heating thermal loads experience compressive stresses. However, during prolonged operation, if the soil's thermal expansion coefficient surpasses that of the piles, a reduction in compressive loads may occur (Salciarini et al., 2017), potentially resulting in tensile stresses (Rotta Loria & Laloui, 2018). Therefore, it is crucial to thoroughly assess the geotechnical properties of the site (Rotta Loria & Laloui, 2018).

The presence of multiple thermo-active elements can lead to variations in the depth of the foundation slab by more than 2 cm compared to those induced by mechanical loading alone (Salciarini et al., 2017). Differences in the temperature of piles within a group, such as those due to series connections, can result in differential settlement and pile cap tilt (Fang et al., 2022). Closely packed energy piles may experience reduced performance due to interference effects (Salciarini et al., 2017), and the thermal influence on the ground can be greater (Katzenbach et al., 2008).

In energy piles constructed within loose soil layers, repeated thermal cycles can induce residual contractive strains and compressive stresses, which intensify with an increasing number of cycles and may exceed the theoretical maximum thermal stress limit (Fang et al., 2022). Traditional piles experience cyclic changes in normal stress due to interactions among adjacent piles (Suryatriyastuti et al., 2013). Interestingly, studies have demonstrated that cyclic heating, as opposed to steady heating, can mitigate thermal interactions among energy piles within a group. (Faizal et al., 2022). This finding could be advantageous for the design and implementation of closely spaced energy piles in practical settings.

2.4.5.2. Thermo-mechanical behavior of energy micropiles

Energy micropiles (EMPs) are a relatively new development in the field of energy geostructures, and there is limited research on their thermo-mechanical behavior. A key aspect influencing EMPs is the significant role of side shear resistance due to insufficient cleanout at the toe, which primarily governs the restraint for thermal expansion and contraction (Casagrande et al., 2022). In granular soils subjected to cyclic thermal loading, initial cooling cycles can lead to irreversible settlement, though these settlements are typically negligible and can be ignored in design considerations (Lupattelli et al., 2023). However, the behavior of EMPs becomes more complex in stratified soils. Thermal response tests have shown that different soil layers affect the thermomechanical response of EMPs differently. For instance, plastic strains develop in organic clay layers upon heating, while silty sand and sand layers retain thermo-elastic behavior (Casagrande et al., 2022). The mobilized coefficient of thermal expansion for EMPs decreases with each heating cycle, corresponding to increased side shear resistance and restraint along the pile length, and this coefficient varies with depth, being minimal in organic clay layers.

Thermal loading induces axial stresses in EMPs, which increase with both the inlet fluid temperature and the number of thermal cycles (Casagrande et al., 2022; Kong et al., 2021).

Long, slender micropiles exhibit significant compressive stresses (Lupattelli et al., 2023) .In micropile groups, thermal compression stresses in heated EMPs can be about three times those in non-heated piles (Kong et al., 2021). These thermal stresses tend to increase over time but may dissipate at the end of a thermal cycle if an intermittent operational mode is employed (Ren et al., 2020). Continuous heating can induce additional compressive stresses of about 200 kPa/°C (Ren et al., 2020), higher than those reported for traditional energy piles (Bourne-Webb et al., 2009; Laloui et al., 2006). Fully restrained EMPs can reach compressive stresses up to 508 kPa/°C (Ren et al., 2020), significantly exceeding the 340 kPa/°C observed in energy piles (Bourne-Webb et al., 2009). Thermal loads can also lead to differential settlement, with displacements in EMPs being larger than in non-energy piles, necessitating careful consideration of thermally induced stresses and displacements during structural design (Kong et al., 2021).

Currently, most studies focus on EMPs with U-pipe configurations, and there is a notable gap in research on the thermo-mechanical behavior of coaxial energy micropiles. One commercial example, the TITAN 73/53 self-drilled energy micropile by Friedr. Ischebeck GmbH, utilizes coaxial pipe configuration and offers several structural advantages, such as rapid construction, cost efficiency, permanent corrosion protection, suitability for all soil types, minimal structural deformation without prestressing, and resistance to tensile, compressive, and cyclic loads (Friedr. Ischebeck GmbH, 2016, 2022).

2.4.6. Comparison between energy piles and micropiles

Energy piles and energy micropiles are innovative solutions for harnessing geothermal energy for heating and cooling buildings. Both systems integrate geothermal loops within foundation elements, sharing similarities in thermal and structural behavior while also presenting distinct differences due to variations in size, material composition, and mechanical behavior. This section provides a detailed comparison of these two technologies, focusing on their similarities and differences in thermal and mechanical behavior, installation processes, design considerations, and operational efficiency.

2.4.6.1. Similarities between energy piles and micropiles

Energy micropiles and conventional energy piles share fundamental characteristics that significantly influence their thermal and structural performance over their operational lifespan. Both types of piles experience a gradual decline in thermal efficiency due to repeated thermal cycles, which diminishes their heat exchange rate. Factors such as groundwater presence, soil thermal conductivity, seasonal temperature variations, and the temperature gradient between soil and the heat exchange fluid collectively influence their thermal performance and overall system efficiency.

Thermal expansion and contraction are prominent characteristics observed in both energy micropiles and conventional energy piles. During heating, these piles expand, while cooling induces contraction, resulting in additional thermal stresses—compression under heating and tensile stresses during cooling. Effective design and operational strategies must carefully consider these thermal stresses to prevent potential structural damage and ensure long-term reliability. Intermittent operation proves advantageous for both energy micropiles and conventional energy piles compared to continuous operation. Intermittent modes allow for the dissipation of accumulated heat, resetting thermal conditions and thereby sustaining efficiency over extended periods. However, an increase in the number of energy piles or micropiles within a foundation can lead to increased settlement during cooling and heave during heating due to cumulative thermal effects. Moreover, over time, central energy piles or micropiles within a group tend to exhibit reduced thermal efficiency compared to perimeter piles. This underscores the critical importance of thoughtful layout and design to optimize the performance of energy geostructures in various applications. By comprehensively understanding and managing these shared characteristics, engineers can enhance the resilience and longevity of energy piles and micropiles in geotechnical and structural designs.

2.4.6.2. Differences between energy piles and energy micropiles

In geotechnical engineering, the distinction between piles and micropiles is crucial, highlighting their specialized roles despite sharing fundamental characteristics. Energy piles, with diameters ranging from 600 to 1500 mm, are robust structures primarily used in new building foundations. Constructed from reinforced concrete, they offer high load-bearing capacity and resilience against mechanical forces. In contrast, energy micropiles, ranging from 100 to 300 mm in diameter, are generally grouted and adapted for underpinning existing structures, retrofitting, and slope stabilization. While both energy piles and micropiles serve as integral components of energy geostructures, their differences in size, construction methods, and mechanical behavior shape their suitability for specific engineering challenges. These differences have been summarized in Table 2.15.

Table 2.15: *Differences between energy piles and energy micropiles (Yozy Kepdib et al., 2025a).*

Aspects	Energy micropiles	Energy piles
Application	New foundations, underpinning, retrofitting, soil retention, slope stability.	New foundations
Diameter	100 - 300 mm	600 – 1500 mm
Construction materials	Grout/mortar	Reinforced Concrete
Group installation	Closely packed, higher thermal interference	Larger distances between piles
Pipe configuration	Mainly U-pipes and coaxial pipes	U-pipes, coaxial pipes, W-pipes, double U-pipes, spiral pipes
Pipe diameters	12 - 20 mm	Can be more than 20 mm
Pipe spacing	Smaller, < 50 mm, greater possibility of thermal interference.	Larger, 100 - 300 mm
Temperature response	Rapid temperature changes rapidly at early stages of operation	Slower temperature change
Thermal influence radius	Can reach 4 m	Smaller, 2 – 3 m
Most influential thermal performance design parameters	Micropile length, concrete thermal conductivity, pipe diameter	Number of pipes, pile length, concrete thermal conductivity, pile diameter
Average thermal output	Lower, < 50 W/m	Between 20 and 80W/m
Bearing capacity	High friction capacity, negligible end – bearing capacity	Both friction and end bearing capacity.
Load carrying capacity	Load mainly carried by the reinforcement	Load mainly carried by the concrete
Thermal stresses	Larger additional compressive and tensile stresses, up to 200 kPa/°C.	Smaller additional compressive and tensile stresses, less than 200 kPa/°C

2.4.7. Environmental impact and sustainability

The environmental impact assessment (EIA) of energy micropiles is crucial in evaluating their sustainability and minimizing their ecological footprint within construction projects. Energy micropiles, like energy piles, offer significant potential benefits by harnessing geothermal energy for heating and cooling, thereby reducing dependence on conventional energy sources and lowering associated greenhouse gas emissions. Ground source heat pump systems typically achieve high coefficients of performance (COP), ranging from 3 to 5, surpassing those of conventional electric heaters and boilers (around 1) (Sadeghi et al., 2022). Hence, energy micropiles offer substantial energy efficiency gains, contributing to environmental sustainability by minimizing overall energy consumption.

Moreover, energy micropiles serve dual roles in structural support and energy rehabilitation of buildings, which reduces costs and environmental impacts associated with conventional energy well drilling. Unlike traditional methods, micropile installation generates less spoil and disturbance to surrounding soil and habitats (Sabatini et al., 2005). However, potential negative impacts such as groundwater contamination, noise, and vibration during drilling processes must be carefully managed (Ren et al., 2020). Environmental risks like groundwater contamination can be mitigated using environmentally safe materials and adherence to rigorous installation protocols, while advancements in drilling technologies and scheduling can minimize noise and vibration impacts on local communities.

In general, the use of geothermal energy may lead to excessive groundwater cooling, which can elevate pH levels and reduce calcium solubility, potentially leading to pore clogging. Ground water cooling also increases the solubility of gaseous substances like CO_2 and the hardness of groundwater (Brandl, 2006). Biological impacts are significant, as temperature fluctuations below 10°C can substantially reduce the activity of microorganisms, impacting pathogen mortality rates in groundwater (Brandl, 2006).

Regular monitoring and maintenance throughout the micropiles' lifecycle are essential to identifying and addressing any environmental concerns promptly. By implementing sustainable construction practices and conducting comprehensive EIAs, the environmental impacts of energy micropiles can be effectively managed, ensuring their long-term viability as a renewable energy solution.

2.4.8. Technological innovations and advancements

Technological innovations in energy micropiles have enhanced their efficiency and environmental sustainability. Initially developed as specialized foundation solutions, energy micropiles have evolved into dual-functioning structures that provide structural support while efficiently managing thermal energy.

Innovative drilling technologies have also revolutionized the installation process. Self-drilling micropiles minimize site materials and construction time allowing installation in challenging urban environments.

Furthermore, advancements in geothermal heat exchange systems have significantly improved the thermal efficiency of energy micropiles. Many researchers have studied the possibility of increasing the thermal conductivity of grouts used in micropiles using additives like sand, graphite, axilat (Allan & Kavanaugh, 1999; Allan & Philippacopoulos, 1998; Ciardi et al., 2023; Maatouk, 2016; Śliwa et al., 2017) .These improvements result in higher energy extraction rates and improved performance of energy micropiles, promoting energy savings and environmental sustainability.

2.5. Summary

This chapter has provided an in-depth exploration of micropiles and energy micropiles, covering their types, classifications, and key design considerations. The fundamental principles of ultimate limit state (ULS) and serviceability limit state (SLS) designs, with a focus on axial bearing capacity and structural failures, were examined. The integration of geothermal energy systems with these foundation elements was discussed, highlighting the mechanisms of heat transfer and the thermal performance of energy micropiles. Additionally, a comparion between energy piles and micropiles was presented, as well as the environmental impact of energy micropiles.

3. Experimental work

3.1. Introduction

This chapter presents the experimental investigation carried out to evaluate the thermal performance and thermo-mechanical behavior of energy micropiles designed for low-enthalpy geothermal energy extraction. The main objectives are to assess the efficiency of energy micropiles for building heating and cooling applications and to analyze their in-situ response under thermal and combined thermo-mechanical loading.

The experimental campaign was conducted at the NTNU Dragvoll test site in Trondheim, where six micropiles were installed in different clay conditions. The micropiles were equipped with innovative heat-exchange pipe configurations - a split pipe and a corrugated coaxial pipe - and instrumented with temperature and strain sensors at various depths. The testing program included mechanical, thermal, and thermo-mechanical loading scenarios. Details of the test setup, instrumentation, procedures and results are presented in the following sections.

3.2. Site description and soil investigation

The experimental site for this study is located at the Dragvoll campus of the Norwegian University of Science and Technology (NTNU) in Trondheim, Norway. Trondheim, the largest city in the Trøndelag region, is situated at the confluence of the river Nidelva and the Trondheimsfjord, offering a diverse range of geological and climatic conditions (Figure 3.1a). The city, with a population exceeding 200,000, serves as the central hub of the Sør-Trøndelag county, nestled in Central Norway. Dragvoll campus is situated in the eastern part of Trondheim, at approximately 63.4°N latitude and 10.5°E longitude. The site's proximity to both coastal and inland geographical features influence its geological makeup, which includes a mix of glacial deposits such as silty clays and sandy soils.

Trondheim experiences a predominantly Oceanic climate (Köppen: Cfb), though it borders on humid continental, sub-polar oceanic, and subarctic climates (Tveito & Lundstad, 2016). Winters in Trondheim are long and cool, characterized by moderate snowfall from November to March. The city experiences an average of 14 days per winter with at least 25 cm of snow cover and 22 days with minimum temperatures of -10°C or lower (Tveito & Lundstad, 2016). Summers, while relatively short, bring milder conditions, with July being the warmest month. The climate is also marked by considerable variability, with the wind playing a significant role in weather patterns. March is typically the windiest month, with an average wind speed of 3.0 m/s, while July and August are the calmest, with average wind speeds of 2.1 m/s (Brozovsky et al., 2021). The average temperature and precipitation values in Trondheim for the period 1971-2000 are reported to be 5.5°C and 950 millimeters. (Norsk Klimaservicesenter, 2022). Hydrogeologically, the Dragvoll area features a shallow water table influenced by the low-permeability clay layers that are common in the region. The site itself is easily accessible, being well-connected by major roads and public transportation, which facilitated the conduction of the in-situ experiments (Figure 3.1b).

(a)

(b)

Figure 3.1: *Testing site.*

The soil at the test site primarily consists of marine deposits as shown in the soil map produced by the Geological Survey of Norway, NGU (Figure 3.2a). Several ground investigation campaigns have been carried out at the test site; however, the associated reports are not publicly available. This thesis utilizes laboratory and field test results conducted by master's students at the Norwegian University of Science and Technology (NTNU) (Magnussen et al., 2024; Simonhjell, 2024) to determine the ground conditions. The locations of the boreholes investigated are shown in Figure 3.2. The micropiles were installed between BP3 and BP1, but closer to BP2. Their position is highlighted with a red rectangle.

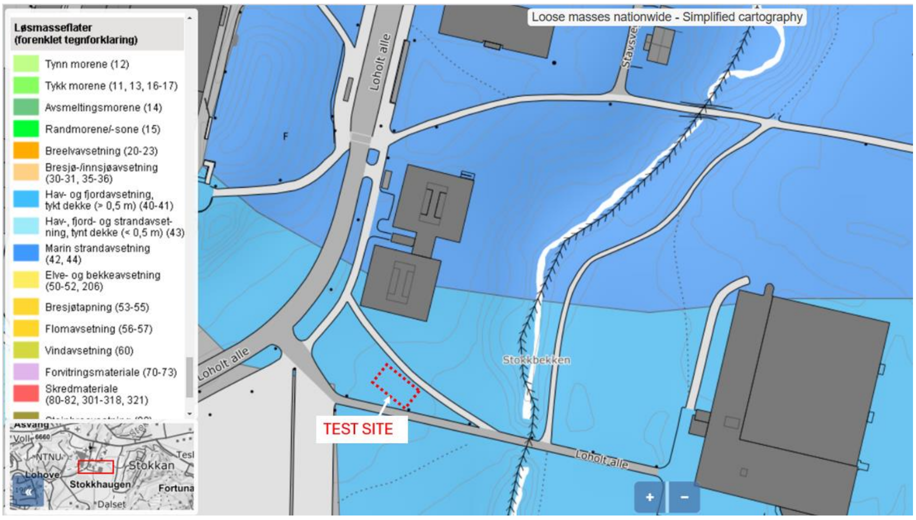

(a)

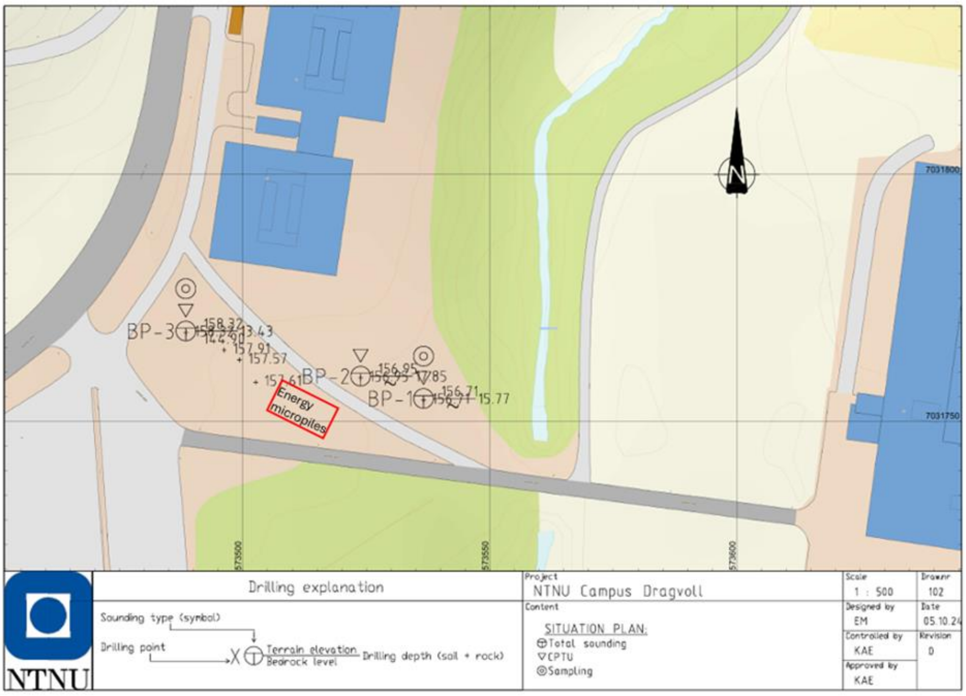

(b)

Figure 3.2:*Soil investigation. (a) Geological map by NGU (b) Position of boreholes and micropiles (modified from Simonhjell, 2024).*

Resistivity cone penetration test with pore water measurement (RCPTU) results presented by Simonhjell (2024) report the presence of quick clay at depths below 15 m, which is further confirmed by index laboratory tests. Samples retrieved from 5 - 6 m depth consisted of clay mixed with sand or silt and some organic matter. Between 11 m and 12 m, the soil appeared to be silt with sand, with possible clay content at the bottom. A sample from 19 - 20 m was identified as quick clay. Grain size distribution analysis suggests the soil is predominantly silty clay from 5 to 19 m. Additionally, bulk resistivity tests on samples within this range yielded values consistent with quick clay.

Further testing conducted by NTNU Master students (Magnussen et al., 2024) revealed the following from CPTU data: the upper 4 m comprises cohesive and silty materials; between 5 and 11 m, the soil is primarily silty clay to clay; below 11 m, the layer is cohesive, clay, potentially sensitive clay. Additional tests such as index tests, triaxial tests, and oedometer tests were also performed. These indicated that the soil consists of dry crust to 0.8 m, silty clay from 0.8 to 4.0 m, and quick clay from 4.0 to 13.425 m. Due to some inconsistencies in the reported data, it is challenging to define the stratigraphy precisely. However, a reasonable approximation of the soil profile at the test site is provided below: the test site may be assumed to be constituted of dry crust (0 – 2 m) in the uppermost layer, followed by silty clay from 2 to 6 m, clay between 6 m and 11 m, sensitive clay between 11 m and 15 m, and quick clay in the lower layers.

Table 3.1: *Soil stratigraphy at the test site*

Soil type	**Depth [m]**
Dry crust	0.0 - 2.0
Silty clay	2.0 - 6.0
Clay	6.0 - 11.0
Sensitive clay (possibly quick clay at lower depths)	11.0 - 20.0

Both investigation reports indicate a shallow groundwater table at 0.8 m depth, suggesting saturated soil. Laboratory tests confirmed this with saturation degrees exceeding 96 % between depths of 5 m to 17 m. The water content ranged from 26.33 % at 5 m to 32% at 17 m. Void ratio values ranged between 0.72 and 0.90, with porosity between 42 % and 47.3 % (Simonhjell, 2024). Simonhjell (2024) also reported average soil densities between 1.97 g/cm^3 and 2.02 g/cm^3, and unit weights from 19.37 to 19.91 kN/m^3 consistent with saturated clay, typically ranging from 17 to 21 kN/m^3. The undrained shear strength c_u varies with depth. Simonhjell (2024) reports a peak value of 54.15 kPa at 5.32 m to 5.71 m depth, which reduces to 28.17 kPa at 11.32 m to 11.71 m, and further to 17.6 kPa at 19.32 m to 19.71 m for BP 7. Lower values were recorded for BP 75, with 25.94 kPa at depth 12.32 m to 12.71 m and 16.86 kPa at 17.32 m to 17.71 m (J. Simonhjell, 2024). These values correspond to the typical shear strength values of soft clay. The thermal conductivity and constant heat capacity were measured to be 1.5 W/mK and $3 * 10^6\ J/m^3K$ (Magnussen et al., 2024). The values of c_u with the corresponding depths and other ground properties are reported in Tables 3.2 and 3.3 respectively.

Table 3.2: *Shear strength of soil at various depths*

Depth [m]	**c_u [kPa]**
5.32 -5.71	54.15
11.32 -11.71	28.17
12.32 -12.71	25.94
17.32 -17.71	16.86
19.32 -19.71	17.6

Table 3.3: *Other ground properties*

Properties	Value
Thermal conductivity [W/(mK)]	1.5
Heat capacity [J/ (m^3K)]	$3 * 10^6$
Density [kg/m^3]	1995
Porosity	0.45

3.3. Materials

The experimental setup for evaluating the thermo-mechanical behavior of energy micropiles at the Dragvoll campus relies on a carefully selected array of materials to ensure accurate data collection and reliable performance.

3.3.1. Hollow bar

The TITAN threaded hollow bar (Figure 3.3), manufactured by Friedr. Ischebeck GmbH is a key component of the setup. It is made from fine-grained structural steel S 460 NH, which offers a high notched impact strength $W \geq 40$ Joules at -20°C, greater than the impact strength of typical structural and prestressing steel, which are 27 Joules and 15 Joules, respectively, under the same conditions. This superior toughness minimizes the risk of damage during rotary percussive drilling (Friedr. Ischebeck GmbH, 2016). Additionally, the fine-grained steel exhibits excellent resistance to stress corrosion cracking, ensuring durability. Hollow tendons, such as the one used in this experiment, offer several advantages over solid tendons with equivalent cross-sectional areas. These include better structural performance in terms of buckling resistance, a larger bond area due to the increased circumference, and improved flexural stability. These benefits are achieved without increasing the amount of steel (material cost) while maintaining the same tensile and compressive capacity (Friedr. Ischebeck GmbH, 2016). For this experiment, hollow bars with dimensions of 103/78 mm (103 mm outer diameter and 78 mm inner diameter) were selected. These bars were supplied in 3-meter lengths, and five bars were joined together using couplers during installation to achieve a total length of 15 m. Of this length, 14.5 m were embedded in the ground, with 0.5 meters extending above the surface.

Figure 3.3: *TITAN hollow bars*

3.3.2. Grout

The grout used in the experiment served both as a flushing medium during drilling and as a component of the pile structural body. Two types of grout mixtures were utilized: a cement suspension with a water-to-cement ratio of 0.7, employed during the initial drilling phase, and a stiffer grout with a water-to-cement ratio of 0.4–0.5, used for the final grouting. The stiffer mix had a minimum compressive strength of $f_{ck} \geq 35N/mm^2$, ensuring high durability and load-bearing capacity.

3.3.3. Sensors

Several sensors were used in the experiment: Strain gauges, temperature sensors, piezometers, LVDT, load cells. The strain gauges, piezometers, ground temperature sensors, and load cells were calibrated by the company SISGEO. The calibration report and acceptance report are presented in annex A.

3.3.3.1. Strain gauges

In this experiment, SISGEO's embedment strain gauges, model 0VK4200VC00, were used to monitor strain within the micropiles (Figure 3.4). These vibrating wire strain gauges are specifically designed for embedding in concrete structures, making them ideal for assessing strain in elements such as piles, foundations, and tunnel linings.

The 0VK4200VC00 model features an active gauge length of 165 mm and a measurement range of ±1500 microstrains, with a typical frequency range between 500 and 1015 Hz. It includes a built-in thermistor for temperature compensation, ensuring accurate strain measurements under varying thermal conditions (Sisgeo, 2025b). Constructed from stainless steel, the gauge is robust and suitable for demanding environments. Its IP68 rating allows for submersion up to 2.0 MPa, accommodating high-pressure conditions encountered during micropile installation.

Figure 3.4*: Strain gauge.*

3.3.3.2. Temperature sensors

3.3.3.2.1. Micropile temperature sensor

The Correge PT100 RTD temperature probe (RS 370-6571) from RS shop was used to monitor the pile temperature. This Class A platinum resistance thermometer (PT100) from Correge (RS stock number 370-6571) uses a 100 Ω platinum element in a four-wire configuration, compliant with IEC 751. The sensing element is enclosed in a 3 mm diameter, 30 mm long 316L stainless steel sheath, which ensures corrosion resistance and mechanical protection. The sensor is constructed in a four-wire configuration, improving accuracy by minimizing the influence of lead wire resistance (RS online, 2025a). The temperature measurement range extends from –50 °C to +250 °C, making it suitable for moderate-to-high temperature monitoring. The cable insulation is made from PTFE and includes a 2 m long cable, which was later extended to a length of 30 m. With an IP68 rating, the sensor withstands prolonged submersion and harsh environmental conditions, making it appropriate for embedded installation in micropiles where exposure to moisture and pressure is expected.

Figure 3.5*: Micropile temperature sensor.*

3.3.3.2.2. Ground temperature sensor

The SISGEO temperature string model 0TS00RTD000 equipped with eight measuring points offers the possibility of monitoring the ground temperature at various depths around the micropiles. This temperature string is composed of RTD sensors (100Ω PT-100), conforming to Class A EN60751 standards, ensuring high-accuracy temperature measurements over a broad range. Each sensor has a measurement range of -200°C to +400°C, with an accuracy of ±0.2°C at 0°C and a resolution of 0.1°C (Sisgeo, 2025a).

The temperature string has a sensed section length of 180 mm and a diameter of 28 mm, with the sensors mounted on a durable PVC cable. The temperature string operates within a temperature range of -30°C to +80°C with the standard cable, and it is rated IP68, providing protection against dust and water submersion up to 2.0 MPa, making it ideal for outdoor installations and harsh environmental conditions. The string's use of multiple measuring points allows for a detailed and continuous thermal profile of the surrounding soil, providing essential data for evaluating the thermal behavior of the energy micropiles in this study.

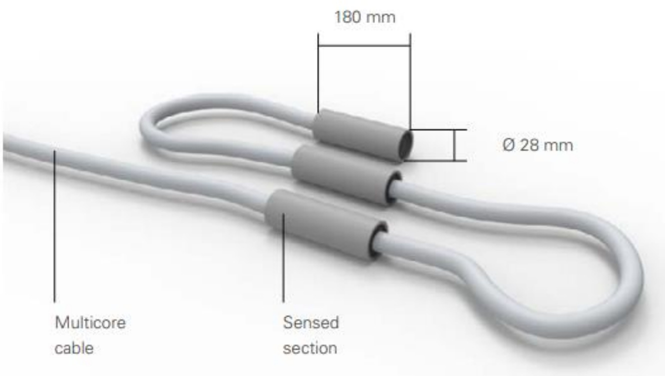

Figure 3.6: *Ground temperature sensor.*

3.3.3.2.3. Fluid temperature sensors

The RS PRO RTD temperature sensor (stock number 200-0593) was used to monitor the fluid inlet and outlet temperature. This sensor is a Class A, 3-wire, platinum resistance thermometer (PT100) with a nominal resistance of 100 Ω at 0 °C, complying with IEC 60751 standards for high-accuracy measurements (RS online, 2025b). It includes a 50 mm long probe with a 6 mm diameter, constructed from 316 stainless steel, offering corrosion resistance and mechanical durability in subsurface conditions. It is rated for a temperature range from –50 °C to +250 °C, making it suitable for applications involving moderate to high thermal exposure. The cable 1 m long, was later extended to a length of 10 m.

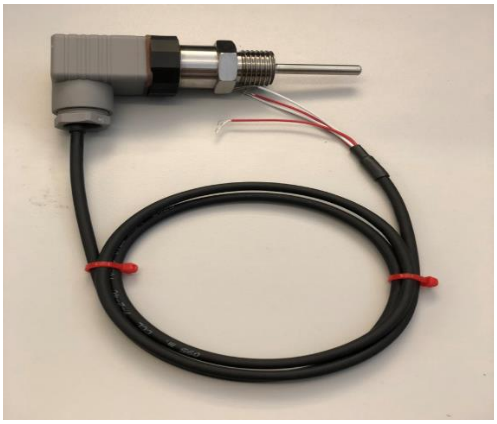

Figure 3.7: *Fluid temperature sensor.*

3.3.4. Plastic pipes

For this study, two types of plastic pipes have been selected: the Powerwave corrugated coaxial pipe by Jansen and the split pipe by separatus.

3.3.4.1. Corrugated coaxial pipes

The Jansen Powerwave coaxial pipe consists of two concentric components: a smooth inner pipe and a corrugated outer pipe. Manufactured from PE 100 RC, the system operates within a temperature range of –20 °C to +40 °C and has a pressure rating of PN 7.4. The outer pipe has an external diameter of 63 mm and a wall thickness of 2.9 mm, while the inner pipe measures 37 mm in diameter and is 3.5 mm thick (Jansen, 2025). The corrugated design of the outer pipe increases the external surface area to 0.22 m²/m, thereby enhancing heat exchange with the surrounding soil. Additionally, the inner corrugation further improves heat transfer by inducing turbulence within the circulating fluid, even at low flow rates. The system offers a relatively high fluid volume of approximately 1.9 L/m, which can aid in buffering thermal energy and maintaining more stable thermal conditions during periods without active circulation. The large diameter also contributes to reduced hydraulic resistance, potentially lowering the energy demand on the circulating pump.

Figure 3.8*: Jansen coaxial pile (from Jansen, 2025).*

3.3.4.2. Split pipe

The Separatus split pipe system represents a newer design in coaxial geothermal piping. It has a more compact external diameter of 51 mm and is also made from high-quality PE 100 RC material, rated for PN10 pressure class. Internally, the pipe is divided by a 2.7 mm thick partition wall extending approximately 3 cm from the bottom, forming two separate flow channels. The wall thickness of the pipe is 3.1 mm (Separatus AG, 2025b). The system is optimized for efficient fluid flow, achieving a Reynolds number of 2300 at a flow rate of 160 L/min with water, which promotes effective thermal transfer while maintaining low hydraulic resistance. The pipe contains approximately 1.4 L/m of fluid and is suitable for operating temperatures between –20 °C and +40 °C (Separatus AG, 2025a).

Figure 3.9*: Separatus split pipe (from Separatus AG, 2025b).*

3.3.5. Exchange fluid

The exchange fluid flows through the plastic pipes transferring heat from the ground to the pump. The fluid used in the system was Kilfrost Geo, a non-toxic heat transfer fluid designed specifically for closed-loop ground and water source heat pump systems. It is engineered to reduce pressure losses within the circuit, thereby lowering energy requirements and improving overall system efficiency (Kilfrost, 2025). Compared to conventional fluids such as monoethylene glycol (MEG) and monopropylene glycol (MPG), Kilfrost Geo offers lower viscosity and superior thermal performance. It also has an enhanced environmental and safety profile, being free from nitrates, nitrites, borates, and heavy metals. The fluid performs reliably across a wide temperature range (−40°C to +40°C) and meets ASTM D1384-05 corrosion resistance standards (Kilfrost, 2025). The 50% and 39% Kilfrost Geo fluids were used during the experiment. The 50% Kilfrost Geo fluid has a density of 1204.7 kg/m^3, dynamic viscosity of 4.826 mPa·s, and heat capacity of 2827 KJ/kgK. The density, dynamic viscosity and specific heat capacity of the 39% kilfrost GEO mixture are 1157.6 kg/m^3, 3.062 mPa·s and 3129 J/kg·K respectively.

The properties of the pipes and the exchange fluid 50% Kilfrost Geo at 20 °C are given in Table 3.4.

Table 3.4*: Properties of the split pipe, the coaxial pipe and the exchange fluid*

Properties	Coaxial pipe	Split pipe	50 % Kilfrost Geo	39 % Kilfrost Geo
Thermal conductivity [W/ (m K)]	0.42	0.42	0.423	0.443
Specific heat capacity [J/ (kg K)]	1900	1900	2827	3129
Density [kg/m^3]	950	950	1204.7	1157.6
Filling volume [L/m]	1.9	1.4	N.A	N.A
Dynamic viscosity [mPa·s]	N.A	N.A	4.826	3.062

3.4. Micropile installation procedures

3.4.1. Conventional installation

As discussed in chapter 2, self-drilling micropiles combine drilling, grouting, and installation into a single process with the hollow bar serving simultaneously as the reinforcement, drilling rod, and injection rod. A drilling fluid suspension prevents the drilled hole from collapsing, eliminating the need for casing during installation. The drill bit fixed at the end of the hollow bar, is sacrificial and remains embedded in the ground. Self-drilling micropiles are more cost-effective and time-efficient than conventional cased micropiles. They are particularly suited to soft soil, as is the case in Trondheim test site. Furthermore, direct drilling and simultaneous flushing/grouting create a mechanical interlock between the grout body and the surrounding soil, enhancing shear strength, increasing load capacity, and reducing settlement (Friedr. Ischebeck GmbH, 2016). The installation of self-drilling TITAN micropiles is carried out in two primary steps: a rotatory percussive drilling with flushing medium followed by a dynamic grout injection.

3.4.1.1. Rotary percussive drilling with flushing medium

The first step involves rotary percussive drilling using a cement suspension as the flushing medium. This method removes soil cuttings, and results in soil displacement and compaction similarly to the installation of a displacement pile. The cement suspension, with a water-to-cement ratio of 0.7, is pumped into the drilled hole, stabilizing it and forming a filter cake that enhances the bond between the grout body and the soil (Friedr. Ischebeck GmbH, 2016). Drilling is performed at a rate of approximately 1 meter per minute. To ensure the quality of the grout body, the drilling rate may be reduced, and the borehole periodically cleaned. Cleaning involves extracting and reinserting the drilling rod while continuing to rotate and flush, effectively removing debris and rinsing the drilled hole clean. Because the micropiles were installed in very soft soil at the test site, the percussive impact was not used, and the rotation speed was slightly increased.

3.4.1.2. Dynamic pressure grouting

The second step involves injecting grout under dynamic pressure while simultaneously rotating the tendon. The grout suspension, with a water-to-cement ratio of 0.4 - 0.5 and a minimum strength of $f_{ck} \geq 35N/mm^2$, displaces the initial flushing medium, forcing it out of the borehole and stabilizing the drilled shaft. The stiff grout mix improves the side shear bond between the micropile and the surrounding soil. In certain cases, the first step can be performed using the grout suspension instead of the cement suspension. When this method is adopted, the second step becomes unnecessary (Friedr. Ischebeck GmbH, 2016).

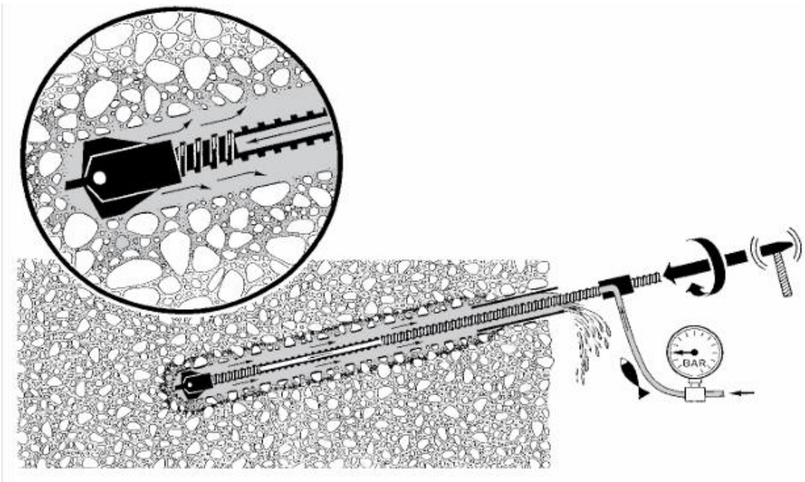

(a)

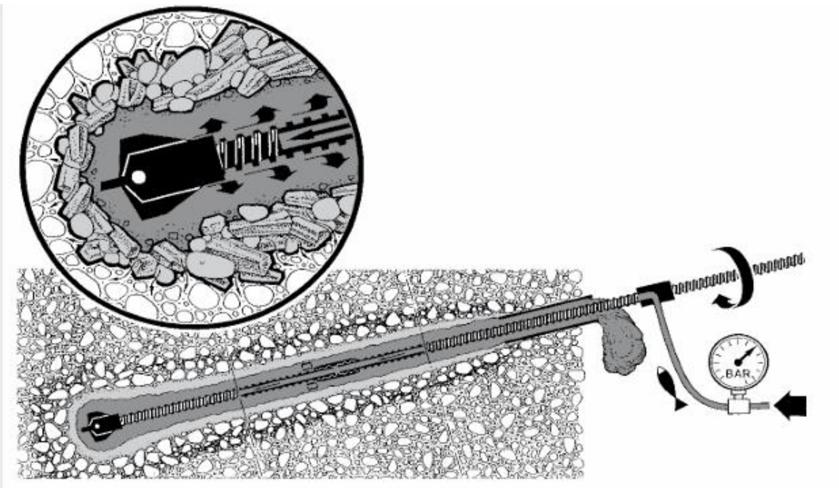

(b)

Figure 3.10*: Installation of micropiles. (a) Rotatory percussive drilling with a flushing medium; (b) Dynamic pressure grouting with grout suspension (Friedr. Ischebeck GmbH, 2016).*

3.4.2. Fixing of sensors

In typical installations, sensors are directly fixed to the rebars of piles or hollow bars of micropiles. This approach works well for drilled piles with casings or driven precast piles. However, it is not feasible for self-drilling micropiles because the hollow bar serves also as the drilling rod and undergoes rotary drilling during installation, a process that could damage the sensors. Consequently, the installation procedure for instrumented self-drilling micropiles had to be revised.

Initially, the plan was to attach the sensors to 16 mm diameter rebars and insert them after grouting. Figure 3.11 shows the sensors being fixed to the rebars. However, during insertion, the flexibility of the rebars caused them to bend into the surrounding soil, preventing their full placement to the bottom of the micropile. Only a partial depth of about 6 meters could be achieved. As a result, the first micropile was installed without any strain or temperature sensors.

(a)

(b)

(c)

(d)

Figure 3.11*: Fixing sensors on rebars: (a) strain gauges on rebar; (b) temperature sensors on rebar; (c) strain gauges and temperature sensors wiring; (d) insertion of rebar into the grouted micropile.*

Given the challenges associated with the insertion of rebars into the grout, an alternative method was employed. After drilling the hole and inserting the hollow bars to the required depth, the bars were fully removed. The rebars, with sensors attached, were then fastened to the hollow bars using plastic ties. However, this method was also unsuccessful as the rebar and hollow bars could not be lowered simultaneously. The plastic ties failed to provide sufficient contact or grip, which led to misalignment. Welding the rebars to the hollow bars was considered a more robust solution, but this approach was deemed too time-consuming.

It was ultimately decided to attach the sensors directly to the hollow bars rather than to the rebars. Initially, attaching sensors to the hollow bar during rotary drilling was deemed impractical due to the risk of damage. However, this risk was mitigated once the drilling process was completed, and the hole was prepared. The procedure involved completing the drilling, removing the hollow bar, affixing the sensors to it, and then lowering the bar back into the hole while performing rotary drilling and grouting. Figure 3.12 shows the sensors being attached to the hollow bar.

(a)

(b)

Figure 3.12*: Fixing of sensors on the hollow bar. (a) strain gauge on hollow bar; (b) temperature sensor on hollow bar.*

Using this method, the second micropile was successfully installed and instrumented with two strain sensors (S3 and S6). The remaining four micropiles were also installed using this approach and instrumented with four strain sensors (S3, S4, S5, and S6) and two temperature sensors (T1 and T2). Figure 3.13 illustrates the placement of each sensor on the hollow bar. For simplicity, a hollow bar of 15 m has been assumed in the illustration, rather than 5 hollow bars joined together with couplers. The micropiles were designed as friction micropiles and the length was chosen to ensure that they remained fully embedded in soft soil, without reaching the underlying bedrock.

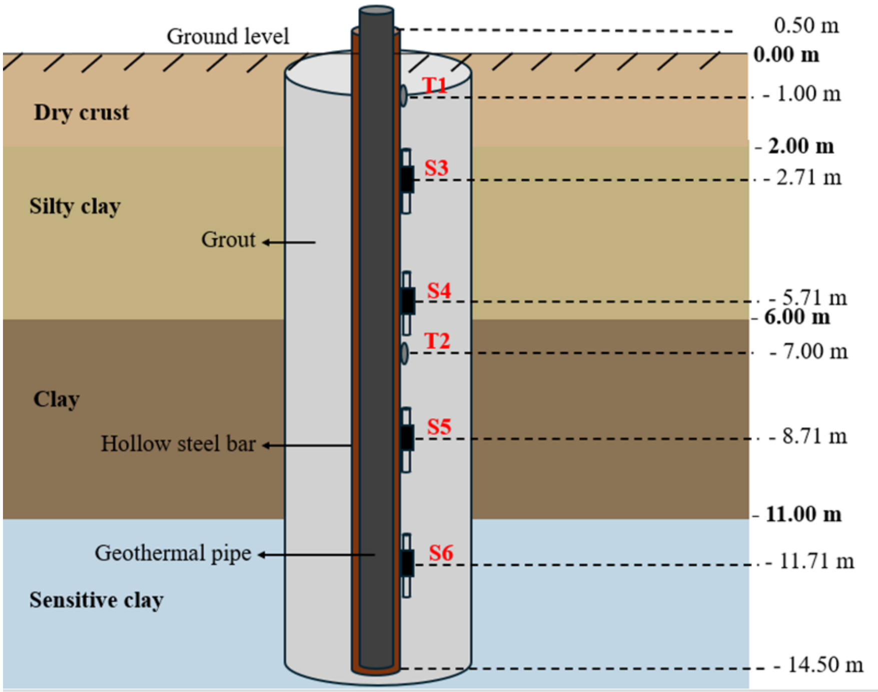

Figure 3.13*: Schematic diagram of the position of sensors on the hollow bars of the micropile.*

3.4.3. Installation of plastic pipes

As already mentioned in section 3.3.4, two types of plastic pipes were utilized for the experiment: split pipe and corrugated coaxial pipe. Following the installation of the instrumented micropiles, these pipes were inserted into the hollow bars. The hollow bars had an internal diameter of 78 mm and were filled with secondary grout. The outer diameters of the split pipe and the corrugated coaxial pipe were 51 mm and 63 mm, respectively, leaving minimal clearance between the pipes and the walls of the grout-filled hollow bars as seen in Figure 3.14. This limited space made the pipe insertion process challenging.

Figure 3.14*: Coaxial pipe in hollow bar.*

To facilitate the insertion, water was introduced into the hollow bars to reduce the density and viscosity of the grout, rendering it more fluid. This adjustment enabled the successful installation of the split pipes. However, the larger corrugated coaxial pipes still could not be inserted using this method alone. To overcome this difficulty, a 10 kg load was attached to the end of the coaxial pipe as shown in Figure 3.15. The load had dimensions of 0.5 m in height and 60 mm in diameter. The added weight helped to push the pipe through the dense grout, ensuring its successful installation.

Figure 3.15*:10 kg load fixed to the bottom end of the coaxial pipe to ease pipe lowering in the hollow bar.*

Micropile installation began on October 28, 2024 and was completed by October 31, 2024. Of the 6 micropiles, split pipes were installed in 4 (micropile 1, micropile 2, micropile 3, and micropile 6) while corrugated coaxial pipes were installed in the remaining 2 (micropile 4 and micropile 5). The 6 micropiles installed on site are shown in Figure 3.16.

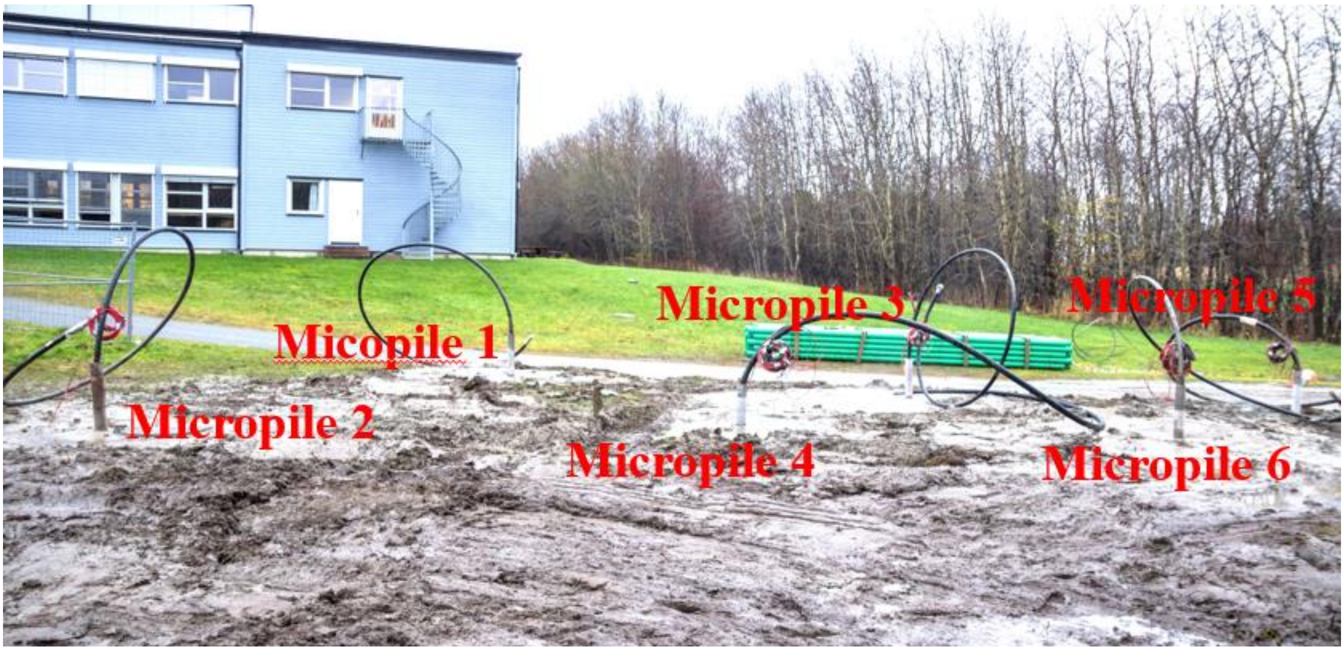

Figure 3.16*: Installed micropiles on site (October 31, 2024).*

Table 3.5 gives a summary of the drill bit diameters, the types of sensors and plastic pipes used in the micropiles

Table 3.5*: Drill bit diameters, types of sensors and plastic pipes used in the micropiles*

	Drill bit diameter [mm]	**Micropile diameter [mm]**	**Sensors**	**Plastic pipe**
Micropile 1	280	300	None	Split pipe
Micropile 2	280	300	S3 and S6	Split pipe
Micropile 3	280	300	T1, S3, S4, T2, S5, and S6	Split pipe
Micropile 4	280	300	T1, S3, S4, T2, S5, and S6	Coaxial pipe
Micropile 5	280	300	T1, S3, S4, T2, S5, and S6	Coaxial pipe
Micropile 6	220	240	T1, S3, S4, T2, S5, and S6	Split pipe

3.4. Installation of piezometers and temperature sensors in the ground

At the time of submission of this thesis, piezometers and ground temperature sensors were not installed due to lack of appropriate machines, and available personnel. These sensors will be installed later. Nevertheless, the initial ground temperature was gotten from the micropile temperature readings several months after installation and before the start of the thermal test.

3.5. Data acquisition

Data from the strain and temperature sensors were collected using the OMNIALOG GT-2400 datalogger by SISGEO. The standard datalogger includes 24 input channels, which were expanded to 72 by adding three external multiplexers to accommodate the large number of sensors installed on the micropiles. The datalogger supports various input types including mA, mV, V, mV/V, °C, and Hz (μsec, digit). Strain values were recorded in digit format and later converted to microstrain using a linear factor provided by the manufacturer. The logger operated within its specified temperature range of -30 °C to +70 °C and was enclosed in a steel box for protection on site. The fluid temperature sensors, flow rate meter, and energy meter were connected to another data acquisition system of a neighboring project.

Figure 3.17: *Sensors connected to the Omnialog datalogger.*

3.6. Test setup

Testing began on 3 June 2025, approximately seven months after the installation of the piles. This extended period allowed the surrounding soil to regain some of its strength and stiffness. Testing at an earlier stage was not possible due to several factors. These included extremely cold weather conditions, snow- and ice-covered ground (Figure 3.18), and limited daylight hours during the winter months in Trondheim (approximately 4 to 6 hours per day). Additional delays were caused by the unavailability of qualified technicians for the setup, as well as the relative novelty and uncommon nature of the components involved, such as the pipes and heat pump system.

Figure 3.18: *Test site in winter (November 2024), snow covered and icy.*

The site layout is shown in Figure 3.19. All above-ground piping was thermally insulated to minimize temperature losses to the environment. Each pipe was connected to a junction cabinet, where it was divided into two flow channels: the inlet (fluid entering the micropile) and the outlet (fluid exiting the micropile), resulting in 6 inlet channels and 6 outlet channels. Flow in each channel was controlled by a valve. To start a thermal test on a specific micropile, the corresponding valve on the junction cabinet was opened. The six inlet channels were combined into a single main inlet line, and similarly, the outlet channels were merged into a single outlet line. These were then connected to a 2.3 kW exhaust air source heat pump, forming a closed-loop circulation system. To ensure safety and restrict unauthorized access, the entire test area was enclosed with a fence. All components, including the micropiles, manifold, piping system, sensors on pile and datalogger, were installed within this secured perimeter. Warning signs were posted on the fence to indicate that the area was an active test site.

(a)


ANLEGGS OMRÅDE
Uvedkommende ingen adgang
Bruk verneutstyr
armacell ArmaFlex

(b)

(c)

Figure 3.19: *Test site. (a) Pipes connected to the manifold. (b,c) Micropiles in the fence*

Initially, micropile cooling was planned, using an inlet fluid temperature lower than the ground temperature. However, the minimum fluid temperature allowed by the air-to water exhaust heat pump in cooling mode was 8°C, which was higher than the initial average temperature of the micropile and surrounding ground (approximately 6°C). As a result, micropile cooling was not possible, and the test was conducted in heating mode instead. The thermal tests were carried out by injecting heat into the micropiles to simulate building cooling applications. Heat exchange with the surrounding environment was possible through openings made in the technical cabin.

Figure 3.20: *Openings made in the technical cabin to exchange heat with the surrounding air.*

Linear Variable Differential Transformers (LVDTs) initially planned to monitor micropile vertical displacements, could not be used at the time of testing and were replaced by mechanical dial gauges. Inlet and outlet fluid temperatures were measured by resistance temperature detectors (RTDs) installed close to the heat pump. Flow meters and electrical current meters were installed to record the flow rate of the circulating fluid and the electrical energy consumption of the system during the tests. An average flow rate of 7.2 l/min was recorded.

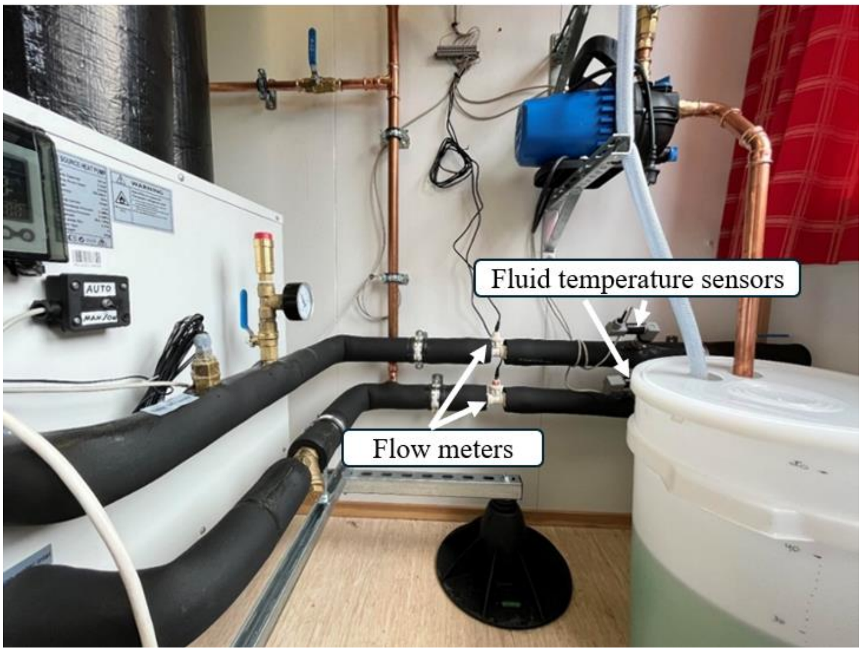

Figure 3.21*: Heat pump and sensors connected to the pump.*

3.7. Testing program

The testing program on the micropiles included pull-out load tests on two micropiles (micropiles 1 and 5), a creep test on micropile 5, thermo-mechanical test on micropile 5, and two thermal tests on micropiles 3 and 6. Micropile 2 was also tested under thermal loading as a preliminary trial; however, since the test lasted less than 24 hours, it will not be discussed further.

The load tests were conducted to determine the load-bearing capacity of the micropiles. Although the thermal tests were limited to durations of less than seven days due to time constraints, they were carried out until the micropile temperature had stabilized, ensuring reliable results for analysis. As already mentioned in section 3.4.2, all micropiles were instrumented with temperature sensors (T1 and T2) and strain gauges (S3, S4, S5, and S6) at different depths, except for micropile 2, which was equipped with only two strain gauges (S3 and S6) and micropile 1 to which no sensor was fixed. During the tests, inlet and outlet fluid temperatures, micropile temperatures, and strain readings were continuously recorded. Micropile head displacements were manually measured throughout the test on micropile 5. The following sections present a detailed description of each test, in chronological order.

3.7.1. Test on micropile 1

The first pull-out test was carried out on micropile 1 (Figure 3.22), selected as the reference micropile. Prior to testing, the area around the micropile had to be prepared to allow sufficient space for the testing equipment. Specifically, the excess hardened grout from the installation process was removed. This grout, which extended 10 - 20 cm above ground level, limited the available clearance required to install the hydraulic jack and steel support beams for the pull-out test. Once it was carefully broken down, the setup was assembled. The test configuration consisted of the following components:

Hydraulic Jacks: Two hydraulic jacks (each 32 cm high and 25 cm diameter) were placed on either side of the micropile. This setup was selected due to the presence of the plastic pipe in the micropile, which prevented mounting a single central jack.

Steel Beams: Two steel I-beams (each 16 cm × 16 cm) were installed above the jacks. These beams were welded to steel plates.

Dial Gauge: A mechanical dial gauge was used to measure vertical displacements during the test. The initial attempt to monitor displacement using a laser sensor was not successful due to its low accuracy (±1 mm), which made it impossible to detect small displacements. As a result, the test was restarted using dial gauge, which provided more accurate readings.

Pressure Control System: The applied tensile load was controlled by adjusting the pressure in the hydraulic jacks. Target pressure values corresponding to load levels had been pre-calculated before testing.

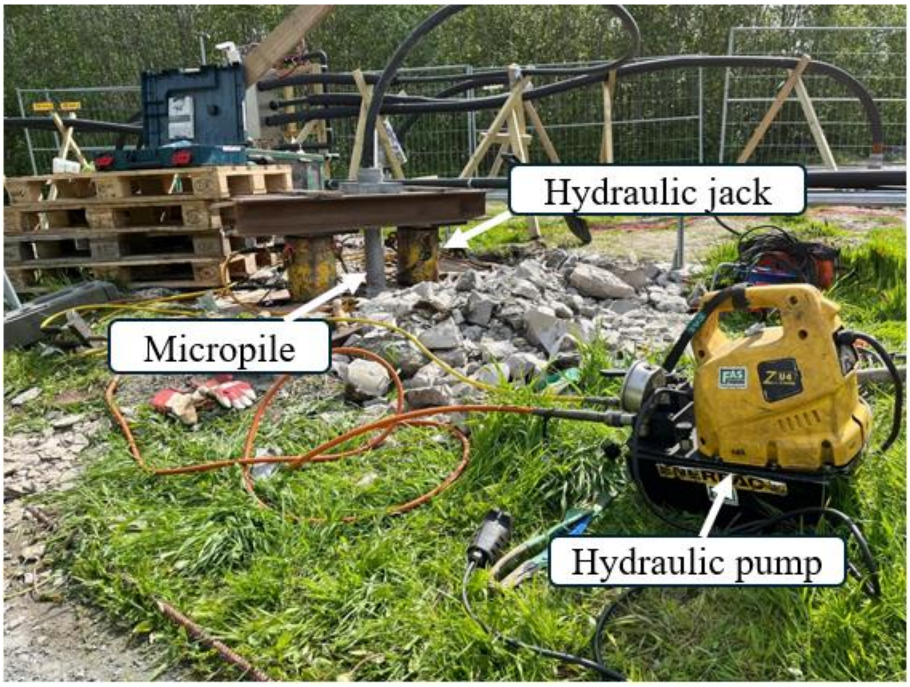

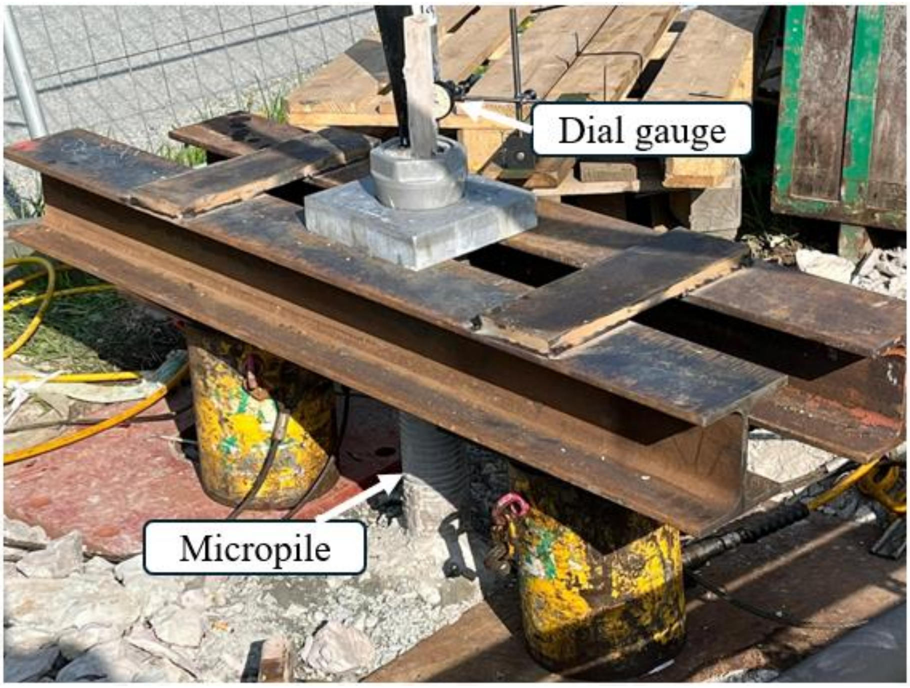

Figure 3.22*: Pull out load test on Micropile 1*

The test commenced at approximately 15:00 on 5 June 2025 and was completed at 19:30 on the same day. It was done in accordance with the Norwegian standard for micropile testing. The load was applied incrementally up to a maximum of 500 kN. Each load step was maintained for an average duration of 10 minutes. Keeping the load at 500 kN was challenging due to pressure drops observed in the system. This was probably caused by insufficient soil reaction from the surrounding ground (indicating a soft soil profile), or limited performance of the hydraulic pump. For this reason, the load on micropile 1 could not be increased above 500 kN and the test had to be ended.

To investigate short-term creep behavior, the final load of 400 kN was maintained overnight. However, by the following morning, the pressure had dropped from 75 bar (400 kN) to 55 bar (approximately 300 kN), indicating a reduction in load. The pressure was then increased back to 75 bar (400 kN), and the dial gauge recorded the new displacement values. It should be noted that the dial gauge did not have data logging capability, so continuous measurements could not be recorded throughout this creep test phase and will therefore not be discussed further. Micropile 1 was unloaded the next morning on June 06. Unloading was carried out in a single step due to the limitations of the pressure pump, which did not allow for a gradual, multi-step unloading process.

3.7.2. Test on micropile 5

A second pull-out load test was conducted on micropile 5 (Figure 3.23) from 15:00 to 17:00 on 6 June 2025. This micropile was instrumented with strain gauges. During the load test, the load was applied incrementally up to a maximum of 700 kN. Following this, the load was reduced to 550 kN and maintained for the duration of the test (approximately 7 days). The primary goal of the creep test was to compare micropile behavior during the creep test and thermo-mechanicaltest. Similar to the reference test, the system was unable to maintain a constant load of 550 kN throughout this period, with pressure drops occurring intermittently. When possible, the load was restored to 550 kN.

The initial plan was to perform a 24-hour long creep test, after which heating of the pile would begin at a controlled temperature of 25°C. A center-in coaxial configuration in which the exchange fluid entered the coaxial pipe through the center (inner) pipe and left through the annular space. The heat pump was switched on at 15:03 on 7 June 2025, and an inlet fluid temperature of 25 ± 2°C was set. However, the pump's compressor was working continuously, causing the fluid temperature to rise continuously. After two hours, the fluid temperature reached 37°C, even though the set temperature had been reduced to 15°C. To avoid unintended consequences due to overheating, the heat pump was shut down. As a result, only mechanical loading was continued till the 3rd day when heat pump was turned on. The pump was still not working properly as the temperature of the fluid continuously increased and stabilized to 43°C, which was approximately about 20°C above the set temperature. Moreover, the pressure in the pump had dropped from around 1.5 bar to around 0.2 bar, probably due to air bubbles in the system. Hence the system required technical intervention for proper thermal testing. On June 10, the pipes were all filled and thermal testing was restarted at an inlet fluid temperature of 25 ± 2°C. The pressure had increased to approximately 2 bars, however the compressor was still not working properly. Thermo-mechanical testing was then continued for 3 days (77 hours) during which both the mechanical load and the thermal load were maintained. Thermal heating on micropile 5 was then stopped but the mechanical load was maintained at 70 bar (375 kN) for a few hours before the micropile was finally unloaded.

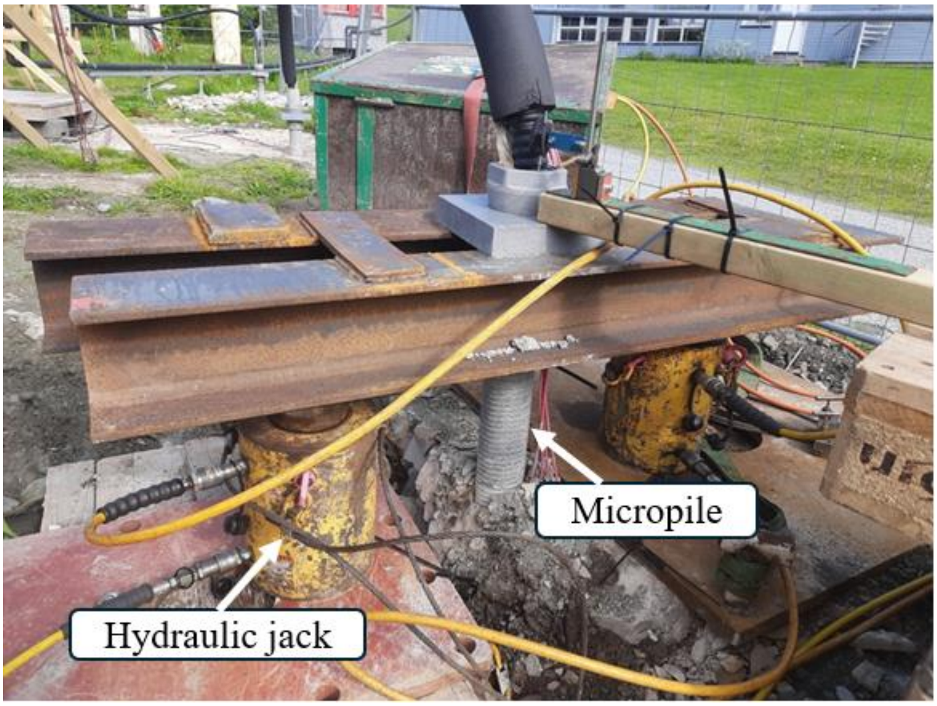

Figure 3.23*: Pull out load test, creep test and thermo-mechanical test set-up on micropile 5*

3.7.3. Tests on micropiles 6 and 3

Tests on micropiles 6 and 3 consisted of purely thermal tests in which the inlet temperature was set at 25 ± 2°C. As a reminder, micropiles 6 and 3 were all fitted with the split pipe. Micropile 6 had a smaller diameter (240 mm) compared to micropile 3 (300 mm).

The test on micropile 6 started on 13th June at 17:38. The test was interrupted on 16th June at 14:00 because the heat pump controller had to be replaced as the compressor was not working properly (continuously on). The test was restarted on 16th June at 14:10 and ended on 18th June at 10:00.

The test on micropile 3 began on 18th June and ended on 23rd June at 10:21.

A summary of the testing program is given in Table 3.6.

Table 3.6: *Testing programme*

	Activity	**Date and time**
Micropile 1	Load test started	06.06.2025 at 15:00
	Load test ended	06.06.2025 at 19:30
	Load test started	06.06.2025 at 15:00
	Load test ended	06.06.2025 at 17:00
Micropile 5	Creep testing at 550 kN	06.06.2025 at 17:00
	Heat pump switched on	07.06.2025 at 15:03
	Heat pump switched off	07.06.2025 at 17:00
	Heat pump switched on	09.06.2025 at 12:24
	Heat pump switched off	10.06.2025 at 11:00
	System maintenance (Filling of pipes)	10.06.2025 at 11:00
	Switching on heat pump	10.06.2025 at 12:00
	Switching off heat pump	13.06.2025 at 17:38
	Mechanical unloading	14.06.2025
Micropile 6	Switching on heat pump	13.06.2025 at 17:38
	Switching off heat pump	16.06.2025 at 14:00
	Change of heat pump controller	16.06.2025 at 14:00
	Switching on heat pump	16.06.2025 at 14:10
	Switching off heat pump	18.06.2025 at 10:00
Micropile 3	Switching on heat pump	18.06.2025 at 10:01
	Switching off heat pump	23.06.2025 at 10:21

3.8. Experimental test results

This section presents the results of the creep, thermal, and thermo-mechanical tests. The thermal tests involved heating the micropiles by circulating a heat exchange fluid through embedded plastic pipes at a temperature of approximately 25 ± 2 °C. The creep tests consisted of applying a constant tensile axial load of 550 kN to the micropiles. The thermo-mechanical test combined both thermal and mechanical loading conditions. During each test, key parameters were monitored, including fluid and micropile temperatures, micropile strains and head displacements, and energy consumption. In total, four micropiles were tested under these different loading scenarios. Unfortunately, ground temperature sensors and piezometers could not be installed during the testing period reported in this thesis. Hence, ground temperature and pore water pressure variations are not discussed. Nevertheless, the initial ground temperature was assumed to be equal to the initial pile temperature ranging between 5.9°C and 6.5°C from 2 m below the ground surface. Above this depth, the micropile temperature was variable and affected by the ambient temperature.

3.8.1. Micropile 1

Table 3.7 presents the load values and the corresponding head displacements (positive) on micropile 1, during the pull-out load test. The load could not be increased beyond 500 kN because the hydraulic pump pressure could not be sustained above this level. This was likely due to the observed ground sinking, indicating that the soil did not provide sufficient reaction force.

Table 3.7: *Pull- out load test on micropile 1*

Load [kN]	Pile head displacement [mm]
0	0
100	0
200	0.734
250	1.146
300	1.522
350	2.238
400	2.888
450	3.410
500	4.206
0	2.632

The load - displacement curve is plotted in Figure 3.24.

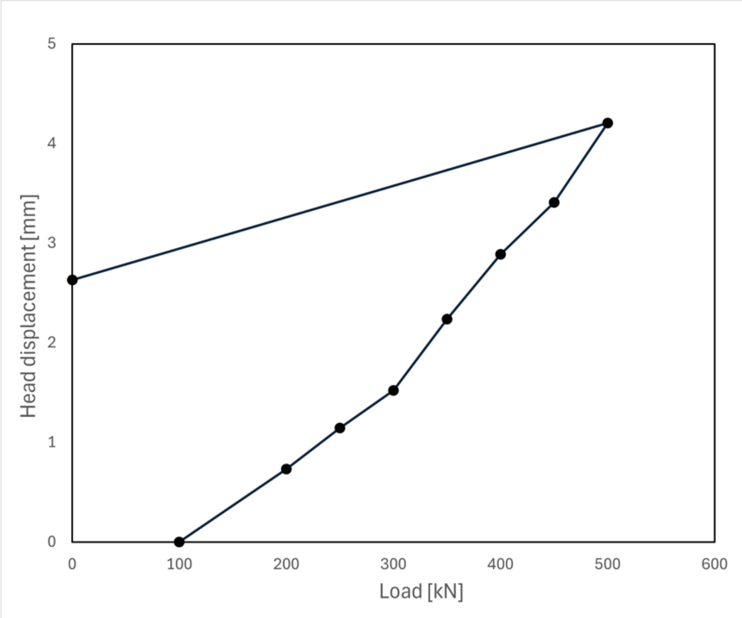

Figure 3.24 : *Pile head displacement vs load during load test on micropile 1*

No significant or disproportionate head displacement is observed in the load–displacement curve. To estimate the ultimate capacity of the pile, Chin's method for non-destructive static load testing was applied. This method involves plotting the ratio of displacement to load against displacement. The inverse of the slope of the resulting linear regression curve represents the ultimate load capacity (Chin, 1970; Yimsiri & Ratananikom, 2025). As shown in Figure 3.25, the linear fit of the data is given by the equation: y = 0.002x+0.0013. Accordingly, the ultimate load capacity Q_u is calculated as:

$$Q_u = \frac{1}{0.002} \approx 510 \text{ kN}$$

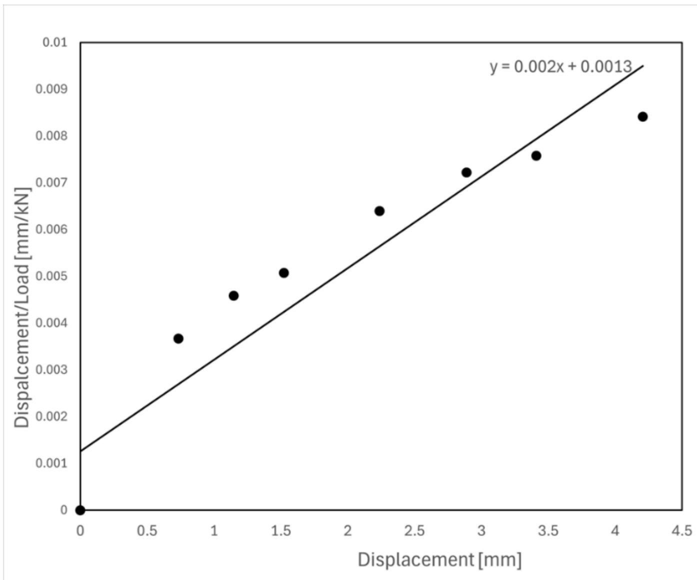

Figure 3.25: *Interpretation of load test on micropile 1 using Chin method.*

3.8.2. Micropile 5

The test results on micropile 5 could not be reported for the entire duration due to a problem with the data acquisition system, which failed to record continuous data. For clarity and ease of interpretation, the test results presented are divided into 5 test sections as shown in Table 3.8.

Table 3.8: *Tests on micropile 5*

Test number	Type of test	Start [h]	End [h]
Load test	Load test	0	2.133
M1	Mechanical test 1 also referred to as Creep test 1	2.5	16
M2	Mechanical test 2 also referred to as Creep test 2	16.13	22.8
TM1	Thermo-mechanical test 1	87.067	105.87
TM2	Thermo-mechanical test 2	106	134.53

Temperature corrections were applied to the strain gauge readings to account for the difference in thermal expansion between concrete and steel, using the following equation:

$$\text{Measured strains} = (S_i - S_0) + [(t_i - t_0) * (\alpha_S - \alpha_C)]$$

where S_i and S_0 are the strain readings at time t_i and t_0 respectively, α_S and α_C are the thermal expansion coefficients of steel (12.2 $*10^{-6}$ /°C) and concrete ($10*10^{-6}$ /°C) respectively. The strain values S_i and S_0 are expressed in microstrains [$\mu\varepsilon$], calculated as follows:

$$S_i = R_i * G$$

$$S_0 = R_0 * G$$

where R_i and R_0 are the raw strain readings (in digits), G=3.814 is the gauge factor provided in the sensor´s calibration report. The initial strain readings have been set to zero.

3.8.2.1. Load test

Table 3.9 presents the applied load values alongside the corresponding micropile head displacements which are plotted in Figure 3.26.

Table 3.9: *Pull- out load test on micropile 5*

Load [kN]	Pile head displacement [mm]
0	0
50	0
100	0
200	0
250	0
300	0.026
350	0.22
400	0.564
450	0.798
500	1.164
550	1.862
600	3.57
650	4.26
700	7.44

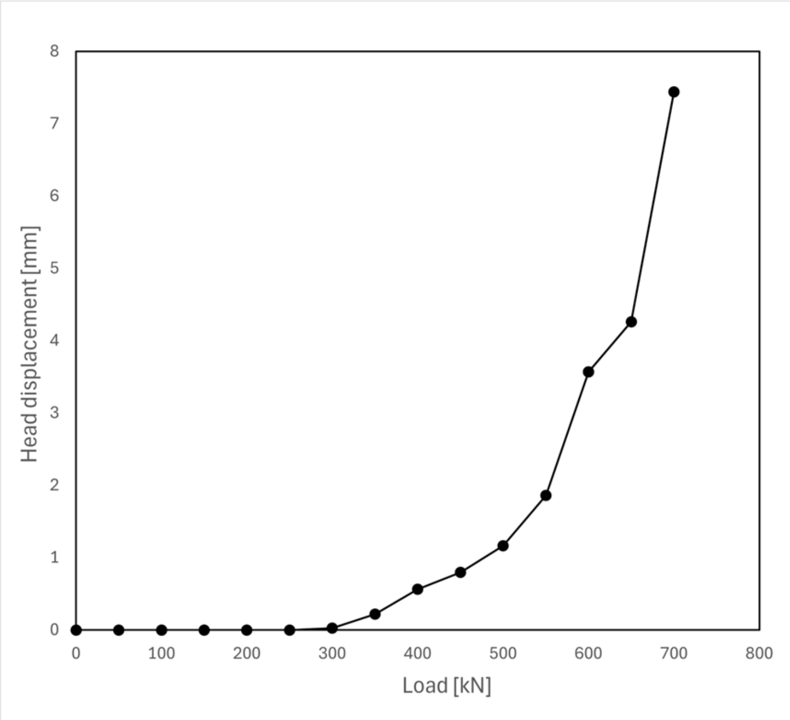

Figure 3.26: *Micropile head displacement vs load during load test on micropile 5.*

A disproportionate increase in micropile displacement is observed between 550 kN and 600 kN, and between 650 kN and 700 kN. However, a small displacement is observed between 600 kN and 650 kN. This may be an error as the dial gauge was reset at 600 kN. Applying Chin method, the linear fit of the data is represented by the equation: y = 0.0015x+0.0002 as shown in Figure 3.27, which suggests an ultimate load capacity Q_u calculated as:

$$Q_u = \frac{1}{0.0015} = 666.67\ kN$$

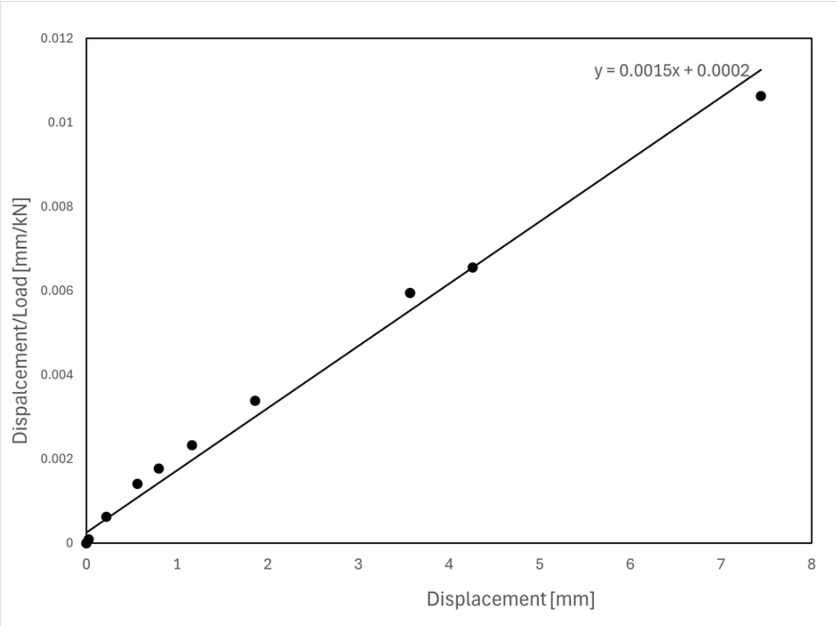

Figure 3.27: *Interpretation of load test on micropile 5 using Chin method.*

A second method was used to assess the ultimate capacity of micropile 5: Davisson´s method. According to this method, failure (that is the ultimate load) is defined as the point at which the measured pile head displacement exceeds the theoretical elastic elongation by a specified offset, calculated using the following expression (Coduto, 2001; Davisson, 1972):

$$\Delta = \frac{P \cdot L}{AE} + 4.0 + \frac{D}{120}$$

where: Δ is Davisson´s offset [mm], P is the load on the pile [kN], L is the pile length [mm], A is the cross-sectional area [mm^2], E is the Young´s modulus of pile material (MPa) and D is the pile diameter [mm].

The calculated Davisson offset for each load level is presented in Table 3.10. Based on the load–displacement curve, the point at which the measured displacement exceeds the Davisson offset corresponds to an ultimate load of 685 kN, as illustrated in Figure 3.28.

Table 3.10: *Calculating Davisson`s offset for estimating micropile capacity*

Load [kN]	Measured displacement [mm]	Davisson offset Δ [mm]
0	0	6.50
50	0	6.50035
100	0	6.50071
150	0	6.50106
200	0	6.50142
250	0	6.50177
300	0.026	6.50212
350	0.22	6.50248
400	0.564	6.50283
450	0.798	6.50318
500	1.164	6.50354
550	1.862	6.50389
600	3.57	6.50425
650	4.26	6.5046
700	7.44	6.50495

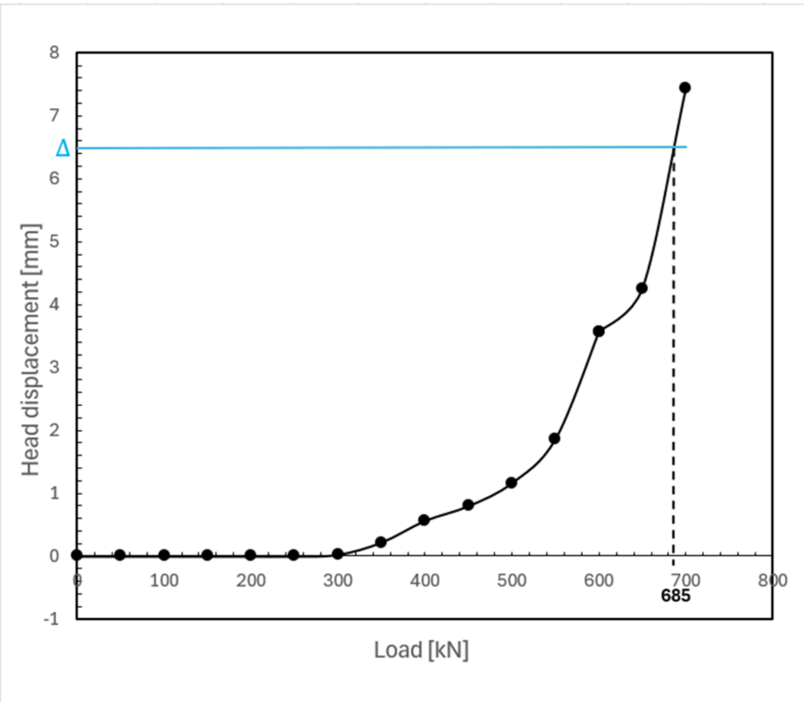

Figure 3.28: *Interpretation of load test on micropile 5 using Davisson´s method.*

As expected, the strains in the micropile increased with increasing pull-out load, indicating axial expansion. However, an unusual response was recorded at a depth of 2.7 m (sensor S3). While strain values followed the expected trend up to a load of 650 kN, a sudden drop in strain was observed beyond this point, as illustrated in Figure 3.29a. This anomaly may be attributed either to a malfunction of the sensor or the onset of cracking in the micropile at that location. As a result, strain data from sensor S3 has been excluded from subsequent analysis. Figure 3.29b presents the variation of strain with depth. As expected, the strain values decreased with increasing depth, with the highest strain recorded at 5.7 m (S4) and the lowest at 11.7 m (S6). This trend reflects the expected reduction in mechanical load with depth along the micropile.

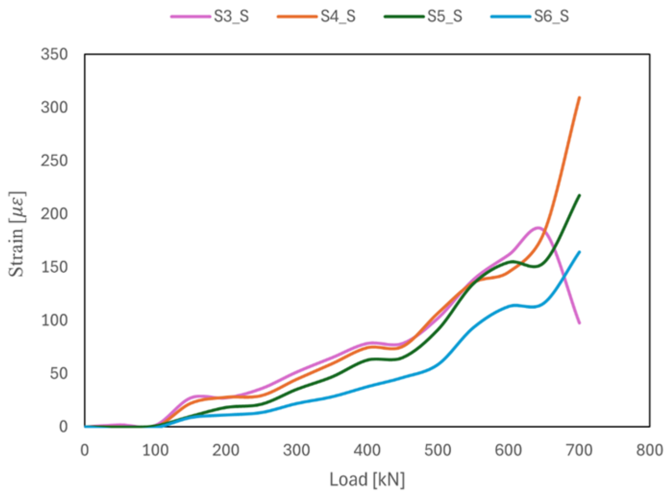

(a)

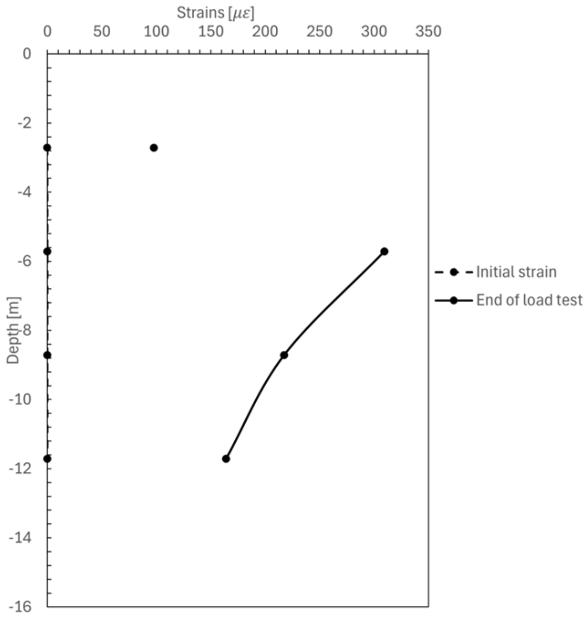

(b)

Figure 3.29: *Strains during load test on micropile 5. (a) strain vs time; (b) strain vs depth*

3.8.2.2. Creep test 1 (M1) and Creep test 2 (M2)

Creep test 1 was started just after the load test and was closely followed by creep test 2. The load was set at 550 kN at the beginning of the test, however a drop to 375 kN was noticed at the end of the test. The load was increased to 550 kN at t = 16 hr. This marked the start of creep test 2. Like in creep test 1, the mechanical load in creep test 2 dropped to a lower value during the test.

The measured strains during the creep tests represented the mechanical strains, as no thermal loading was applied. Strain evolution over time for sensors S3, S4, S5 and S6 installed at depths 2.71 m, 5.71 m, 8.71 m and 11.71 m respectively are presented in Figure 3.30a. A gradual decrease in strain values corresponding to the load reduction with time is observed. Additionally, "apparent residual" strains are observed as the strain values at the start of creep test 2 do not align with those recorded at the start of creep test 1 for the same load of 550 kN. This discrepancy is further illustrated in Figure 3.30b, where the strain values at 550 kN during creep test 1 also differ from those recorded at the same load level during the load test described previously. Specifically, the differences in strain between the load test and creep test 1 were +167.7 με, +79.1 με, and +75.6 με for sensors S4, S5, and S6, respectively and was smaller between creep tests 1 and 2.

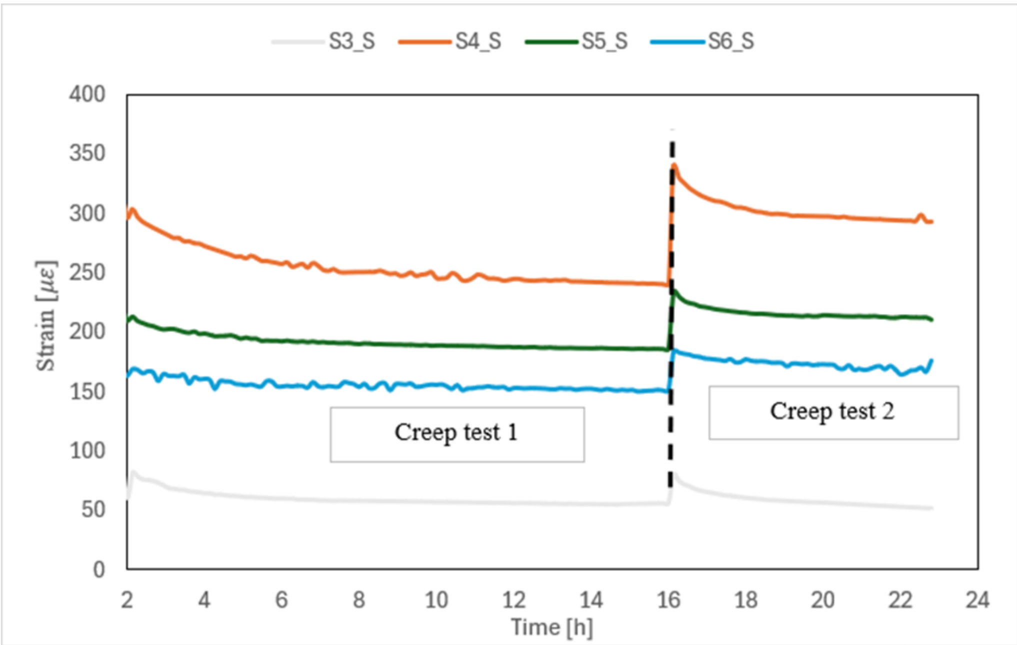

(a)

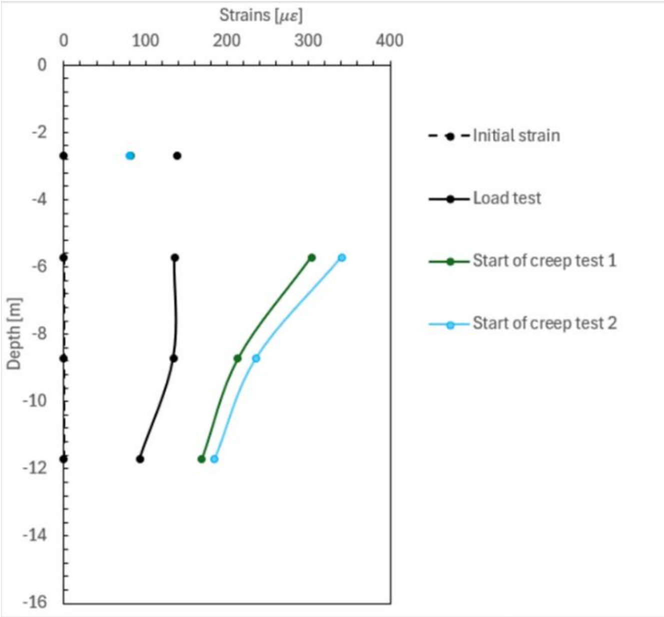

(b)

Figure 3.30: *Strains during creep tests on micropile 5. (a) Strain vs time during creep tests at depths 5.7 m (S4), 8.71 m (S5) and 11.71 m (S6); (b) Strain at a load value of 550 kN vs depth during load test and start of creep tests.*

The most significant strain reduction occurred at sensor S4, which is in the zone most affected by the mechanical loading. Strains at S6 were reducing at a slower rate as S6 is the deepest strain gauge which is least affected by the effects of mechanical loading. This behavior is illustrated in the strain–depth profile shown in Figure 3.31.

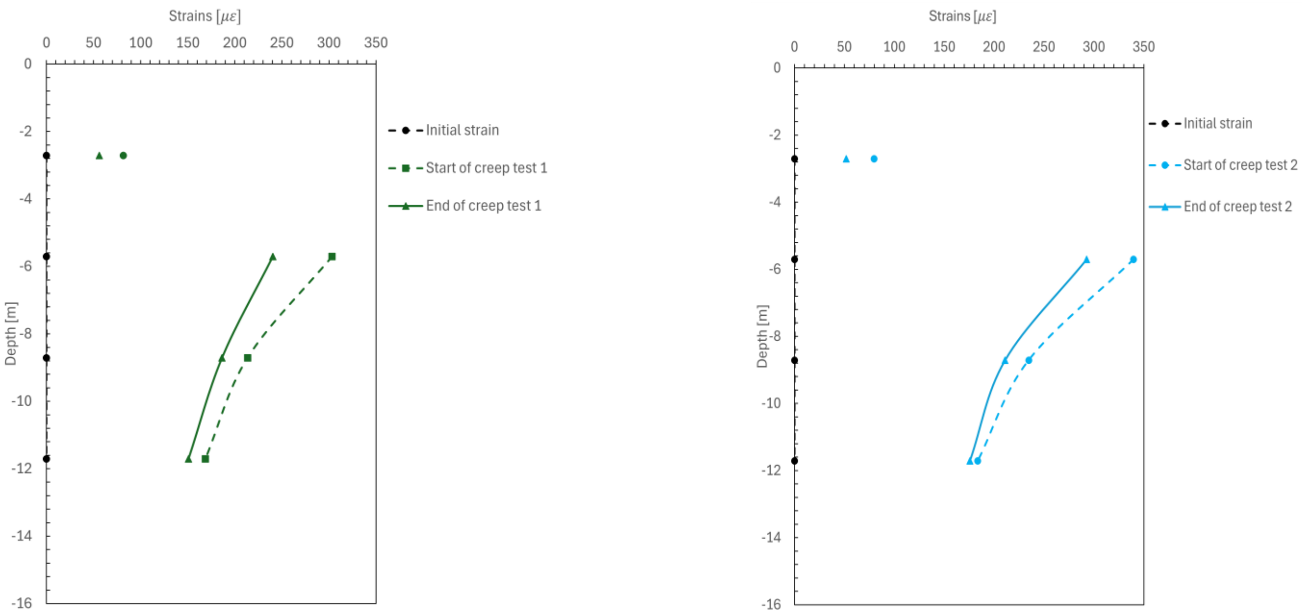

(a) (b)

Figure 3.31: *Strain vs depth during creep tests on micropile 5. (a) Creep test 1; (b) Creep test 2*

3.8.2.3. Thermo-mechanical test 1 (TM1) and thermo-mechanical test 2 (TM2)

Thermo-mechanical testing involved the simultaneous application of both thermal and mechanical loads to the micropile. The active length of the micropile was 14 m due to the space occupied by the solid weight (0.5 m long) at the bottom of the coaxial pipe.

3.8.2.3.1. Fluid temperature

The variation of inlet and outlet fluid temperatures over time is presented in Figure 3.32. It should be noted that no temperature data was recorded between t = 117.22 h and t = 128.6 h due to a system update in the data acquisition software.

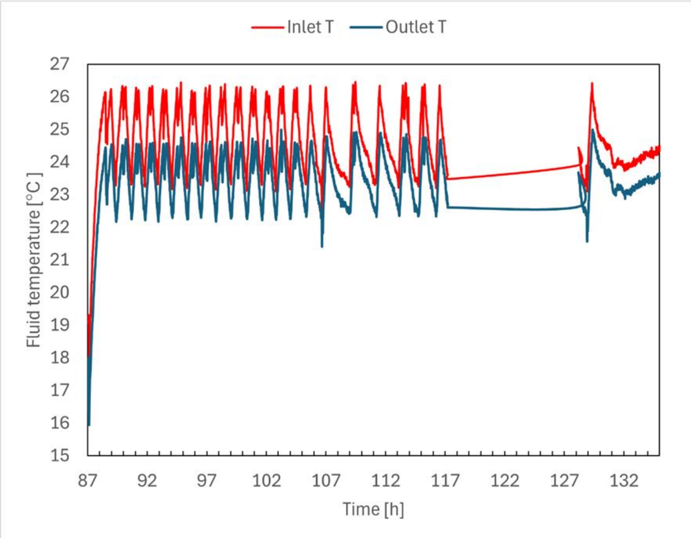

Figure 3.32: *Inlet and outlet fluid temperature during thermo-mechanical test on micropile 5.*

The average and maximum temperature difference between the inlet and outlet were approximately 1.11 °C and 2.143 °C respectively. Temperature changes few minutes after the heat pump was started have not been considered. Initially, the 50% Kilfrost Geo mixture, which has a density of 1204.7 kg/m³ and a specific heat capacity of 2827 J/kg·K was used. It was later replaced with a 39% kilfrost Geo mixture. The density and specific heat capacity of the 39% kilfrost Geo mixture are 1157.6 kg/m³ and 3129 J/kg·K respectively.

Based on an average volumetric flow rate of 0.00012 m³/s and an active micropile length of 14 m, the minimum, average and maximum thermal power transferred per meter of active pile length were calculated as follows:

$$Q_{av} = \frac{1157.6\,\mathrm{kg/m^3} * 3129\,\mathrm{J/kgK} * 0.00012\,\mathrm{m^3/s} * 1.11°\mathrm{C}}{14.0\,\mathrm{m}} = 34.46\,\mathrm{W/m}$$

$$Q_{max} = \frac{1157.6\,\mathrm{kg/m^3} * 3129\,\mathrm{J/kgK} * 0.00012\,\mathrm{m^3/s} * 2.143°\mathrm{C}}{14.0\,\mathrm{m}} = 66.53\,\mathrm{W/m}$$

These values are comparable with other geothermal heat exchangers (energy geostructures and energy boreholes).

3.8.2.3.2. Coefficient of performance, COP

The coefficient of performance (COP) is a key indicator of the efficiency of a thermal system, representing the ratio of thermal energy output to electrical energy input. It is defined as:

$$\mathrm{COP} = \frac{\text{Thermal energy obtained (Output)[kWh]}}{\text{Electrical energy consumed (Input)[kWh]}}$$

According to the energy meter, the total electrical energy consumed during the test was 23.017 kWh. The thermal energy output over a test duration of 47.47 hours is calculated as follows:

$$\text{Thermal energy output}_{\mathrm{av}} = 34.46 * 14.0 * 47.47 = 22{,}901.42\ \mathrm{Wh} = 22.90\ \mathrm{kWh}$$

$$\text{Thermal energy output}_{\mathrm{max}} = 66.53 * 14.0 * 47.47 = 44{,}217.36\ \mathrm{Wh} = 44.21\ \mathrm{kWh}$$

These values correspond to average and maximum COP values of approximately 0.99 and 1.92, respectively.

It is important to note that these COP values are significantly lower than typical values observed in air source heat systems (typically between 2 and 4). This discrepancy is attributed to a malfunction in the heat pump's compressor, which operated continuously during the test, significantly increasing electrical consumption. In a properly functioning system, the compressor operates only when the fluid temperature needs to be increased otherwise it remains off, while the circulation pump runs continuously. As a result, the COP values obtained in this test are not representative of the system's actual performance under normal operating conditions and should not be used for design or comparison purposes. These results highlight the importance of ensuring that all components of the system are functioning correctly prior to testing or operation. Faulty equipment can result in lower performance. Therefore, routine checks and proper commissioning of the system are essential for obtaining reliable data and ensuring optimal system performance.

3.8.2.3.3. Micropile temperature

The micropile temperature was measured using two temperature sensors (T1 and T2) and four strain sensors (S3, S4, S5 and S6) equipped with embedded thermistors at various depths as illustrated in Figure 3.13. Micropile temperature increased with time, as shown in Figure 3.33a.

A rapid increase in micropile temperature is observed during the initial hours of heating, with a rise of approximately 5 °C recorded by all sensors within the first three hours. This quick response can be attributed in part to the small dimensions of the micropile. Over time, the temperature stabilizes after 48 hours, to 8°C above the initial value. The plot of temperature versus depth is shown in Figure 3.33b. The highest temperature is observed at 1.0 m below the ground surface. This is because the micropile temperature at that depth is affected by the ambient temperature which varied between 17°C and 19°C during the day over the testing period. Nevertheless, the temperature increase is uniform along the depth of the pile.

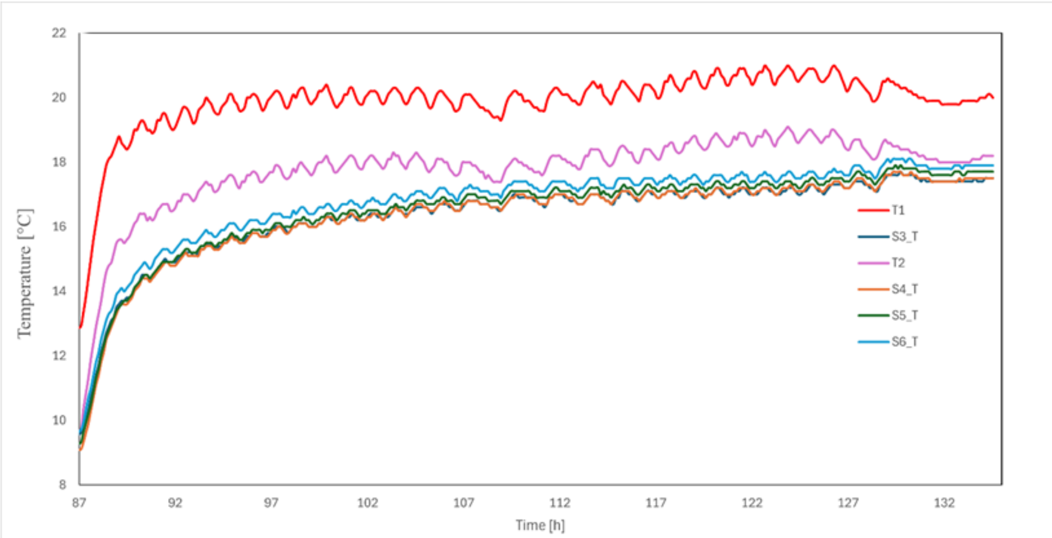

(a)

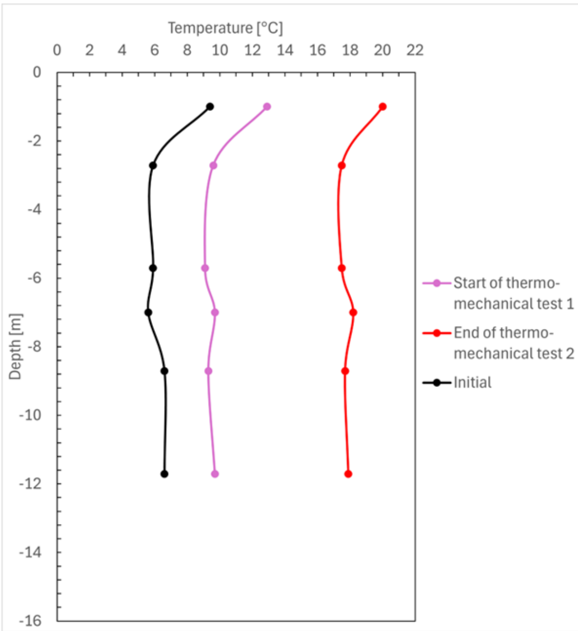

(b)

Figure 3.33: *Pile temperature during thermo-mechanical tests on micropile 5. (a) Pile temperature vs time at depths 1.0 m (T1), 2.71 m (S3),5.71 m (S4), 7.0 m (T2), 8.71 m (S5) and 11.71 m (S6); (b) Pile temperature vs depth.*

3.8.2.3.4. Strains

During the thermo-mechanical tests, temperature variations in the micropile induced thermal strains. Hence, the measured strains represent the combined effect of both mechanical and thermal loads. Thermal strains were obtained by subtracting the mechanical strains from the measured strains. The evolution of the measured strains and thermal strains over the duration of the test is shown in Figure 3.34. As previously mentioned, data from sensor S3 is excluded from the analysis due to suspected sensor malfunction or possible cracking of the micropile during the load test.

Thermal strains at S4 and S5 are observed to increase with temperature (Figure 3.34b), indicating thermal expansion. The observed behavior at S4 and S5 is consistent with theoretical expectations and aligns with patterns reported in previous experimental studies (Amatya et al., 2012; Bourne-Webb et al., 2013). The thermal expansion of the micropile counteracts the reduction in strain caused by the decreasing mechanical load. As a result, although the overall measured strains decline, the rate of this reduction is mitigated by the increasing thermal effect (Figure 3.34a).

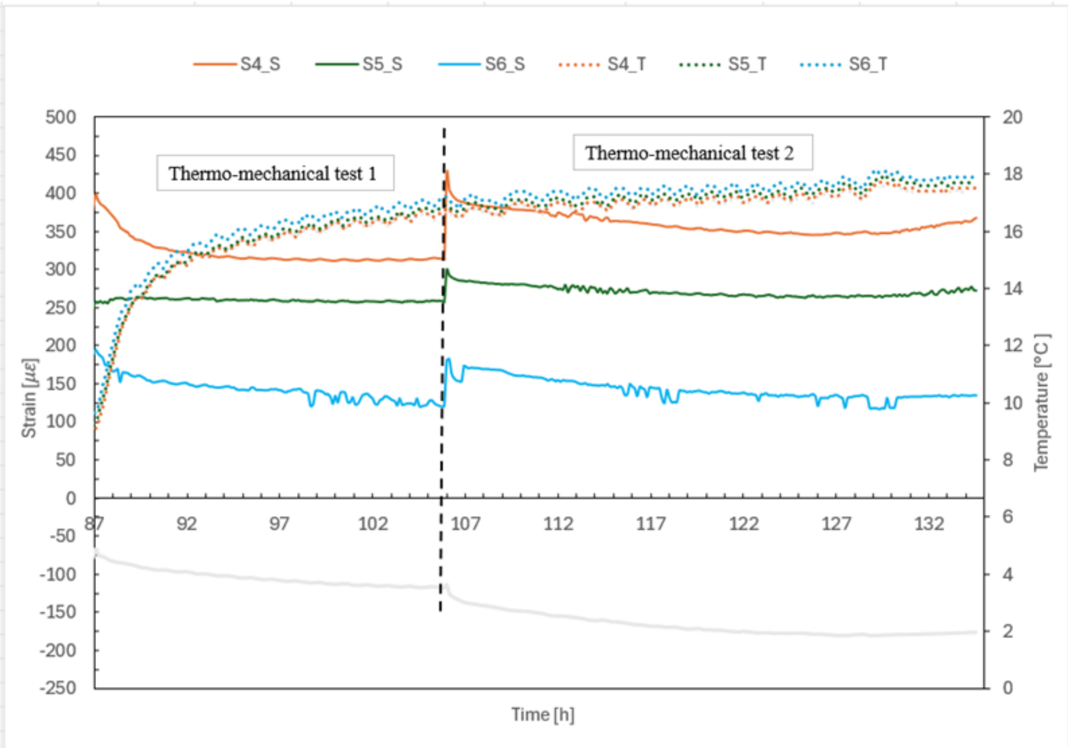

(a)

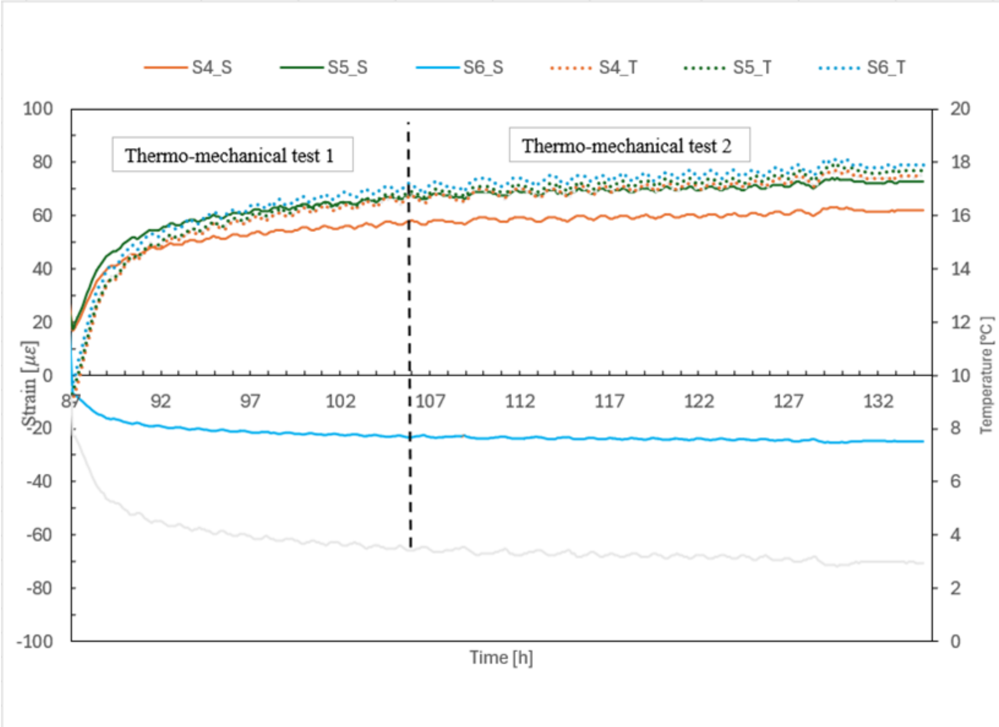

(b)

Figure 3.34*: Strains vs time during thermo-mechanical tests on micropile 5 at depths 5.71 m (S4), 8.71 m (S5) and 11.71 m (S6). (a) Measured strains; (b) Thermal strains.*

A particularly interesting observation arises at sensor S6. During the creep test, the reduction in strain at S6 was more gradual compared to S5 (Figure 3.30a). In contrast, during the thermo-mechanical test, the measured strains at S6 decreased more rapidly than at S5 (Figure 3.34a). As illustrated in Figure 3.34b, the thermal strains at S4 and S5 are positive (expansion) and increase with temperature. However, the thermal strains at S6 are negative, indicating contraction, which is contrary to the typical expansion behavior of piles when heated. According to the geotechnical investigation report, S6 is in a deeper soil layer characterized by the presence of sensitive clay, and possibly quick clay. Sensitive clays are known to lose significant strength upon disturbance or remolding, often behaving like a fluid. Quick clays, a highly sensitive subtype, are particularly prone to collapse and flow when disturbed. When saturated clays are heated, pore water pressure may increase, potentially reducing effective stress and soil strength and causing partial collapse, which can lead to a downward, or downdrag force on the pile. However, a maximum temperature change in the micropile was 11°C and is unlikely to significantly affect the surrounding soil. Further examination of the S6 sensor's behavior during the pre-testing laboratory phase (not reported in this thesis) revealed an anomalous temperature - strain relationship and high sensitivity to temperature changes. The strain values were approximately eight times higher than those of most sensors, which according to the manufacturer, should be an indication of sensor malfunction. These data were initialized to zero prior to analysis for consistency and were therefore not previously presented. It is therefore hypothesized that the unusual strain response at S6 is likely due to the sensor malfunction rather than an effect of downdrag force due to the thermal collapse of the surrounding soil. Nevertheless, given the complex behavior of clays - particularly sensitive clays – and previous observations of contractive behavior of energy piles during heating as reported by McCartney and Murphy (2017), further research is recommended to better understand the implications for the performance of energy geostructures in such soil conditions.

The variation of strains with depth is illustrated in Figure 3.35. The strains at 5.7 m depth are lower than those at 8.7 m depth, due to greater restraint provided by the stiffer surrounding soil. Larger thermal strains are observed during the thermo-mechanical test 1 as the micropile temperature increased by around 7.5°C during this test compared to thermo-mechanical test 2 where the temperature was almost stable with a maximum change of 1.2°C.

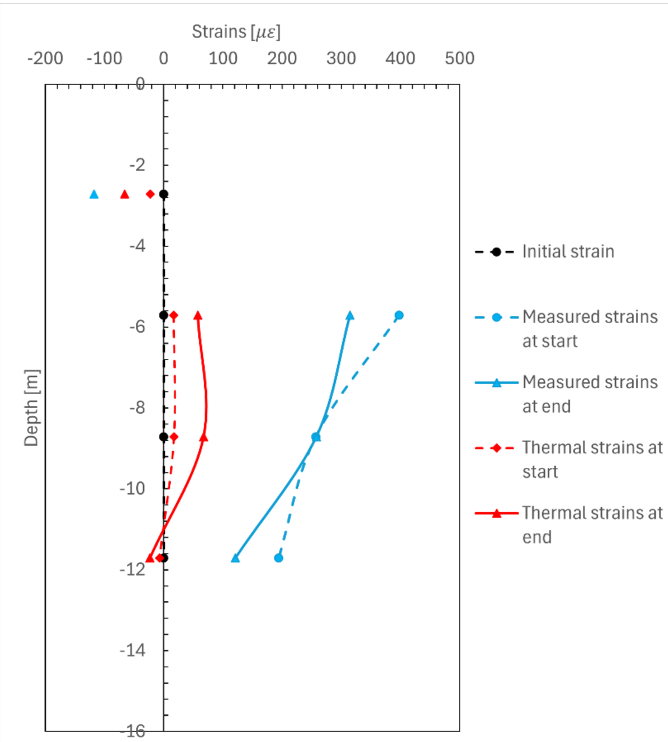

(a)

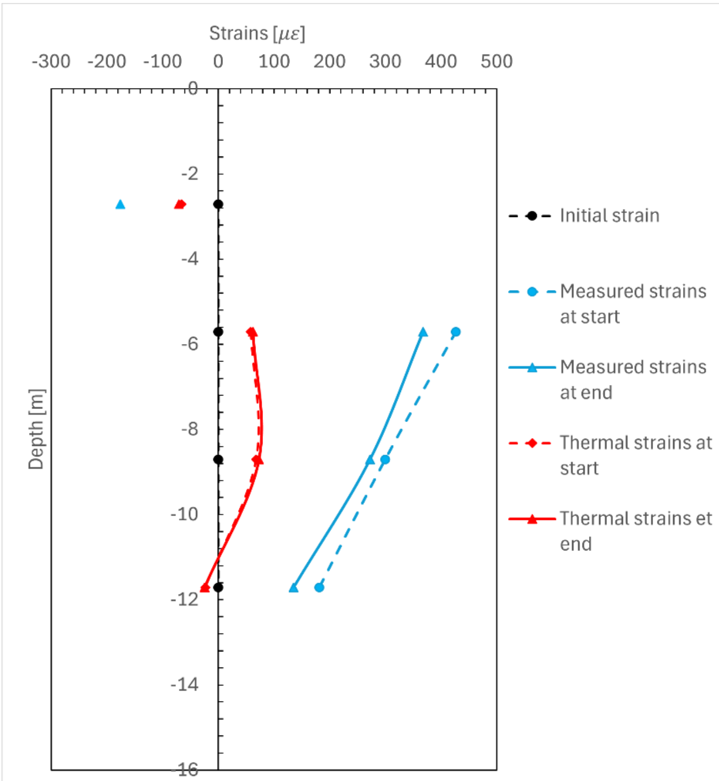

(b)

Figure 3.35: *Strains vs depth during thermo-mechanical test on micropile 5. (a) Thermo-mechanical test 1; (b) Thermo-mechanical test 2.*

The observed thermal strains and the free thermal strains are plotted in Figure 3.36. The free thermal strains can be calculated using equation 2.34. The calculated free thermal strains are 109 $\mu\varepsilon$, 103 $\mu\varepsilon$, and 106 $\mu\varepsilon$ for S4, S5, and S6 respectively. The observed thermal strains in S4 and S5 represent 53.54% and 65.66% of the free thermal strain, which were in line with previous studies (Bourne-Webb et al., 2009; Amatya et al., 2012). However, negative strains were observed at S6. These strains represented -21.96% of the free thermal strains.

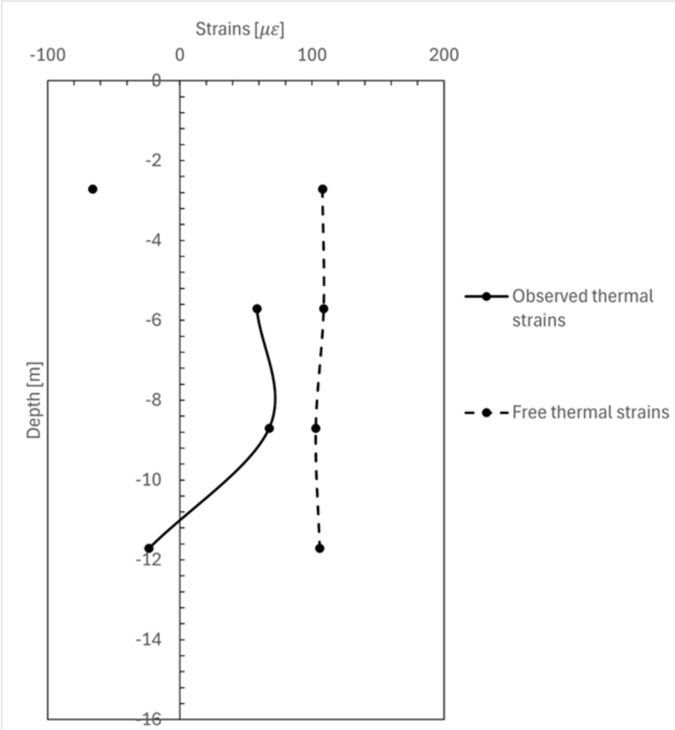

Figure 3.36: *Observed and free thermal strains during thermo-mechanical test on micropile*

3.8.2.3.5. Impact on ultimate limit state and serviceability limit state

To evaluate the effect of temperature variation on the ultimate limit state of energy micropiles, the induced thermal axial stresses, σ_T, were calculated using equation 2.36, as the product of the blocked thermal strains and the Young`s modulus of the grout, assumed to be 30 GPa. The calculated thermal stresses per degree Celsius are summarized in Table 3.11. Results indicate thermal stresses of 132.42 kPa/°C and 97.88 kPa/°C at sensors S4 and S5, respectively. These values are consistent with those reported in previous studies on energy piles (Bourne-Webb et al., 2009; Laloui et al., 2006). At S6, the computed stress was -219.48 kPa/°C, which indicates tensile stress and is notably higher than those at S4 and S5. As discussed in Section 3.8.2.3.4, sensor S6 is suspected to have malfunction; therefore, the stress values derived from this sensor should be interpreted with caution. The ratios of the axial stresses to the grout compressive strength, 35 MPa, are 3.03%, 2.23% and 5.02% for S4, S5, and S6 respectively. Although the observed thermal stresses are within a moderate range, they suggest that temperature variations could influence the load distribution in energy micropiles under certain conditions. Consequently, existing design approaches for energy micropiles may warrant re-evaluation if further evidence confirms temperature induced effects of practical significance. Further research is therefore recommended to better quantify these interactions and to inform future design guidelines for energy geostructures, especially in soft soils.

Table 3.11: *Thermally induced axial stresses*

Depth [m]	Thermally induced axial stress σ_T [kPa/°C]	$\left\| \sigma_T / f_{ck} \right\|$ [%]
5.71 (S4)	132.42	3.03
8.71 (S5)	97.88	2.23
11.71 (S6)	-219.48	5.02

The serviceability limit state can be evaluated by analyzing the micropile head displacements. These were manually recorded using a mechanical dial gauge and are illustrated in Figure 3.37a. During creep tests M1 and M2, the micropile head displacement remained nearly constant, with a slight reduction during M2 corresponding to the decrease in applied load. A noticeable increase in displacement occurred only when the load was increased back to 550 kN at t =16 hours.

Following M2 and prior to TM1, a small increase in head displacement is noticeable. This was probably due to the slight increase in micropile temperature during this period (about 2°C). During the first thermo-mechanical test (TM1), a head displacement increase of 3 mm was recorded, corresponding to a temperature rise of approximately 7.5 °C. This value was about three times that observed during the creep test (0.94 mm). Nevertheless, the total micropile head displacement was lower than 10 mm which is satisfactory for most building and civil engineering structures provided that the group settlement is not excessive (Tomlinson & Woodward, 2015). The rate at which displacement increased decreased once the micropile temperature stabilized. This suggests that large temperature variations in energy micropiles should be avoided during operation to prevent large displacements. "Apparent residual displacements" were also observed during the test, as the micropile head displacement did not return to its initial value when the load was restored to 550 kN. However, as shown in Figure 3.37b, six days after the test was ended and the micropile had cooled down to 7.7°C, strain measurements returned to approximately zero. Perhaps, the micropile head displacements also returned to near-zero values after cooling; unfortunately, this measurement was not recorded. Based on these observations, it may be concluded that micropile behavior was thermo-elastic during the test. Additionally, cyclic operation of energy micropiles is recommended to minimize the risk of permanent deformations or serviceability issues that may arise under long - term continuous thermal loading conditions.

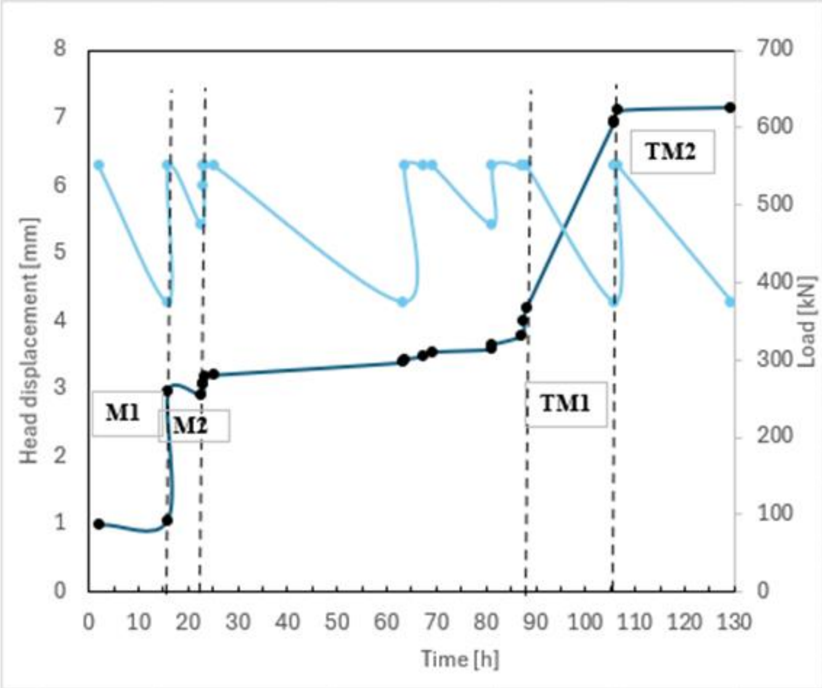

(a)

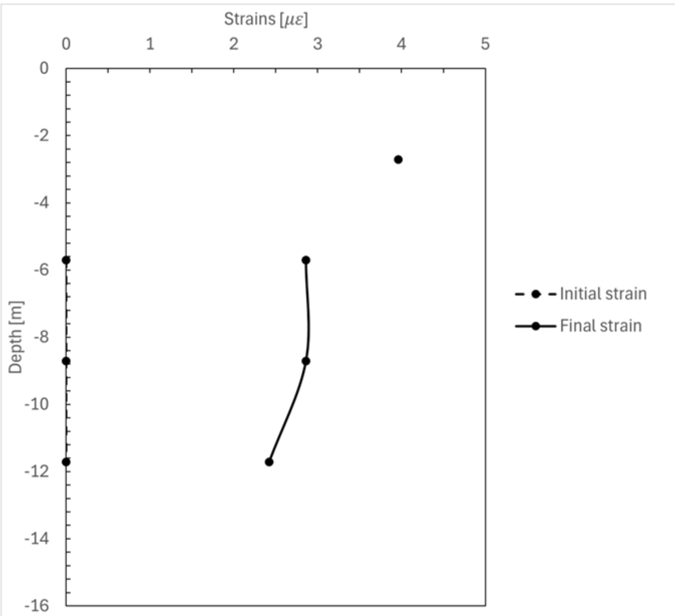

(b)

Figure 3.37: *Micropile head displacement and strains during the test on micropile 5. (a) Pile head displacement vs depth; (b)Residual strains after cooling vs depth.*

3.8.3. Micropile 6

Thermal testing on micropile 6 was conducted over a period of approximately 113 hours (4.7 days). The heat pump controller was replaced about 70 hours after the test started, resolving the issue with the continuously running compressor. This micropile has a diameter of 240 mm. The following sections present the results obtained from the test.

3.8.3.1. Fluid temperature

The variations in fluid inlet and outlet temperatures are shown in Figure 3.38. The average temperature difference between the inlet and outlet was approximately 1.06 °C, with a maximum of 2.406 °C. Sudden spikes in temperature difference observed immediately after the heat pump startup were excluded from the analysis.

This micropile has an active length of 14 m and was tested using a 39% Kilfrost Geo fluid circulated at an average flow rate of 7.2 l/min (0.00012 m³/s). The calculated average and maximum thermal power outputs are:

$$Q_{av} = \frac{1157.6\,\mathrm{kg/m^3} * 3129\,\mathrm{J/kgK} * 0.00012\,\mathrm{m^3/s} * 1.06°\mathrm{C}}{14.0\ \mathrm{m}} = 32.91\ \mathrm{W/m}$$

$$Q_{max} = \frac{1157.6\,\mathrm{kg/m^3} * 3129\,\mathrm{J/kgK} * 0.00012\,\mathrm{m^3/s} * 2.406°\mathrm{C}}{14.0\ \mathrm{m}} = 74.70\ \mathrm{W/m}$$

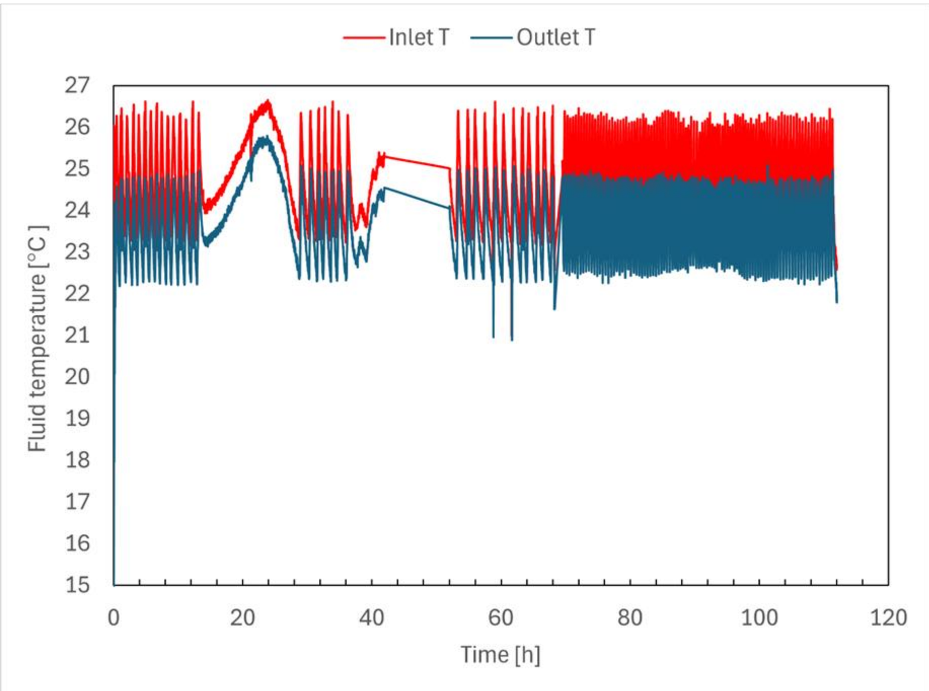

Figure 3.38: *Fluid temperature vs time during thermal test on micropile 6.*

3.8.3.2. Coefficient of performance COP

The total electrical energy consumption during the 112-hour testing period was 44.262 kWh. The corresponding thermal energy outputs are:

$$\text{Thermal energy output}_{\text{av}} = 32.91 * 14.0 * 112 = 51{,}602\ \text{Wh} = 51.60\ \text{kWh}$$

$$\text{Thermal energy output}_{\text{max}} = 74.70 * 14.0 * 112 = 117{,}129.6\ \text{Wh} = 117.13\ \text{kWh}$$

These values correspond to an average COP of approximately 1.17 and a maximum of 2.65. The COP for this micropile is higher than that of micropile 5 because the heat pump controller was replaced about 70 hours after the test began. From that point forward, the compressor operated properly, which improved the system's performance. However, since the issue was only resolved partway through the test, the average COP remained lower than the typical average for air source heat pump systems.

3.8.3.3. Micropile temperature

The temperature profile along the depth of the pile is shown in Figure 3.39. Similar to the observations from micropile 5, the highest temperature is recorded near the ground surface (approximately 1.0 m below ground level), likely due to the influence of higher outdoor air temperatures. Overall, the increase in micropile temperature appears to be uniform along the micropile's length.

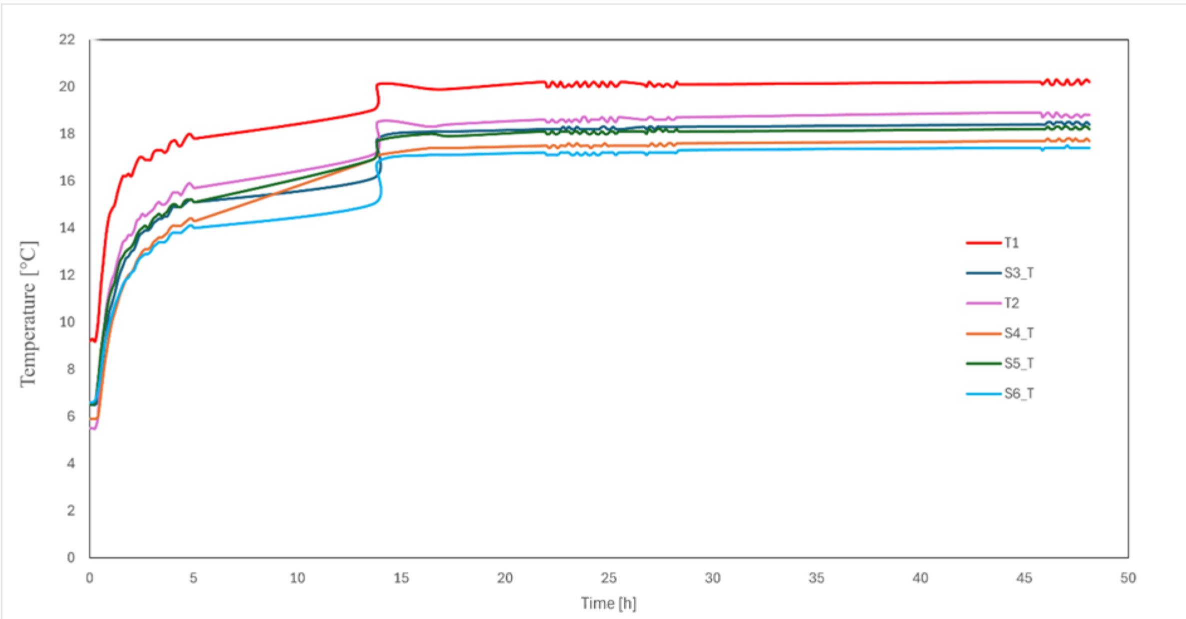

(a)

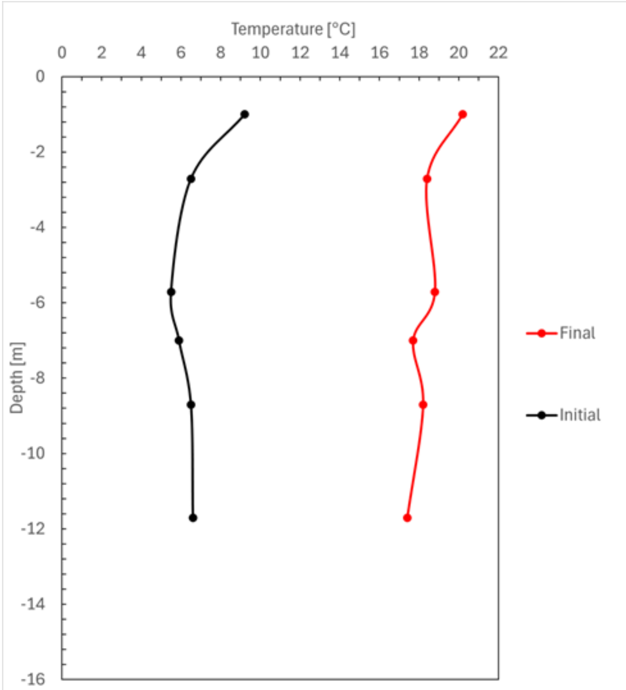

(b)

Figure 3.39: *Pile temperature during thermal test on micropile 6. (a) Pile temperature vs time time at depths 1.0 m (T1), 2.71 m (S3),5.71 m (S4), 7.0 m (T2), 8.71 m (S5) and 11.71 m (S6); (b) Pile temperature vs depth.*

3.8.3.4. Strains

Two strain sensors (S3 and S6) were damaged during installation; therefore, strain data were available at only two depths and are presented in Figure 5.40. Interestingly, while expansive (positive) strains were recorded at a depth of 8.71 m (S5), contractive strains (negative) were observed at 5.71 m (S4). Similarly, contractive strains were also observed at a depth of 11.71 m during the thermo-mechanical test on micropile 5 as discussed in Section 3.8.2.3.4. Given the different types of soil at these depths – silty clay at 5.71 m and sensitive clay at 11.71 m, it is unlikely that the contractive strains resulted from soil collapse. Further examination of sensor S4 indicated an unusually high sensitivity to temperature variations during the laboratory testing phase, a behavior also observed in sensor S6 of micropile 5. This consistency supports the interpretation that the recorded contractive strains were likely due to sensor malfunction rather than the soil thermal collapse. Nevertheless, further investigation is recommended to confirm this interpretation.

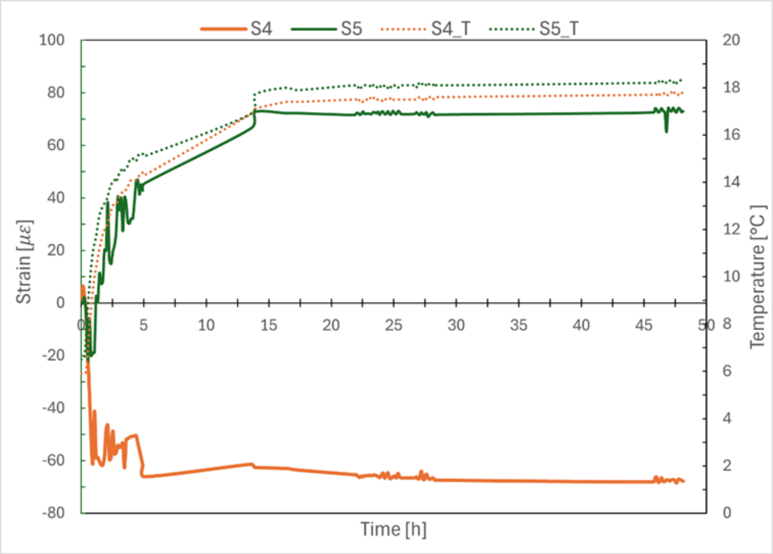

(a)

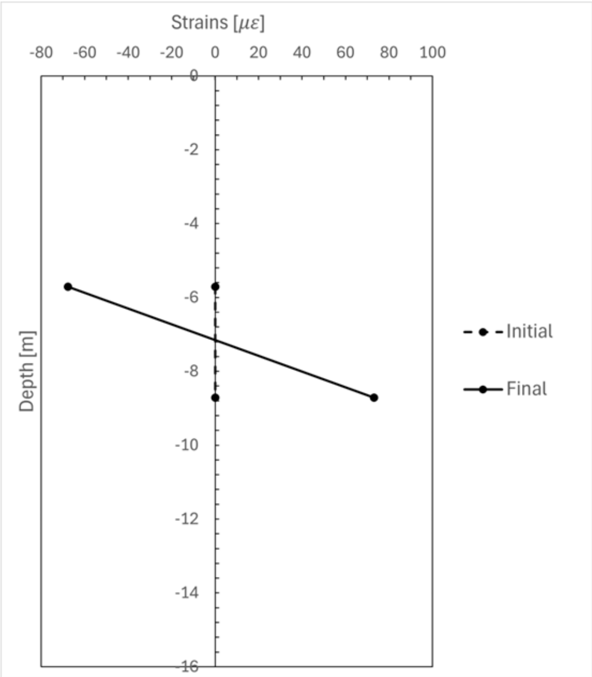

(b)

Figure 3.40: *Strains during thermal test on micropile 6 (a) Strain vs time time at depths 5.71 m (S4), and 8.71 m (S5); (b) Strain vs depth.*

The strains recorded at S5 correspond to approximately 62.45% of the free thermal strain (Figure 3.41), which is equivalent to a thermally induced axial stress of 112.72 kPa/°C calculated from the restrained (blocked) thermal strains.

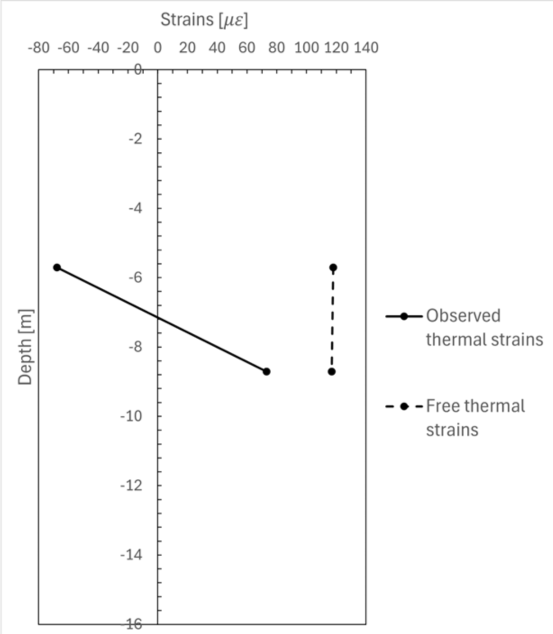

Figure 3.41: *Observed and free thermal strains during thermal test on micropile 6.*

3.8.4. Micropile 3

Thermal testing on micropile 3 was conducted over a period of approximately 120.32 hours (5.01 days). Unfortunately, three strain sensors (S3, S5, and S6) appear to have been slightly damaged during installation, as only temperature readings were recorded, and no strain data was obtained. Consequently, strain results will not be discussed. Additionally, one temperature sensor (T1) and one strain gauge (S4) were completely damaged. Hence, micropile temperature readings are only available for S3, T2, S5, and S6, which were installed at depths of 2.71 m, 7.00 m, 8.71 m, and 11.71 m. The following sections present the results obtained from the test.

3.8.4.1. Fluid temperature

The variations in fluid inlet and outlet temperatures are shown in Figure 3.42. The average temperature difference between the inlet and outlet was approximately 1.16 °C, with a maximum of 2.59 °C. Sudden spikes in temperature difference observed immediately after the heat pump startup were excluded from the analysis.

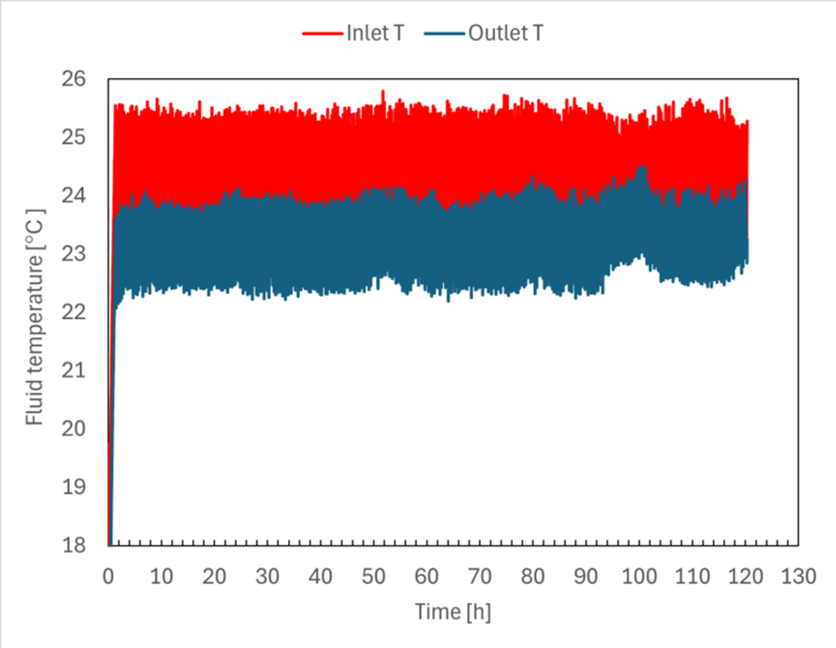

Figure 3.42: *Fluid temperature vs time during thermal test on micropile 3.*

This micropile has an active length of 14 m and was tested using a 39% Kilfrost Geo fluid circulated at an average flow rate of 7.2 l/min (0.00012 m³/s). The calculated average and maximum thermal power outputs are:

$$Q_{av} = \frac{1157.6\ \mathrm{kg/m^3} * 3129\ \mathrm{J/kgK} * 0.00012\ \mathrm{m^3/s} * 1.16°\mathrm{C}}{14.0\ \mathrm{m}} = 36.01\ \mathrm{W/m}$$

$$Q_{max} = \frac{1157.6\ \mathrm{kg/m^3} * 3129\ \mathrm{J/kgK} * 0.00012\ \mathrm{m^3/s} * 2.59°\mathrm{C}}{14.0\ \mathrm{m}} = 80.41\ \mathrm{W/m}$$

These results show that micropile 3 with a slightly bigger diameter (30 cm) compared to micropile 6 (24 cm), has a slightly higher thermal power. The difference is between 3 W/m and 6 W/m.

3.8.4.2. Coefficient of performance

The total electrical energy consumption during the 120-hour testing period was 34.989 kWh. The corresponding thermal energy outputs are:

$$\text{Thermal energy output}_{av} = 36.01 * 14.0 * 120.32 = 60{,}658.12\ \mathrm{Wh} = 60.66\ \mathrm{kWh}$$

$$\text{Thermal energy output}_{max} = 80.41 * 14.0 * 120.32 = 135{,}449.04\ \mathrm{Wh} = 135.50\ \mathrm{kWh}$$

These results correspond to an average COP of approximately 1.73 and a maximum of 3.87. Following the recent repair of the compressor system, two principal factors can explain the relatively low COP values compared with those typically reported for geothermal systems.

First, the efficiency of an exhaust-air heat pump, such as the one employed in this study, is strongly influenced by the outdoor air temperature. Lower ambient temperatures, as is characteristic of the Norwegian climate, reduce the COP because the compressor requires greater effort to maintain the desired thermal output. Second, the heat pump was oversized for this experimental setup, as the testing programme involved only one micropile test at a time. Oversizing resulted in frequent on–off cycling, which increased energy consumption and further lowered the effective COP. Therefore, the reported COP values are not representative of the real-world performance of geothermal micropile systems and should not be used for direct comparison. These findings highlight the importance of appropriate selection and sizing of the heat pump to ensure optimal system efficiency.

3.8.4.3. Micropile temperature

The micropile temperature was measured using one temperature sensor and three strain sensors equipped with embedded thermistors. The temperature profile along the depth of the micropile is shown in Figure 3.43. Overall, the increase in pile temperature appears to be uniform.

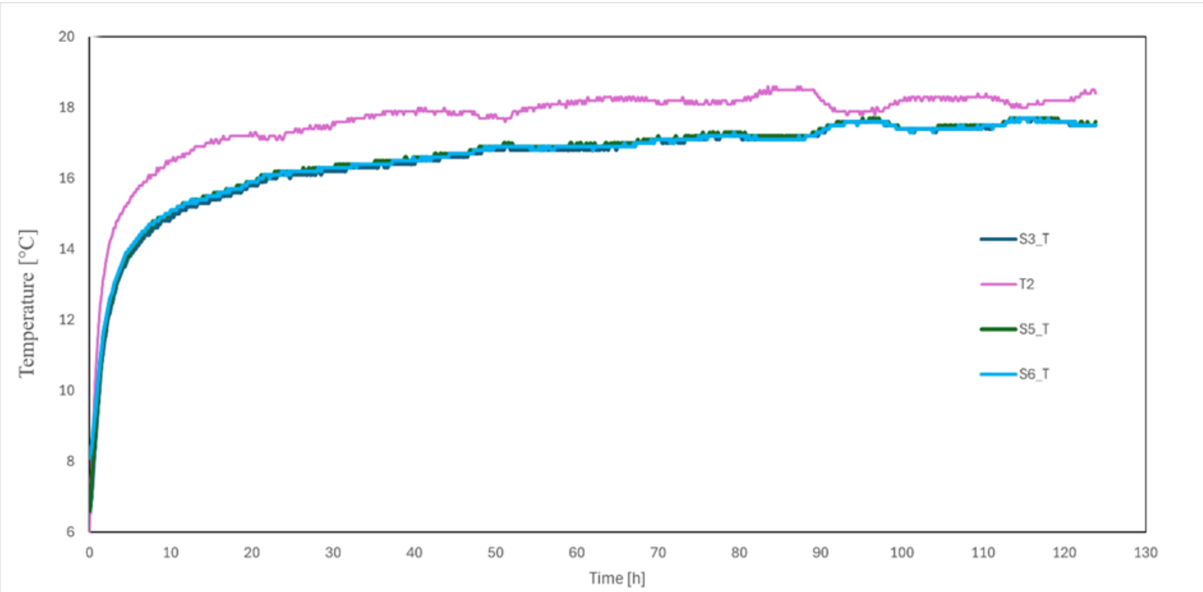

(a)

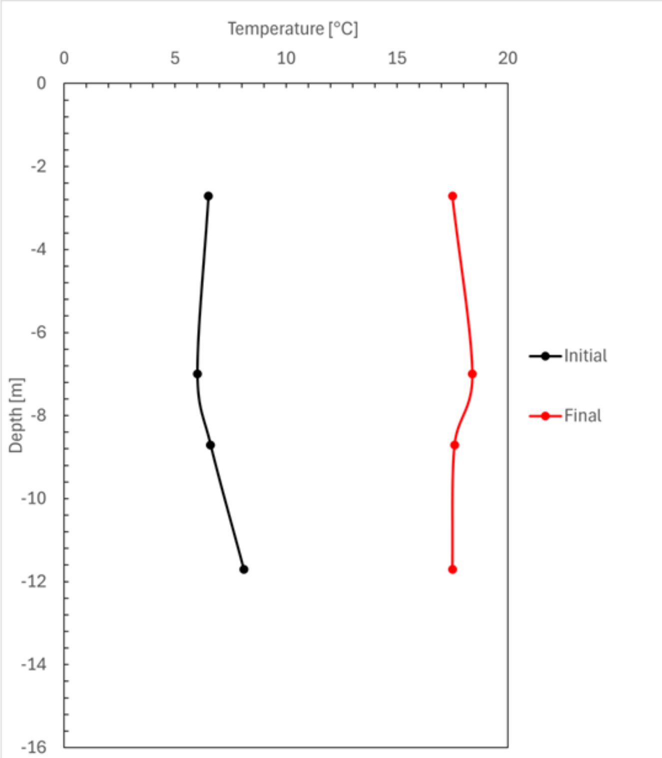

(b)

Figure 3.43: *Micropile temperature during thermal test on micropile 3. (a) Pile temperature vs time at depths 2.71 m (S3), 7.0 m (T2), 8.71 m (S5) and 11.71 m (S6). (b) Pile temperature vs depth.*

3.9. Limitations of the experimental work

Several limitations were encountered during the experimental program, which should be considered when interpreting the results.

From a thermal perspective, the performance of the heat pump impacted the coefficient of performance. The heat pump was oversized relative to the test setup, which caused frequent on–off cycling and unstable fluid temperatures. In addition, a control malfunction resulted in continuous operation at certain stages, leading to higher energy consumption and a lower apparent coefficient performance. To achieve the desired test set-up, an air-source heat pump was used instead of a ground-source unit; consequently, variations in outdoor air temperature influenced the performance. In practical applications, a ground-source heat pump would provide better efficiency.

There were also some instrumentation and data acquisition issues. Some strain sensors provided only temperature readings or showed signs of malfunction. There were also some interruptions with the data acquisition system, resulting in discontinuous records for fluid temperature and micropile strain. Hence, certain periods of the test could not be analyzed in detail. In addition, flow rate readings had to be calculated manually.

Additionally, the pipe length in the micropile was approximated, but the difference is likely to be within a few centimeters and therefore has a negligible effect on the results.

Maintaining a constant mechanical load during the creep and thermo-mechanical tests was challenging, which made it difficult to fully separate the effects of thermal and mechanical strains. As a result, slight quantitative variations may exist in the measured responses. Nevertheless, a reliable methodology was used, and the overall trends and observed behaviors are considered representative.

Although the thermal tests were conducted under summer conditions, with the micropile heated by fluid at approximately 25 °C, the results are still relevant for evaluating winter performance. In winter, the micropile system operates in reverse: heat is extracted from the ground and delivered to the building via a heat pump. Assuming an initial ground temperature of 6 °C, this results in a maximum thermal gradient of around 6 °C. Consequently, the thermal power output in winter may be lower than in summer. However, to accurately assess winter performance, additional tests involving heat extraction cycles are recommended.

3.10. Summary

This chapter has outlined the experimental program designed to investigate the thermal performance and thermo-mechanical behavior of energy micropiles. The testing campaign involved six micropiles installed in saturated clay at NTNU Dragvol Campus in Trondheim. Each micropile was equipped with one of the two innovative pipes and instrumented with temperature and strain sensors located at various depths and connected to a heat pump. The materials and equipment used, the sensor configurations, and the challenges encountered during the preparation of the field test have been reported in detail. Various solutions were attempted to overcome the challenges met, some of which proved only partially effective, highlighting the complexity of full-scale field testing.

The test results demonstrate that energy micropiles equipped with split-pipe and corrugated coaxial configurations effectively delivered thermal energy, achieving thermal power outputs between 32.91 W/m and 80.41 W/m under heating conditions at a set temperature of 25 °C. These findings confirm the viability of energy micropiles for building cooling applications. However, the coefficient of performance (COP) values of the exhaust-air-to-water heat pump, which ranged from 1.73 to 3.87, were lower than those typically reported for geothermal systems. This reduction is attributed to the low outdoor temperatures during testing and to the oversizing of the heat pump. It should be noted that the exhaust-air-to-water heat pump was employed solely for experimental purposes. In practical applications, both the type and capacity of the heat pump should be carefully selected to ensure optimal performance.

During the thermo-mechanical test on micropile 5 and the thermal test on micropile 6, expansive strains were observed along most of the micropile length, as expected, corresponding to 53.54% to 65.66% of the free thermal strains. The maximum thermally induced compressive stress, calculated from the blocked strains, was 132.42 kPa/°C, which represents about 3% of the grout's compressive strength. However, two sensors recorded contractive strains, an unusual response that may be attributed to sensor malfunction. Nonetheless, given the complex behavior of soft soils, further investigation is recommended. Additionally, temperature-induced micropile head displacements (3 mm) were approximately three times larger than those caused by mechanical loading alone (0.94 mm), but less than the allowable settlement for serviceability limit state. Upon unloading and cooling, strains values returned to near zero, suggesting a predominantly thermo-elastic response of the micropile under the tested conditions. Hence, energy micropiles can effectively be used as foundation elements and geothermal heat exchanger for heating and cooling buildings.

4. Numerical modelling and parametric analysis

4.1. Introduction

The experimental work in chapter 3 has demonstrated that the efficient utilization of low-enthalpy geothermal energy through energy micropiles represents a promising avenue for sustainable heating and cooling applications. However, while experimental studies provide important data on the thermal and mechanical behavior of energy micropiles, numerical modelling helps to explore performance under varying conditions.

In this chapter, a parametric study of energy micropiles equipped with the split pipe system is presented. The study consists of investigating how different design choices and operating parameters influence the thermal performance of the system. This includes exploring the effects of hollow bar thickness, micropile length and diameter, grout and filling thermal conductivity, flow rate, and geometric properties of the pipe.

4.2. Numerical model

The modelling process involves selecting appropriate software, creating a detailed geometric representation of the system, defining the governing equations, establishing initial and boundary conditions, and running the simulation. The aim is to accurately replicate the thermal behavior observed in the experimental setup and predict the long-term performance of the energy micropile under different operating conditions.

4.2.1. Software selection: COMSOL Multiphysics

COMSOL Multiphysics version 6.1 was chosen for this study due to its comprehensive capabilities in modeling and simulating complex multiphysics phenomena. It provides an integrated computational environment that supports the coupling of various physical processes, such as heat transfer and fluid dynamics. COMSOL's graphical user interface provides a streamlined workflow for defining models. Users can set up geometries, assign material properties, and configure boundary conditions. COMSOL includes a wide range of predefined physics interfaces designed for various engineering applications. In this study, the laminar flow and the heat transfer in porous media interfaces were employed to model the thermal behavior of the micropile.

4.2.2. Mathematical formulation

The fluid flow in the micropile is modelled using the continuity equation, which expresses the mass conservation for a stationary and incompressible flow, and the Navier-Stokes equation for incompressible flow, which describes momentum conservation.

Continuity equation (mass conservation):

$$\nabla \cdot \rho \boldsymbol{u} = 0 \tag{4.1}$$

Navier-Stokes equation (momentum conservation) for incompressible flow accounting for transient effects (Kundu et al., 2012):

$$\rho\left(\frac{\partial \boldsymbol{u}}{\partial t} + (\boldsymbol{u} \cdot \nabla)\boldsymbol{u}\right) = -\nabla p + \rho \boldsymbol{g} + \mu \nabla^2 \boldsymbol{u} \tag{4.2}$$

where ρ represents the fluid density [kg/m^3], $\boldsymbol{u}$ denotes the velocity field of the fluid [m/s], p signifies the pressure field [Pa], μ denotes dynamic viscosity, ∇ represents the gradient operator, · represents the dot product, and $\boldsymbol{g}$ represents the acceleration due to gravity vector.

The Single-phase fluid flow interfaces in COMSOL Multiphysics solve the following Navier Stokes equation (COMSOL, 2018a):

$$\rho \frac{\partial \boldsymbol{u}}{\partial t} + \rho(\boldsymbol{u} \cdot \nabla)\boldsymbol{u} = \nabla \cdot [-p\boldsymbol{I} + \tau] + \boldsymbol{F} \tag{4.3}$$

where τ is the viscous stress tensor [Pa], **F** is the volume force vector [N/m^3].

If the fluid is a Newtonian fluid, the viscous stress tensor τ, can be expressed as (COMSOL, 2018a) :

$$\tau = 2\mu \boldsymbol{S} - \frac{2}{3}\mu(\nabla \cdot \boldsymbol{u})\boldsymbol{I} \tag{4.4}$$

where **S** denotes the strain-rate tensor (COMSOL, 2018a):

$$\boldsymbol{S} = \frac{1}{2}(\nabla \boldsymbol{u} + (\nabla \boldsymbol{u})^T) \tag{4.5}$$

Replacing the expression of S in equation 4, τ can then be further expressed as:

$$\tau = \mu(\nabla \boldsymbol{u} + (\nabla \boldsymbol{u})^T) - \frac{2}{3}\mu(\nabla \cdot \boldsymbol{u})\boldsymbol{I} \tag{4.6}$$

Assuming $\boldsymbol{K} = \mu(\nabla \boldsymbol{u} + (\nabla \boldsymbol{u})^T)$:

$$\tau = \boldsymbol{K} - \frac{2}{3}\mu(\nabla \cdot \boldsymbol{u})\boldsymbol{I} \tag{4.7}$$

The Navier stokes equation can thus be rewritten as:

$$\rho \frac{\partial \boldsymbol{u}}{\partial t} + \rho(\boldsymbol{u} \cdot \nabla)\boldsymbol{u} = \nabla \cdot \left[-p\boldsymbol{I} + \boldsymbol{K} - \frac{2}{3}\mu(\nabla \cdot \boldsymbol{u})\boldsymbol{I}\right] + \boldsymbol{F} \tag{4.8}$$

For a stationary flow, we have $\frac{\partial \boldsymbol{u}}{\partial t} = 0$ since the velocity does not change with time and $\nabla \cdot \boldsymbol{u} = 0$ for an incompressible flow. If gravity forces $\rho \boldsymbol{g}$ are considered, the momentum equation can thus be finally expressed as:

$$\rho(\boldsymbol{u} \cdot \nabla)\boldsymbol{u} = \nabla \cdot [-p\boldsymbol{I} + \boldsymbol{K}] + \boldsymbol{F} + \rho \boldsymbol{g} \tag{4.9}$$

The mathematical modeling of heat transfer in energy pile systems involves discretizing the system domain into finite elements and solving a coupled system of partial differential equations (PDEs). These equations describe the spatiotemporal distribution of temperature within the system, accounting for heat conduction in materials like grout and soil, as well as convective heat transfer within fluid-carrying pipes.

The rate of heat transfer through a material by conduction is given by Fourier's law and can be expressed as:

$$\boldsymbol{q} = -k\nabla T \tag{4.10}$$

where $\boldsymbol{q}$ is the conductive heat flux vector (rate of heat transfer per unit area), k is the thermal conductivity of the material, and ∇T is the gradient of temperature (change in temperature per unit distance). k is positive when heat flows from regions of high temperature to low temperature.

The energy balance equation can be written as (COMSOL, 2018b):

$$\rho\frac{\partial E}{\partial t}+\rho\boldsymbol{u}\cdot\nabla E+\nabla\cdot\boldsymbol{q}=\sigma:\boldsymbol{D}+Q \tag{4.11}$$

where ρ is the density of the material [kg/m^3], E is the internal energy [J], $\boldsymbol{q}$ is the heat flux by conduction [W/m^2], $\boldsymbol{u}$ is the velocity vector [m/s], σ is the Cauchy stress tensor [Pa] , $\boldsymbol{D}$ is the strain rate tensor [s^{-1}] and Q represents any additional heat sources [W/m^3].

The heat transfer in solids interface of COMSOL Multiphysics solves for the following equation (COMSOL, 2018b):

$$\rho C_p(\frac{\partial T}{\partial t}+\boldsymbol{u}\cdot\nabla T)+\nabla\cdot\boldsymbol{q}=Q \tag{4.12}$$

where C_p is the specific heat capacity at constant stress [J/(kg · K)], T is the absolute temperature [K].

In the fluids interface, the heat transfer equation solved for is expressed as (COMSOL, 2018b):

$$\rho C_p(\frac{\partial T}{\partial t}+\boldsymbol{u}\cdot\nabla T)+\nabla\cdot\boldsymbol{q}=Q+Q_p+Q_{vd} \tag{4.14}$$

The second term at the right side of the equation, Q_p represents the work done by pressure changes and is calculated as:

$$Q_p=\alpha_p T(\frac{\partial p}{\partial t}+u\cdot\nabla p) \tag{4.15}$$

Where α_p is the coefficient of thermal expansion [K^{-1}] expressed as:

$$\alpha_p=\frac{-1}{\rho}\frac{\partial\rho}{\partial T} \tag{4.16}$$

For ideal gases,

$$\alpha_p=\frac{1}{T} \tag{4.17}$$

Q_{vd} represents viscous dissipation in the fluid:

$$Q_{vd} = \tau \colon \nabla \boldsymbol{u} \tag{4.18}$$

4.2.3. Initial and boundary conditions

To accurately model the thermal and fluid dynamics within the soil and micropile domains, some initial and boundary conditions were established. An initial temperature of 7 °C was considered for all the domains. A Newtonian fluid model has been assigned to the heat carrier fluid. A no slip condition has been assumed at the wall boundaries, thus the velocity at the walls is equal to zero.

$$\boldsymbol{u} = 0 \tag{4.19}$$

As the study was conducted in winter conditions, the inlet temperature of the heat carrier fluid has been taken to be 2°C. At the same point, a volumetric flow rate of 6 l/min has been imposed, and a fully developed flow boundary condition has been considered. This is mathematically expressed as:

$$\boldsymbol{u} \cdot \boldsymbol{t} = 0, \qquad P_{inl} : V_0 = -\int_{\partial\Omega_{inl}} \boldsymbol{u} \cdot \boldsymbol{n} dS \tag{4.20}$$

Where $\boldsymbol{u} \cdot \boldsymbol{t}$ denotes the velocity ($\boldsymbol{u}$) of the fluid at the boundary surface ($\boldsymbol{t}$) in the tangential direction, P_{inl} represents the pressure at the inlet boundary, V_0 represents the prescribed flow rate (or volumetric flow rate) at the inlet boundary, u represents the velocity vector field of the fluid, Ω_{inl}represents the boundary surface of the inlet and $\boldsymbol{n}$ represents the outward unit normal vector to the boundary surface.

The domain dimensions were chosen such that the boundary condition of the lateral surface does not affect the heat transfer of the pile and surrounding soil. A constant temperature of 7°C has been imposed at the lateral and bottom parts of the model, adhering to a Dirichlet boundary condition:

$$T = T_0 \tag{4.21}$$

Meanwhile, a Neumann boundary condition, thermal insulation, was considered at the top boundary of the model to represent the thermal insulation between the slab and the building (Sutman et al., 2020). The Neumann boundary condition is mathematically expressed as:

$$-\boldsymbol{n} \cdot \boldsymbol{q} = 0 \tag{4.22}$$

At the outlet, a static pressure condition has been assumed, with a pressure value of 108 kPa representing the circuit pressure (Ronchi et al., 2018). All the solid domains were assumed to be homogenous and isotropic materials. The simulations were carried out for a period of 30 days.

A nonlocal integration coupling over the boundary surface was defined to evaluate the outflow temperature at the outlet point of the pipes. The thermal power was calculated using the following thermal energy equation:

$$H = \frac{Q_{in}\, \rho_{hcf}\, C_p\, \Delta T}{L} \tag{4.23}$$

where H is the thermal power per unit length in W/m, Q_{in} is the volumetric flow rate of the heat carrier fluid in m^3/s, ρ_{hcf} is the carrier fluid density in kg/m^3, C_p its specific heat capacity in J/(kgK), ΔT is the difference between the inlet and the outlet temperature in K, and L is the active length of the micropile in m. More information on the EMP FE model validation with experimental data is available in literature (Yozy Kepdib et al., 2025b).

4.2.4. Thermal properties of materials

The thermal properties of the materials significantly influence heat transfer and storage behaviour. The surrounding soil acts as a heat source, with its thermal properties varying based on composition, moisture content, and compaction, directly impacting heat dissipation and storage. The grouted micropile is made of grout and steel with different properties. The heat transfer fluid is assumed to be water with temperature dependent characteristics. The properties of the materials given in Table 4.1 were obtained from literature (Ronchi et al., 2018, Abbasi, 2022).

Table 4.1: *Main properties of the materials used in the simulation of the grouted energy micropile.*

Properties	Fluid (Water at 25°C)	Pipes (HDPE)	Steel (S355J2H)	Grout	Soil (Clay)
Thermal conductivity [W/(m K)]	0.6	0.6	45	1.6	1.2
Specific heat capacity [J/(kg K)]	4186	2000	420	880	1800
Density [kg/m3]	1000	950	7850	2300	1700

4.2.5. Model geometry and Meshing

The model geometry was setup in COMSOL Multiphysics to represent an energy micropile embedded in a soil medium. To eliminate boundary interactions and ensure the accuracy of the numerical results, the model domain was set to a total width of 10 m and a height of 10 m. This dimension is sufficiently large to prevent any interference from the outer boundaries during the simulations. At the centre of the domain lies the energy micropile, which has a diameter of 300 mm and consists of a hollow steel bar surrounded by grout. The steel bar, made of fine-grained structural steel, has an external diameter of 103 mm and an internal diameter of 78 mm. The grout layer encases the steel, providing structural integrity and thermal conductivity enhancement. Within the hollow section of the steel bar, the split pipe was modelled. This pipe has an external diameter of 51 mm with a wall thickness of 2.8 mm and an internal separation wall of the same thickness, dividing the pipe into two flow channels. This separation wall terminates 30 mm above the bottom of the pipe.

In the present study, the micropiles with split pipes are fully modelled in 3D. The heat exchange fluid flows through these plastic pipes, entering via an inlet and exiting through an outlet. Further details about the design and specifications of the split pipe are provided in section 3.3.4.2.

The model geometry and its components are illustrated in Figure 4.1.

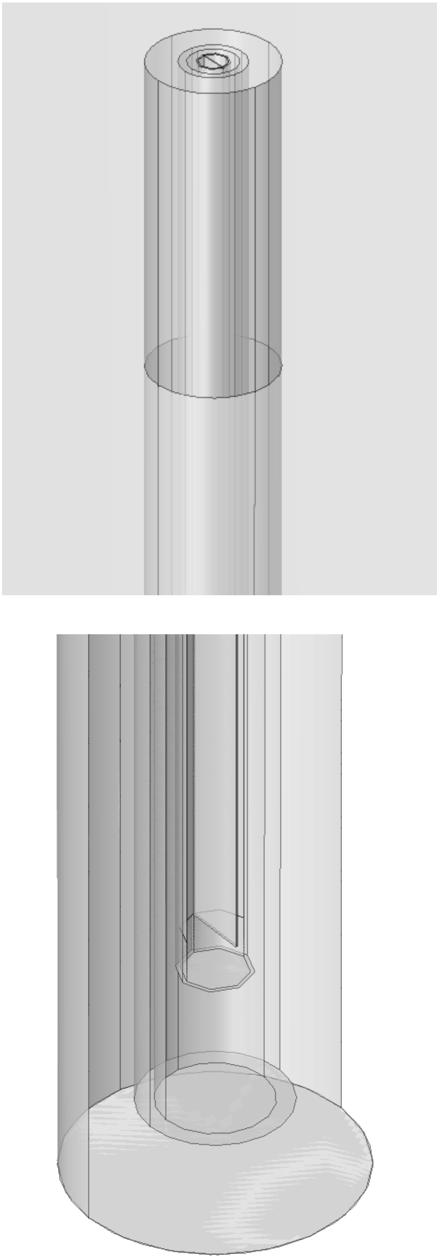

Figure 4.1: *Micropile geometry in COMSOL Multiphysics*

A physics-controlled mesh comprising free tetrahedral elements was used as shown in Figure 4.2. The mesh comprises of normal size elements at the soil, refined around the micropile and heat exchanger pipes. A finer mesh was applied near the interfaces to improve the resolution of thermal interactions. The total number of elements was approximately 23030 elements. The mesh was chosen to achieve rapid convergence and improve computational efficiency.

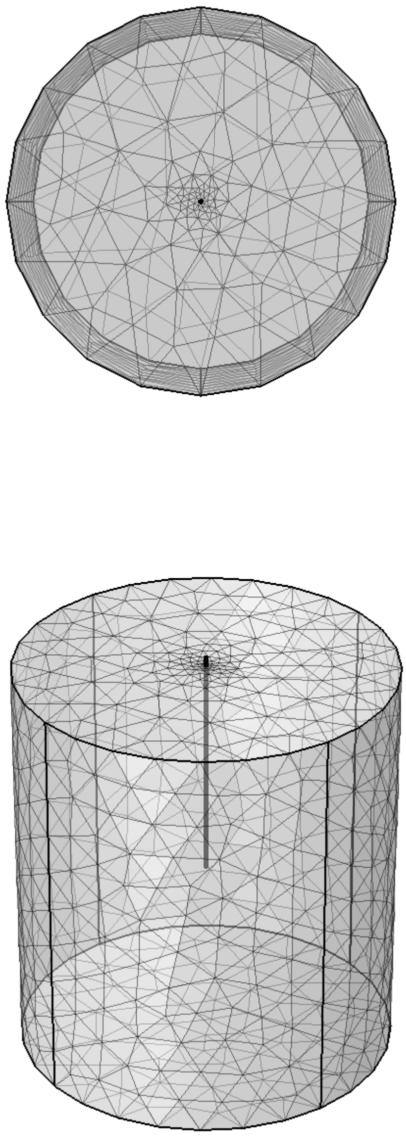

Figure 4 2: *Meshing*

4.3. Parametric analysis

The optimization of energy micropiles requires a comprehensive understanding of how various design parameters influence thermal performance. Given the multitude of factors involved – ranging from geometric characteristics to material properties- a full factorial analysis would be computationally expensive. To address this challenge, the present study employs the Taguchi Method by Dr. Genichi Taguchi, a powerful statistical tool for design optimization (Pal et al., 2009).

Implementing the Taguchi Method involves several key steps: first, defining the objectives of the analysis; then, selecting the design parameters and range of values; creating orthogonal arrays for each experiment; conducting the experiments, analysing the data, and confirming the results. The results are interpreted through a level average analysis. This technique helps to identify which of the design parameters has the greatest influence on the thermal performance of the micropile system. It works by comparing the average outcomes of each parameter at its different levels across all simulations of the orthogonal array.

For each parameter, the simulation results are grouped according to the level at which the parameter was set. The average value of the response is then calculated for each level. These averages give an indication of how changes in a single parameter affect the system's behaviour, independent of the other variables. Once the level averages are established, the influence of each parameter is measured by calculating the range, defined as the absolute difference between the highest and lowest average values. This difference gives a direct measure of the sensitivity of the thermal performance to that parameter. A larger range suggests that the parameter has a stronger effect on the output. All the parameters are then ranked based on these ranges, allowing a comparison of their relative importance.

The level average analysis not only helps in identifying the parameters that most affect thermal output, but it also supports the selection of the best combination of parameter levels. By observing which levels correspond to the most favourable average responses, an optimal design configuration can be proposed. A confirmation simulation can be done as a reliability check (Cecinato & Loveridge, 2015a; Ogunleye et al., 2020; Peace, 1993).

In this study, the response of the simulations is the thermal performance of the split pipe pile system, assessed using with the thermal power output. The thermal power exchanged is calculated using equation 4.23.

4.3.1. Selection of design parameters

The parameters selected for this study (Figure 4.3) were chosen based on their potential impact on the thermal performance of energy micropiles and the extent to which they can be designed. The micropile length and diameter are important because they determine the surface area available for heat exchange and the length over which heat is transferred, both of which affect the overall heat transfer efficiency. They are determined from structural and geotechnical design. The grout thermal conductivity is included since it plays a significant role in transferring heat between the micropile and the surrounding soil. The hollow bar (steel tube) thickness (t_b) was selected based on its influence on the thermal resistance of the micropile system and the structural design of micropiles. The filling thermal conductivity was chosen because it can vary during the installation process of self-grouting micropiles. To facilitate the installation, water may be added to the grout to reduce its density, which in turn may affect its thermal properties, as discussed in chapter 3. Fluid flow rate governs the convective heat transfer between the circulating fluid and the micropile body, influencing both the exchange fluid outlet temperature and the thermal power output. The partition wall thickness (t_{pw}) and height (h_{pw}) are important for preventing heat transfer between the inlet and outlet portions of the system. Increasing the thickness of the wall increases the resistance to heat flow between the inlet and the outlet fluid.

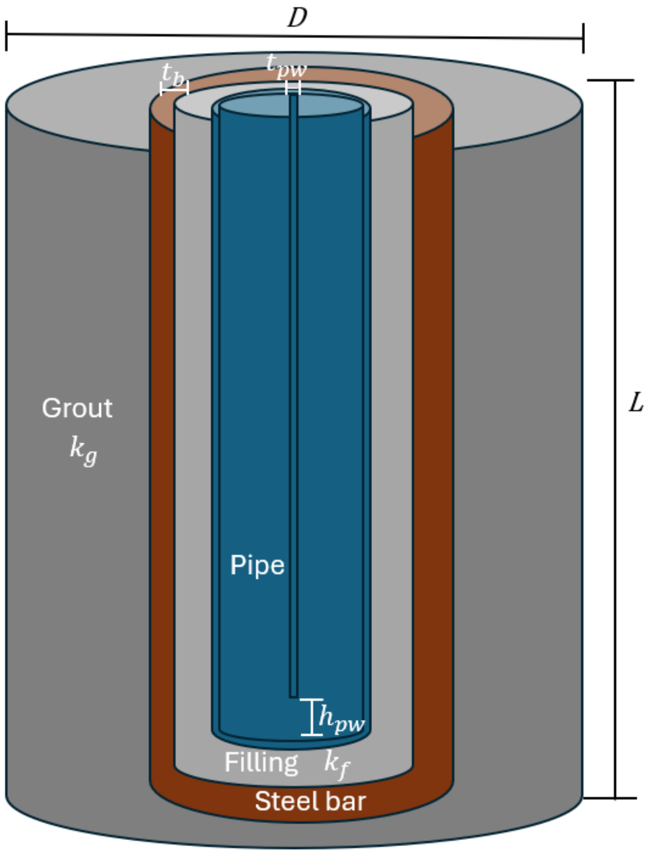

Figure 4.3:Design parameters for parametric analysis

The range of values selected for the design parameters as shown in Table 4.2 reflects realistic conditions based on actual project characteristics and practical considerations. For embedded length, three values are chosen: 12 m, 15 m, and 30 m, representing typical micropile lengths used in real-world applications. The pile diameter is set at 20 cm, 24 cm, and 30 cm, corresponding to the TITAN hollow bar sizes and the associated drill bit sizes of 17.5 cm, 22 cm, and 28 cm, respectively. Grout conductivity is varied between 0.6, 1.2, and 1.6 W/m·K, as these values cover a typical range for grout materials used in geothermal applications. Similarly, filling conductivity is also considered within the same range (0.6, 1.2, and 1.6 W/m·K), as the conductivity of the filling material is influenced by the grout's composition during installation.

The hollow bar thickness was chosen based on the common sizes available in the market, with values set at 25 mm and 31 mm for the bar 103/72 and 103/78 respectively. The fluid flow rate is varied between 2 l/min, 4 l/min, and 6 l/min, reflecting typical operational flow rates for micropile systems. The split pipe wall thickness is varied at 1.5 mm, 3 mm, and 4.5 mm, as these values represent feasible options for creating an effective partition between the inlet and outlet fluid portions. Finally, the partition wall height is varied at 30 mm, 50 mm, and 100 mm to explore the effect of different partition wall heights on the flow characteristics and heat transfer efficiency within the system. The range of parameter values ensures that the analysis remains relevant to practical applications while covering a broad spectrum of operational conditions.

Table 4.2*: Design parameters and their range of values*

Parameter	Unit	Minimum	Median	Maximum
Hollow bar thickness (t_b)	mm	25		50
Micropile length (L)	m	12	15	30
Grout conductivity (k_g)	W/mK	0.6	1.2	1.6
Partition wall thickness (t_{pw})	mm	1.5	3.0	4.5
Filling conductivity (k_f)	W/mK	0.6	1.2	1.6
Flow rate (Q_{in})	l/min	2	4	6
Micropile diameter (d)	mm	200	240	300
Partition wall height (h_{pw})	mm	30	50	100

The parameter values that are kept constant in the analysis are given in Table 4.3. Temperature dependent properties were assigned for the density, thermal conductivity and specific heat capacity of the exchange fluid, water.

Table 4.3: *Fixed parameter values*

Parameter	Unit	value
Inlet fluid temperature	°C	2
Initial temperature (fluid, grout, soil, pile)	°C	7
Pipe diameter	mm	51
Pipe thermal conductivity	W/mK	0.6
Ground thermal conductivity	W/mK	1,2
Fluid thermal conductivity	W/mK	0.6
Ground density	kg/m3	1700
Ground specific heat capacity	J/ (kg K)	1800
Concrete density	kg/m3	1910
Concrete specific heat capacity	J/ (kg K)	880

4.3.2. Design of parametric study

The parametric study involves 8 design parameters, 7 of which are tested at three levels, and 1 at two levels. This structure corresponds to the L18 orthogonal array used in the Taguchi method. The L18 array requires only 18 experiments (simulations), a significant reduction compared to the $3^7 * 2^1 = 4374$ simulations needed for a full factorial analysis. This efficiency reduces both time and cost. In the L18 orthogonal array, each row represents a unique combination of parameter settings for one experiment, and each column corresponds to one of the parameters. Within each column, the various levels of that parameter are distributed across the experiments. This design allows for a thorough exploration of the parameter space while keeping the number of simulations minimal. The combination of parameters tested in each of these experiments is shown in Table 4.4.

The significance of each parameter on the output variable can be determined by comparing the results obtained at different levels of that parameter. If the output changes significantly with different levels of parameter, it suggests that the parameter has a strong influence on the results. The orthogonality of the array ensures that each level of a parameter occurs an equal number of times across all experimental runs. As a result, the effects of other parameters are "balanced out," making it possible to isolate and accurately estimate the effect of each individual parameter (Cecinato & Loveridge, 2015a; Peace, 1993).

Table 4.4: *L18 orthogonal array of the Taguchi method*

	Parameter number							
Experiment number	1	2	3	4	5	6	7	8
1	min	min	min	min	min	min	min	min
2	min	min	med	med	med	med	med	med
3	min	min	max	max	max	max	max	max
4	min	med	min	min	med	med	max	max
5	min	med	med	med	max	max	min	min
6	min	med	max	max	min	min	med	med
7	min	max	min	med	min	max	med	max
8	min	max	med	max	med	min	max	min
9	min	max	max	min	max	med	min	med
10	max	min	min	max	max	med	med	min
11	max	min	med	min	min	max	max	med
12	max	min	max	med	med	min	min	max
13	max	med	min	med	max	min	max	med
14	max	med	med	max	min	med	min	max
15	max	med	max	min	med	max	med	min
16	max	max	min	max	med	max	min	med
17	max	max	med	min	max	min	med	max
18	max	max	max	med	min	med	max	min

The significance of each parameter on the output variable can be determined by comparing the results obtained at different levels of that parameter. If the output changes significantly with different levels of parameter, it suggests that the parameter has a strong influence on the results. The orthogonality of the array ensures that each level of a parameter occurs an equal number of times across all experimental runs. As a result, the effects of other parameters are "balanced out," making it possible to isolate and accurately estimate the effect of each individual parameter (Cecinato & Loveridge, 2015a; Peace, 1993) .

4.3.3. Data analysis and interpretation

The level average analysis method can be used to interpret the simulation results and identify the most influential design parameters on the thermal performance of the energy micropile. The response variable considered is the thermal power output.

The level average analysis method involves calculating the average thermal power output at each level of a given parameter to evaluate its influence on the system performance. For each parameter X, the mean response at level i is given by:

$$\bar{Y}_{X_i} = \frac{1}{n_i} \sum_{j=1}^{n_i} Y_{X_{i,j}} \tag{4.24}$$

where $\bar{\bar{Y}}_{X_i}$ is the average response at level i, $Y_{X_{i,j}}$ is the thermal power output from the j[th] experiment with parameter X at level i and n_i is the number of experiments at that level. The relative effect of the parameter is then quantified using the range:

$$\Delta X = \max\left(\bar{Y}_{X_i}\right) - min\ \left(\bar{Y}_{X_i}\right) \tag{4.25}$$

Parameters are ranked based on their ΔX values to identify those with the strongest effect on thermal performance.

4.4. Results

For each simulation, the thermal exchange power (Q) was recorded on day 1 and day 30. These simulations are referred to as "runs," and the full set of conditions and corresponding results is presented in Table 4.5. A confirmation run, based on the best-performing combination, was carried out to verify the accuracy of the analysis. The calculated thermal power with time is plotted in Figure 4.4.

For each parameter, the mean thermal power was calculated at each level, and the influence of the parameter was determined as the difference between the highest and lowest average values. This method allows a clear ranking of parameters based on their impact on system performance. Tables 4.6 and 4.7 summarize these effects for day 1 and day 30, respectively.

Table 4.5: *Simulations carried out in parametric analyses. The response, thermal exchange power at days 1 and 30 are at the right of the table. The confirmation run is at the bottom.*

	Hollow bar thickness [mm]	Length [m]	Grout conductivity [W/mK]	Partition wall thickness [mm]	Filling conductivity [W/mK]	Flow rate [l/min]	Micropile diameter [mm]	Partition wall height [mm]	Q at day 1 [W]	Q at day 30 [W]
Run 1	25	12	0.6	1.5	0.6	2	200	30	159.06	117.73
Run 2	25	12	1.2	3	1.2	4	240	50	241.24	150.02
Run 3	25	12	1.6	4.5	1.6	6	300	100	298.44	165.34
Run 4	25	15	0.6	1.5	1.2	4	300	100	208.73	148.60
Run 5	25	15	1.2	3	1.6	6	200	30	366.60	203.90
Run 6	25	15	1.6	4.5	0.6	2	240	50	229.29	161.01
Run 7	25	30	0.6	3	0.6	6	240	100	414.27	284.79
Run 8	25	30	1.2	4.5	1.2	2	300	30	270.705	214.44
Run 9	25	30	1.6	1.5	1.6	4	200	50	489.3	324.27
Run 10	31	12	0.6	4.5	1.6	4	240	30	198.192	131.96
Run 11	31	12	1.2	1.5	0.6	6	300	50	223.26	144.42
Run 12	31	12	1.6	3	1.2	2	200	100	239.184	156.9
Run 13	31	15	0.6	3	1.6	2	300	50	198.75	148.51
Run 14	31	15	1.2	4.5	0.6	4	200	100	279.255	175.97
Run 15	31	15	1.6	1.5	1.2	6	240	30	355.29	203.22
Run 16	31	30	0.6	4.5	1.2	6	200	50	494.79	329.40
Run 17	31	30	1.2	1.5	1.6	2	240	100	281.19	223.01
Run 18	31	30	1.6	3	0.6	4	300	30	454.2	311.64
Confirmation run	31	30	1.6	3	1.2	6	200	50	638.25	377.16

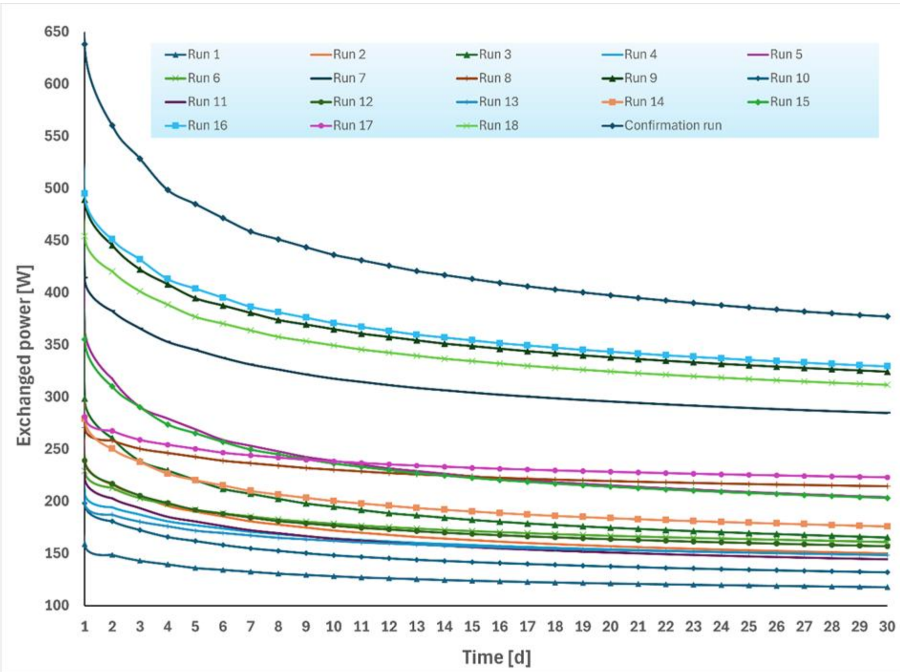

Figure 4.4: *Thermal power versus time from parametric analyses.*

Table 4.6: *Interpretation of parametric study on day 1 using the level average analysis method*

	Hollow bar thickness	Micropile length	Grout conductivity	Partition wall thickness	Filling conductivity	Flow rate	Micropile diameter	Partition wall height
Min	297.51	226.56	278.96	286.14	293.22	229.70	338.03	300.67
Med		272.99	277.04	319.04	301.66	311.82	286.58	312.77
Max	302.68	400.74	344.28	295.11	305.41	358.78	275.68	286.84
Effect	5.16	174.18	67.24	32.90	12.19	129.08	62.35	25.93
Ranking	8	1	3	5	7	2	4	6

Table 4.7: *Interpretation of parametric study on day 30 using the level average analysis method*

	Hollow bar thickness	Micropile length	Grout conductivity	Partition wall thickness	Filling conductivity	Flow rate	Micropile diameter	Partition wall height
Min	196.68	144.40	193.50	193.54	199.26	170.27	218.03	197.15
Med		173.53	185.29	209.29	200.43	207.08	192.34	209.61
Max	202.78	281.26	220.40	196.35	199.50	221.84	188.82	192.43
Effect	6.10	136.86	35.10	15.75	1.17	51.58	29.20	17.17
Ranking	7	1	3	6	8	2	4	5

From the analysis on day 30, the most influential parameter was the micropile length, followed by flow rate, grout thermal conductivity, and micropile diameter. These results are in line with expectations. Increasing the micropile length enhances the contact surface area between the pile and the ground, which improves heat exchange (Cecinato & Loveridge, 2015; Cecinato & Salciarini, 2022). Additionally, longer piles enable access to deeper, thermally stable soil layers.

Flow rate strongly affects fluid velocity inside the pipes and thus thermal performance (Cecinato & Loveridge, 2015; Cecinato & Salciarini, 2022; Ronchi et al., 2018). Higher flow rates typically improve performance by enhancing convective heat transfer and turbulent flows. However, high flow rates result in increased pressure losses. Therefore, while increasing flow rate can be beneficial, it must be optimized to avoid excessive energy demand for pumping.

Grout conductivity is another important factor, as grout forms a large part of the micropile's volume. A highly conductive grout helps minimize thermal resistance between the pipes and the ground. Many researchers have investigated methods to increase the conductivity of grout or concrete (Allan & Kavanaugh, 1999; Allan & Philippacopoulos, 1998; Ciardi, 2023; Ciardi et al., 2023; Maatouk, 2016; Śliwa et al., 2017). Using grout with higher thermal conductivity can be a practical way to increase performance without altering structural design.

Pile diameter also affects thermal output, especially for larger piles that can accommodate multiple pipe circuits. However, in the case of micropiles -due to their limited size - the number of pipes that can be installed is restricted. As such, while diameter does play a role, its effect is less significant compared to that in larger bored piles.

Parameters related to the geometry of the internal pipe system - such as partition wall height, partition wall thickness, and hollow bar thickness - had a comparatively smaller influence on the system's thermal performance. The partition wall thickness slightly increases the thermal resistance between the inlet and outlet flow paths, potentially reducing thermal short-circuiting. However, increasing thickness also reduces the cross-sectional area of each pipe channel, which in turn limits fluid volume and can lead to higher pressure drops.

The influence of hollow bar thickness was minimal within the range of values tested. Although thicker bars have larger structural capacity, they contribute little to thermal exchange in this context. A broader range of values might have a more noticeable effect, but within the dimensions considered in this study, the impact is negligible.

Filling conductivity had the least effect on system performance on day 30. This is consistent with previous findings (Ronchi et al., 2018), who observed little variation in thermal power when changing the conductivity of the filling material. Hence, increasing the water content in the grout filling to improve workability and reduce viscosity during pipe insertion, has a negligible impact on the thermal performance. This is especially relevant for the self-drilling energy micropile installation method discussed in Chapter 3.

Overall, the results confirm that the most effective ways to enhance thermal performance in energy micropiles are by optimizing pile length, flow rate, and grout properties. Adjustments to internal pipe geometry, while still relevant for hydraulic and mechanical performance, have limited thermal impact within the range of values considered.

As shown in Table 4.5, the confirmation run designed using the best performing levels of each parameter showed significantly higher thermal output compared to all individual runs, further validating the analysis method and confirming the importance of carefully selecting design parameters to maximize performance.

4.5. Summary

This chapter has presented parametric analysis and the key assumptions adopted to investigate the thermal performance of energy micropiles with the split pipe system. The methodology, based on the Taguchi design of experiments, explores variations in design and operational parameters in order to assess their impact on heat exchange efficiency. Results highlight that micropile length, fluid flow rate, and grout thermal conductivity are the most influential factors affecting thermal performance while changes in internal pipe geometry and steel bar section had only a marginal effect.

5. Application of energy micropiles: foundation element and geothermal heat exchanger of 5-floor building in Norway

5.1. Introduction

This chapter demonstrates how energy micropiles can effectively provide both foundation support and geothermal heating to buildings. The realistic case study is a five-floor residential and commercial building (designated as R+4), with reinforced concrete floors and masonry walls. The building has a footprint of 500 m^2 (25 m * 20 m). The micropiles, primarily designed to meet structural and geotechnical requirements, are adapted to incorporate thermal functionality. The thermal performance is assessed through numerical simulations using COMSOL. Although the building is not physically constructed, the design is based on typical structural and thermal loads expected in such a context. Additionally, a 30-year cost analysis is conducted to compare energy micropiles and electric heaters.

5.2. Structural design

To estimate the structural loads, standard assumptions based on conventional construction practices and relevant codes were used. The ground floor slab is assumed to be 0.4 m thick, while the intermediate slabs and the roof are each 0.2 m thick, giving a total slab thickness of 1.2 m. Assuming the unit weight of concrete to be 25 kN/m^3, the total dead load from the slabs is calculated as:

$$\text{slab load} = (25\ \text{kN/m}^3 * 1.20\ \text{m}) * 500\ \text{m}^2 = 15\ 000\ \text{kN}$$

The external walls are assumed to be 0.24 m thick and 3.5 m high per floor and constructed with masonry ($\gamma_{\text{masonry}} = 10\ \text{kN/m}^3$). Using the full building perimeter, the total external wall load is:

$$\text{External wall load} = 10\ \text{kN/m}^3 * 0.24\ \text{m} * (3.5\ \text{m} * 4) * \big((25\ \text{m} + 20\ \text{m}) * 2\big) = 3024\ \text{kN}$$

An internal wall load of 2,000 kN is assumed, bringing the total wall load to approximately 5,024 kN.

For variable loads, a live load of 2.5 kPa is assumed on each of the four floors, and 0.5 kPa on the roof (to account for snow). This results in:

$$\text{Live load} = \big((2.5\ \text{kPa} * 4) + 0.5\ \text{kPa}\big) * 500\ \text{m}^2 = 5250\ \text{kN}$$

According to Eurocode 7 and DIBt specifications, the design load is determined by applying safety factors of 1.35 for permanent loads and 1.5 for variable loads:

$$\text{Design loads} = (15000 \text{ kN} + 5024 \text{ kN}) * 1.35 + (5250 \text{ kN} * 1.5) = 34\ 907.4 \text{ kN}$$

Foundation grid layout and load distribution

The foundation is assumed to be an 8*6 rectangular grid layout of 48 micropiles, 3.5 m away from each other. The load per micropile is calculated as:

$$\text{Load per micropile} = \frac{34\ 907.4 \text{ kN}}{48} = 727.24 \text{ kN}$$

Two types of TITAN hollow bars were considered: the 103/78 with a characteristic capacity of 1,770 kN, and the 73/56 with 865 kN. Applying a partial safety factor of 1.15, the design resistances are:

TITAN 103/78: 1,770 / 1.15 ≈ 1,540 kN

TITAN 73/56: 865 / 1.15 ≈ 752 kN

Given that the 73/56 satisfies the load requirement while offering cost advantages, it was selected for the final design.

5.3. Geotechnical design

Assuming a skin friction q_s= 60 kPa for tubular grouted piles in cohesive soils (Table 2.13) and a drill bit diameter of 200 mm, the micropile diameter was taken as 220 mm, considering a 20 mm grout enlargement. Using conventional axial pile design equations as indicated in the German standard (DIN, 1054), the required micropile length to resist the design load through skin friction is estimated as:

$$L = \frac{1.4 * 727.24}{3.14 * 0.22 * 60} \approx 25 \text{ m}$$

5.4. Thermal design

For thermal design, a heating demand of 50 W/m² was assumed, reflecting typical residential heating loads in cold climates such as Norway. With a building footprint of 500 m² across five floors, the total estimated heating requirement is:

$$\text{Heating load} = 50 \text{ W/m}^2 * 500 \text{ m}^2 * 5 \text{ floors} = 125 \text{ kW}$$

Numerical simulation was conducted using COMSOL Multiphysics as described in chapter 4, to evaluate the heat extraction capacity of the energy micropiles. The micropile configuration included a 220 mm diameter, 25 m long micropile with split pipes and a heat transfer fluid circulating at a flow rate of 6 l/min. The outer pipe diameter was 51 mm. Winter conditions were assumed, with an initial ground temperature of 7°C, representative of Norwegian subsurface temperatures.

The simulation showed that each micropile can extract approximately 332.9 W of thermal energy. With 48 micropiles installed in the foundation, the total thermal power output of the system is:

$$\text{Total thermal power } = 48 * 332.9 \text{ W} = 15.98 \text{ kW}$$

Assuming a geothermal heat pump with a coefficient of performance of 4, the total heat delivered to the building becomes:

$$\text{COP} = \frac{\text{Heat output}}{\text{electrical input}}$$

$$\text{Heat output} = \text{EMP thermal power} + \text{electrical input}$$

Let electrical input = x.

$$\text{Heat output} = \text{EMP thermal power} + \text{x}$$

$$\text{Heat output} = \text{COP} * \text{electrical input}$$

$$\text{Heat output} = 4\text{x}$$

$$4\text{x} = 15.98 \text{ kW} + \text{x}$$

$$\text{x} = \frac{15.98 \text{ kN}}{3} = 5.33 \text{ kW}$$

$$\text{Heat output} = 4 * 5.33 \text{ kW} = 21.32 \text{ kW}$$

This total output represents approximately 17.06% of the building's total heating demand. While not sufficient to meet the total heating demand, the energy micropile system demonstrates strong potential as a complementary renewable heating solution. Particularly in retrofit or urban environments with limited space for boreholes, micropiles provide dual functionality: structural support and geothermal energy extraction. System performance can vary depending on soil thermal conductivity, moisture content, and temperature.

5.5. Ground temperature

Based on the simulation results shown in Figure 5.1, the operation of the energy micropile system over a 30-day winter period leads to a localized decrease in ground temperature. On day 1, the temperature at 1 meter from the micropile center remained at the initial ground temperature of 7 °C. By day 30, this temperature had dropped to approximately 6.3 °C. A noticeable reduction in temperature was observed up to around 2.5 meters from the micropile center, beyond which the ground temperature remained unchanged. This cooling effect is expected due to continuous heat extraction but stays within acceptable limits from an environmental standpoint. Although no significant ground temperature change was observed within the 30-day timeframe, the results highlight the importance of appropriate micropile spacing and seasonal operation for better thermal performance and to avoid risks such as ground freezing or overheating.

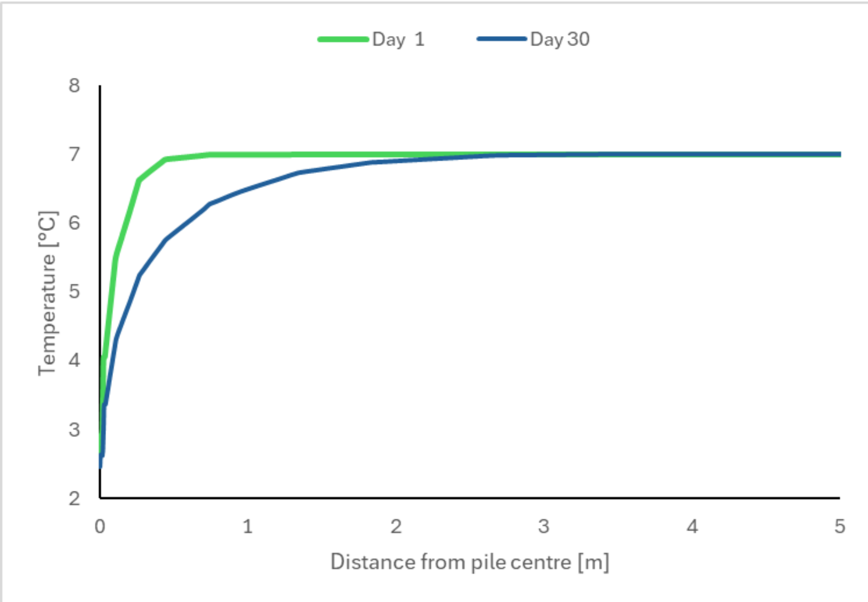

Figure 5.1: *Ground temperature vs depth*

5.6. Cost analysis

This section presents the results of the cost analysis. It should be noted that the prices used may not exactly reflect actual market values, as estimations were made for the purpose of the analysis. However, the prices are considered realistic and suitable for drawing meaningful conclusions.

5.6.1. Energy micropiles system

5.6.1.1. Micropiles

Using TITAN 73/56 hollow bars, the total material cost for the micropiles (excluding grout) is approximately 85,032 Euros as detailed in Table 5.1.

Table 5.1: *Material cost of micropiles*

Pos.	Quantity	Unit	Description	Price per unit	Total value
1	336	pc.	0330720045 Hollow Bar TITAN 73/56 3,00 m, black	147.00 EUR	49,392.00 EUR
2	48	pc.	0330720046 Hollow Bar TITAN 73/56 4,00 m, black	196.00 EUR	9,408.00 EUR
3	336	pc.	0430720063 Coupling Nut TITAN 73/56 Ø 89 x 180 mm, black with steel ring	36.00 EUR	12,096.00 EUR
4	336	pc.	0130720090 Centralizer TITAN 73 Ø 130 mm, cast iron, black	15.70 EUR	5,275.20 EUR
5	48	pc.	0130720063 Washer Plate TITAN 73/53 + 73/56 175 x 175 x 35 mm, black	36.00 EUR	1,7280.00 EUR
6	96	pc.	0130720050 Spherical Collar Nut TITAN 73 SW 95 x 70 mm, black	36.80 EUR	3,532.80 EUR
7	48	pc.	0130730057 Hardened Clay Bit TITAN 73 Ø 200 mm	75.00 EUR	3,600.00 EUR
Total amount					**85,032.00 EUR**

5.6.1.2. Installation cost of piles

Assuming installation costs to be equal to material costs, the standard foundation installation is 85,032 EUR. The installation cost of the energy micropiles has been increased by 2% to account for the work associated with heat exchange pipes. Thus, the total installation cost is:

$$\text{Installation cost of energy micropiles} = 85{,}032 \ * 1.02 = 86{,}732.64 \text{ Euros}$$

5.6.1.3. Pipes

The pipe system includes probes, connectors and fittings. The material cost of the pipes is detailed in Table 5.2.

Table 5.2: *Material cost of pipes*

Pos.	Quantity	Unit	Description	Price per unit	Total value
1	48	pc.	Probe head-pipe connector	9.90 EUR	475.20 EUR
2	48	pc.	Probe head with supply/return connection 32 mm	39.00 EUR	1,872.00 EUR
3	48	pc.	Coupler	6.90 EUR	331.20 EUR
4	48	pc.	Geothermal probe	168.75 EUR	8,100.00 EUR
5	48	pc.	Geothermal probe short length surcharge	25.00 EUR	1,200.00 EUR
Total amount					**11,978.40 EUR**

5.6.1.4. Heat exchange fluid

The total exchange fluid volume required for 48 micropiles, 25 m long each with a filling volume of 1.4 L/m is:

$$\text{Volume of exchange fluid} = 1.4 \text{ L/m} * 48 * 25 \text{ m} = 1680 \text{ L}$$

Using a 1:1 water–glycol mix and a glycol cost of 102 EUR per 25 L (Varmeshop, 2025), the total cost is:

$$\text{Cost of ethylene glycol} = 0.5 * 1680 \text{ L} * \frac{102 \text{ Euros}}{25\text{L}} = 3427.2 \text{ Euros}$$

5.6.1.5. Heat pump

A 22 kW Junkers Bosch brine/water heat pump costs approximately 17,798 Euros (Heizungsdiscount24.de, 2025.).

5.6.1.6. Electricity cost

For a heat pump operating 8 hours per day over 30 days at 5.33 kW, the energy consumption would be:

$$\text{Operating time} = 8\ \text{h} * 30 = 240\ \text{h}$$

$$\text{Energy consumption} = 240\ \text{h} * 5.33\ \text{kW} = 1279.2\ \text{kWh}$$

Assuming 0.1902 euros per kWh (Countryeconomy.com, 2025.), then the monthly electricity cost of the heat pump is

$$\text{Electricity cost of heat pump} = 0.1902\ \text{euros per kWh} * 1279.2\ \text{kWh}$$
$$= 243.30\ \text{euros per month}$$

5.6.2. Standard electrical heating

5.6.2.1. Material costs-heaters

In Norway, the dominant source of heating is electricity. To provide 21.32 kW, 12 units of 2 kW electric heaters are needed. If one heater costs 250 Euros, then the total cost of heaters will be:

$$\text{Total cost of electric heaters} = 12 * 250 = 3000\ \text{Euros}$$

5.6.2.2. Electricity cost

Assuming the electric heater operates 8 hours per day, the electricity consumption and cost per month would be:

$$\text{Electricity consumption} = 240\ \text{hours} * 21.32\ \text{kW} = 5116.8\ \text{kWh}$$

$$\text{Electricity cost for heating} = 0.1902\ \text{euros per kWh} * 5116.8\ \text{kWh}$$
$$= 973.22\ \text{euros per month}$$

5.6.3. 10-Year cost comparison

Table 5.3 presents a summary of the cost estimates calculated in the previous section. It compares the total expenses associated with two heating systems - Energy Micropiles (EMP) and a standard electric heater - over 10-year (Table 5.3) and 30-year (Figure 5.2) periods. These figures include both the initial installation costs and the yearly running expenses, offering a clear view of how the overall cost of each system builds up over time. Note that this projection excludes installation of underfloor heating, transportation, maintenance, and assumes no change in electricity price beyond 4% interest rate adjustment.The electricity cost at year n is calculated as:

$$\text{Cost at year n} = \text{C1} * (1 + \text{r})^{\text{n}-1}$$

Where C1 is the cost at year 1, r = 0.04 is the interest/inflation rate and n is the year.

Table 5.3: *Cost comparison between energy micropiles and electric heaters*

Category	**Energy micropile (EUR)**			**Electric heater (EUR)**		
	1 month	1 year	10 years	1 month	1 year	10 years
Exchange fluid	3427.2	3427.2	3427.2	N.A	N.A	N.A
Pipes	11,978.40	11,978.40	11,978.40	N.A	N.A	N.A
Piles	85,032	85,032	85,032	85,032	85,032	85,032
Piles installation	86,732.64	86,732.64	86,732.64	85,032	85,032	85,032
Heat pump	17,798	17,798	17,798	N.A	N.A	N.A
Electric heater	N.A	N.A	N.A	3000	3000	3000
Electricity cost	243.30	2919.6	4155.50	973.22	11,678.64	16,622.35
Total (EUR)	205,211.54	207,887.84	209,642.614	174,037.22	184,742.64	189,686.346

Note: This projection excludes installation of underfloor heating, transportation, maintenance, and assumes no change in electricity price beyond 4% inflation rate adjustment.

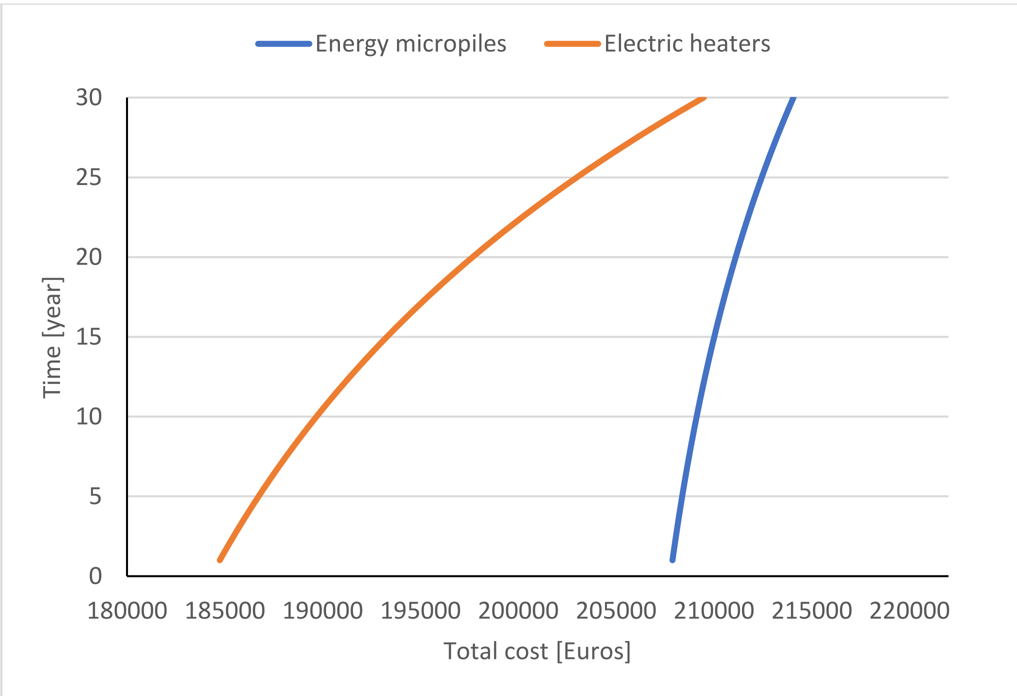

Figure 5.2: *Comparison between cost of energy micropiles and electric heaters for heating buildings in the Norwegian context.*

While electric heaters may appear more economical in the short term, the EMP system emerges as the more advantageous option over the long term. In the first year, the installation cost of the

EMP system is significantly higher than that of the electric heater. However, its lower electricity consumption results in slower increase in cumulative costs over time. By year 30, the total cost of the EMP system is only approximately 2.19% higher than that of the electric heater, compared to a difference of 12.52% in year 1. This narrowing gap indicates that the EMP system becomes increasingly cost-effective with time. The relatively stable expenses of the EMP system make it a more suitable choice for long-term planning.

A key parameter influencing this economic comparison is the coefficient of performance of the ground source heat pump integrated within the EMP system. In this study, A COP value of 4 was assumed, representing typical performance. However, the COP can vary between 3 and 6 in practical applications, depending on system design, local ground temperature, and seasonal climate fluctuations. Variations in COP directly affect usable heat output and electricity consumption, thereby influencing both the annual operating cost and the overall return on investment. For example, a COP of 6 would have increased heat output from 21.32 kW to 31.98 kW, which represents approximately 25.58% of the building`s heating demand. Additionally, for the heat output of 21.32 kW, the monthly electricity consumption would have reduced from 1279.2 kWh to 852 kWh which represents a 33.4% drop in electricity cost.

Furthermore, when coupled with complementary renewable energy sources such as a solar power system and battery storage, the electricity cost of the EMP system could potentially be reduced to zero. Although such integration increases the initial investment, it can drastically reduce or even eliminate electricity costs over the system´s lifespan, enhancing the long-term economic and environmental benefits.

5.7. Advantages, limitations and environmental considerations of energy micropiles for heating buildings

Energy micropiles offer a promising solution for sustainable building heating and cooling. By combining structural support with geothermal energy extraction, this technology provides dual functionality and contributes to the decarbonization of the building sector. However, while this technology presents several advantages, it also faces notable technical and environmental challenges that must be addressed to ensure reliable performance and broader adoption.

One of the primary benefits of energy micropiles lies in their long-term economic performance. Although the initial installation cost is relatively high, mainly due to material cost and sometimes drilling cost, this cost can be mitigated through government subsidies, green energy incentives, and institutional funding. Over time, the operating costs of energy micropiles are considerably lower than those of conventional electric or fossil-fuel-based heating systems.

This is largely due to the reduced reliance on fluctuating electricity prices and the low energy consumption once the system is in operation. Additionally, these systems typically require minimal maintenance, which further contributes to their long-term cost-effectiveness. From a technical perspective, energy micropiles offer several operational advantages. The system relies on ground-source heat, which is continuously available and not subject to weather variability, unlike solar or wind energy. When coupled with underfloor heating systems, energy micropiles can deliver a more uniform and efficient heat distribution compared to traditional radiators. The integration of heating and cooling functionality into the building's foundation also reduces the spatial requirements for separate energy systems, offering a compact solution particularly well-suited for urban environments. Moreover, because they are also used as foundation elements, energy micropiles can be deployed without significant additional land use. Furthermore, by using the earth as a heat source, they help lower the overall carbon footprint of building operations. Reduced dependence on electricity - especially when the system is partially or fully powered by on-site renewable energy such as photovoltaics—translates to fewer greenhouse gas emissions over the system's lifespan.

Despite their advantages, several challenges must be carefully considered. Thermally extracting heat from the ground lowers the temperature of the surrounding soil, which, if not properly monitored, can lead to soil freezing. In extreme cases, this may compromise the structural integrity of the foundation or affect nearby underground infrastructure. Additionally, prolonged heat extraction can alter the local hydrogeological conditions, including changes in groundwater flow or minor soil shrinkage. These risks necessitate careful site-specific design, thermal modelling, and long-term monitoring strategies. Furthermore, the technology is still relatively new in many countries, and there is limited expertise in the design, installation, and long-term operation of such systems. The thermo-mechanical behavior of energy micropiles in soft soil and sensitive soil is complex and requires further investigation. In fact, temperature variations in the micropile may alter the load distribution and accelerate creep. This knowledge gap may slow down implementation of energy micropiles.

5.8. Summary

A practical application of energy micropiles for heating buildings has been presented. The results showed that the energy micropile system could meet approximately 17.06% of the building’s monthly heating demand, highlighting its potential as a supplemental low-carbon energy source. A 30-year life-cycle cost analysis was also conducted, comparing the energy micropile system with conventional electric heating. Although the initial investment cost of energy micropiles is higher, the long-term operating costs are comparable. Energy micropiles offer additional advantages in terms of energy efficiency and environmental impact. Overall, this study demonstrates the technical and economic feasibility of energy micropiles as a sustainable solution for building heating and cooling, particularly in space-constrained or retrofit applications.

6. Conclusions and future outcomes

This doctoral research contributes to the growing field of low enthalpy geothermal energy by investigating the use of energy micropiles as a dual-function system, providing both structural support and geothermal heating and cooling. The study combines full-scale field experiments with numerical modeling to evaluate both the thermal performance and the thermo-mechanical behavior of energy micropile systems under realistic operational conditions.

The experimental campaign involved six micropiles installed at NTNU Dragvoll Campus in Trondheim, Norway. The micropiles were 15 m long, with diameters 240 mm and 300 mm, and were installed in a layered soil consisting of stiff, soft, and sensitive (possibly quick) clay. Two innovative plastic pipe systems, not commonly used in energy geostructures - the corrugated coaxial pipe and the split pipe - were utilized as heat exchange pipes. The micropiles were subjected to a series of tests including pull-out load test, creep test, thermo-mechanical, and purely thermal testing. All tests, except for the load test, were conducted for an average duration of 05 days. Thermal loading consisted of circulating the heat exchange fluid at a temperature of 25 ± 2 °C, while mechanical loading consisted of subjecting the pile to a constant mechanical load of 550 kN. Parameters such as strain, pile temperature, micropile head displacement, inlet and outlet fluid temperatures, flow rate and energy consumption were continuously recorded.

Test results showed that the thermal power output of the energy micropiles ranged between 32.91 W/m and 80.41 W/m, comparable to values reported for other geothermal systems. The calculated coefficients of performance (COP) ranged from 1.73 to 3.87, which are lower than the typical range of 3 to 5 reported in the geothermal literature. This reduced performance is attributed primarily to the low ambient air temperatures during testing and to oversizing of the heat pump and should therefore not be used for comparison purposes. The efficiency of an air-source heat pump is influenced by the outdoor air temperature; lower temperatures increase compressor workload and energy consumption, thereby reducing the COP. Under real operating conditions, a geothermal heat pump would typically be used instead, resulting in higher efficiency due to the relatively stable ground temperatures throughout the year. Additionally, oversizing the heat pump causes frequent on–off cycling, which further increases energy consumption and decreases overall efficiency. These findings highlight the importance of appropriate selection and sizing of heat pumps to ensure optimal system performance.

From a thermo-mechanical perspective, the strain measurements were consistent with well-established findings in the literature (Amatya et al., 2012; Bourne-Webb et al., 2013), confirming that piles tend to expand when subjected to heating loads. Owing to restraint provided by the surrounding soil, the observed expansive thermal strains were 53.53% and 65.56% of the free thermal strains, as expected. However, two sensors recorded contractive thermal strains during heating. Although heating of saturated clay can increase pore water pressure and reduce soil strength, potentially leading to partial collapse, the slight temperature increase observed in the pile (maximum 11 °C) is unlikely to unlikely to significantly affect the surrounding soil. Both sensors that exhibited these anomalous readings were previously identified during laboratory testing as being highly sensitive to temperature fluctuations, which according to the manufacturer, should be an indication of malfunction. It is therefore hypothesized that the contractive strains recorded during the thermal and the thermo-mechanical tests were likely caused by sensor malfunction rather than the thermal collapse of the surrounding soil. Nevertheless, given complex behavior of clay and previous observations of contractive strains in a heated pile reported by McCartney and Murphy (2017), further investigation is required to improve understanding of the micropile-soil interaction under coupled thermal and mechanical loadings.

The thermally induced compressive axial stresses calculated from the blocked strains were maximum 132.42 kPa/°C, representing 3% of the grout compressive strength. Although these thermal stresses are moderate, they indicate that temperature variations could influence the load distribution in energy micropiles under certain conditions. Consequently, existing design methodologies for energy micropiles may require re-evaluation if further evidence confirms temperature-induced effects of practical significance.

Additionally, micropile head displacements also varied under different loading scenarios. While displacements increased gradually during the creep test, rapid displacement was observed at the start of thermal loading. For instance, a 7.5 °C increase in micropile temperature resulted in a head displacement increase of 3 mm, approximately three times the value observed under mechanical loading alone during the creep test (0.94 mm). This suggests that large temperature variations can affect serviceability limit states and should therefore be carefully considered in design. Nevertheless, the total head displacement was lower than 10 mm which is satisfactory for most building and civil engineering structures provided that the group settlement is not excessive (Tomlinson & Woodward, 2015). Upon unloading and subsequent cooling, the strain values returned close to zero, indicating a predominantly thermo-elastic response of the micropile under the tested conditions.

To assess the impact of various design parameters on the thermal performance of energy micropiles, a parametric study was conducted using the Taguchi method. Eight parameters were selected: micropile length, diameter, grout thermal conductivity, steel tube thickness, filling thermal conductivity, flow rate, and the internal partition wall's thickness and height. Seven parameters were tested at three levels, and one parameter was tested at two levels. A total of 18 simulations were performed using an L18 orthogonal array. The results, interpreted with the level average analysis method, confirmed that the most influential parameters were micropile length, grout thermal conductivity, and fluid flow rate. Internal pipe geometry showed a minimal impact on thermal efficiency within the tested range of values. Although high flow rates enhance thermal performance, they are also associated with increased pressure losses. Therefore, an optimized design of energy micropiles must carefully balance thermal performance and energy consumption.

To demonstrate practical feasibility, a 30-day numerical simulation using COMSOL Multiphysics was performed for a realistic building project in Norway. The foundation design was based on structural and geotechnical criteria to ensure that thermal design did not compromise on initial micropile design. A detailed numerical model was developed incorporating local climatic data, building heat demand, and subsoil thermal properties. The results showed that the energy micropiles could meet approximately 17.06% of the building's monthly heating demand, highlighting its potential as a supplemental low-carbon energy source. Additionally, the effect on the ground temperature was minimal, with a maximum temperature change of 0.7 °C observed within 2.5 meters from the micropile center, without any indication of ground freezing. Nevertheless, long-term studies are required to assess potential risks associated with cumulative ground cooling. Furthermore, a 30-year life-cycle cost analysis was performed, comparing the energy micropile system with conventional electric heating. The analysis showed that, although the total cost of the micropile system remained higher than that of electric heating, the difference decreased significantly, from 12.52% in the first year to 2.19% after 30 years. Moreover, integrating the energy micropile system with solar panels and battery storage could potentially reduce electricity costs to almost zero. Hence, despite higher initial investment costs, long-term operating expenses are comparable, with potential benefits in terms of energy efficiency and environmental impact.

In conclusion, this research demonstrates the technical and economic feasibility of energy micropiles as a sustainable solution for heating and cooling buildings, particularly in space-constrained or retrofit applications. Despite their small size, the thermal performance of energy micropiles is comparable with other geothermal systems. Additionally, better performance can be achieved through careful design choices, particularly regarding pipe configuration, micropile length, grout conductivity and fluid flow rate. Beyond buildings heating and cooling application, energy micropiles offer promising applications for infrastructure such as road and bridge de-icing. However, several aspects, such as long-term thermal performance and thermo-mechanical behavior in sensitive clays, groundwater variation, ground temperature changes, cyclic loading effects, and group interactions between micropiles, require further investigation to inform reliable and efficient design strategies. With continued research and support, energy micropiles have the potential to contribute significantly to advancing sustainable buildings and infrastructures.

References

Abbasi, S. (2022). *Thermal analysis of steel geothermal energy pile foundation*. Norwegian University of Science and Technology, NTNU.

Akrouch, G. A., Sánchez, M., & Briaud, J. L. (2014). Thermo-mechanical behavior of energy piles in high plasticity clays. *Acta Geotechnica*, *9*(3), 399–412. https://doi.org/10.1007/s11440-014-0312-5

Allan, M. L., & Philippacopoulos, A. J. (1998). *Thermally conductive cementitious grouts for geothermal heat pumps*.

Allan, M. L., & Kavanaugh, S. P. (1999). Thermal conductivity of cementitious grouts and impact on heat exchanger length design for ground source heat pumps. *HVAC and R Research*, *5*(2), 85–96. https://doi.org/10.1080/10789669.1999.10391226

Amatya, B. L., Soga, K., Bourne-Webb, P. J., Amis, T., & Laloui, L. (2012). Thermo-mechanical behaviour of energy piles. *Geotechnique*, *62*(6), 503–519. https://doi.org/10.1680/geot.10.P.116

Barla, M., & di Donna, A. (2018). Energy tunnels: concept and design aspects. *Underground Space (China)*, *3*(4), 268–276. https://doi.org/10.1016/j.undsp.2018.03.003

Barla, M. (2022). *Introduction : Geostrutture energetiche*.

Barla M. & Insana A. (2023). Energy tunnels as an opportunity for sustainable development of urban areas. *Tunnelling and Underground Space Technology*, *132*. https://doi.org/https://doi.org/10.1016/j.tust.2022.104902

Batini, N., Rotta Loria, A. F., Conti, P., Testi, D., Grassi, W., & Laloui, L. (2015). Energy and geotechnical behaviour of energy piles for different design solutions. *Applied Thermal Engineering*, *86*, 199–213. https://doi.org/10.1016/j.applthermaleng.2015.04.050

Bourne-Webb, P. J., Amatya, B., Soga, K., Amis, T., Davidson, C., & Payne, P. (2009). Energy pile test at Lambeth College, London: geotechnical and thermodynamic aspects of pile response to heat cycles. *Géotechnique*, *59*(3), 237–248. https://doi.org/https://doi.org/10.1680/geot.2009.59.3.237

Bourne-Webb, P. J., Amatya, B., & Soga, K. (2012). A framework for understanding energy pile behaviour. *Proceedings of the Institution of Civil Engineers: Geotechnical Engineering*, *166*(2), 170–177. https://doi.org/10.1680/geng.10.00098

Bourne-Webb, P. J., Bodas Freitas, T. M., & Da Costa Gonçalves, R. A. (2016). Thermal and mechanical aspects of the response of embedded retaining walls used as shallow geothermal heat exchangers. *Energy and Buildings*, *125*, 130–141. https://doi.org/10.1016/j.enbuild.2016.04.075

Brandl, H. (2006). Energy foundations and other thermo-active ground structures. *Géotechnique*, *56*(2), 81–122. https://doi.org/https://doi.org/10.1680/geot.2006.56.2.81

Brozovsky, J., Corio, S., Gaitani, N., & Gustavsen, A. (2021). Evaluation of sustainable strategies and design solutions at high-latitude urban settlements to enhance outdoor thermal comfort. *Energy and Buildings*, *244*. https://doi.org/10.1016/j.enbuild.2021.111037

Bruce, D. A., DiMillio, A. F., & Juran, I. (1997). Micropiles: the state of practice Part 1: Characteristics, definitions and classifications. *Institution of Civil Engineers*, *1*(1), 25–35.

Caltrans. (2015). *Foundations Manual Chapter 13, Micropiles*.

Casagrande, B., Saboya, F., McCartney, J. S., & Tibana, S. (2022). Investigation of a field-scale energy micropile in stratified soil under cyclic temperature changes. *Geomechanics for Energy and the Environment*, *29*. https://doi.org/10.1016/j.gete.2021.100263

Cecinato, F., & Loveridge, F. A. (2015). Influences on the thermal efficiency of energy piles. *Energy*, *82*, 1021–1033. https://doi.org/10.1016/j.energy.2015.02.001

Cecinato, F., & Salciarini, D. (2022). Energy performance assessment of thermo-active micro-piles via numerical modeling and statistical analysis. *Geomechanics for Energy and the Environment*, *29*. https://doi.org/10.1016/j.gete.2021.100268

Chin, F. K. (1970). Estimation of piles not carried to failure. *Proceedings of the Second Southeast Asian Conference on Soil Engineering*, 81–90.

Ciardi, G., Madiai, C., & Tamagnini, C. (2023). Numerical study of the thermal performance of an energy micropile. *International Symposium on Numerical Analysis of Geomaterials*. Retrieved June 4, 2024, from http://www.nange.info/

Ciardi, G., Oliynyk, K., Madiai, C., & Tamagnini, C. (2023). Thermal Conductivity of Cement–Based Grouts for Energy Micropiles: Preliminary Experimental Investigation. In A. Ferrari, G. Guido, M. Ziccarelli, & M. Rosone (Eds.), *Geotechnical Engineering in the Digital and Technological Innovation Era* (pp. 785–791). Springer Series in Geomechanics and Geoengineering. https://doi.org/https://doi.org/10.1007/978-3-031-34761-0_94

Clarke, B. G., Agab, A., & Nicholson, D. (2008). Model specification to determine thermal conductivity of soils. *Proceedings of the Institution of Civil Engineers: Geotechnical Engineering*, *161*(3), 161–168. https://doi.org/10.1680/geng.2008.161.3.161

Coduto, D. P. (2001). *Foundation design principles and practices*.

COMSOL. (2018). *Pipe Flow Module*. www.comsol.com/blogs

COMSOL. (2018). *Heat Transfer Module User's Guide*. www.comsol.com/blogs

CountryEconomy.com. (2025). Norway - Household electricity prices. Retrieved October 30, 2025, from https://countryeconomy.com/energy-and-environment/electricity-price-household/norway

Davisson, M. T. (1972). High capacity piles. *Proceedings of Lecture Series on Innovations in Foundation Construction*, 81–112.

De Moel, M., Bach, P. M., Bouazza, A., Singh, R. M., & Sun, J. O. (2010). Technological advances and applications of geothermal energy pile foundations and their feasibility in Australia. In *Renewable and Sustainable Energy Reviews* (Vol. 14, Issue 9). Elsevier Ltd. https://doi.org/10.1016/j.rser.2010.07.027

Di Donna, A., Cecinato, F., Loveridge, F., & Barla, M. (2017). Energy performance of diaphragm walls used as heat exchangers. *Proceedings of the Institution of Civil Engineers: Geotechnical Engineering*, *170*(3), 232–245. https://doi.org/10.1680/jgeen.16.00092

Faizal, M., Bouazza, A., & Singh, R. M. (2016). An experimental investigation of the influence of intermittent and continuous operating modes on the thermal behaviour of a full scale geothermal energy pile. *Geomechanics for Energy and the Environment*, *8*, 8–29. https://doi.org/10.1016/j.gete.2016.08.001

Faizal, M., Moradshahi, A., Abdelmalek Bouazza, ;, Mccartney, J. S., & Asce, M. (2022). *Soil thermal response to temperature cycles and end boundary conditions of energy piles*. https://doi.org/10.1061/(ASCE)GT.1943

Fang, J., Kong, G., & Yang, Q. (2022). *Group performance of energy piles under cyclic and variable thermal loading*. https://doi.org/10.1061/(ASCE)GT.1943

Friedr. Ischebeck GmbH (2014). Geothermal energy

Friedr. Ischebeck GmbH (2016). *TITAN micropiles design and construction manual*.

Friedr. Ischebeck GmbH (2022). *Foundations and underpinning with TITAN micropiles*

Florides, G., & Kalogirou, S. (2005). *Annual ground measurements at various depths*.

Gao, J., Zhang, X., Liu, J., Li, K., & Yang, J. (2008). Numerical and experimental assessment of thermal performance of vertical energy piles: An application. *Applied Energy*, *85*(10), 901–910. https://doi.org/10.1016/j.apenergy.2008.02.010

Gashti, E. H. N., Uotinen, V. M., & Kujala, K. (2014). Numerical modelling of thermal regimes in steel energy pile foundations: A case study. *Energy and Buildings*, *69*, 165–174. https://doi.org/10.1016/j.enbuild.2013.10.028

Gehlin, S. (2002). *Thermal response test method development and evaluation*.

Gerola, M., Lupattelli, A., Cecinato, F., Salciarini, D., & Arola, T. (2023). *Numerical analysis of the behaviour of energy micropiles used for heat storage: A case study in Turku (Finland)* (pp. 808–815). https://doi.org/10.1007/978-3-031-34761-0_97

German Geotechnical Society. (2013). *Recommendations on Piling (EA-Pfähle)*. Wilhelm Ernst &Sohn.

Heizungsdiscount24.de. (2025.). *Junkers Bosch 2- stufige Sole/Wasser Erdwärmepumpe Supraeco T 220-2, 22 kW*. Retrieved October 30, 2025, from https://www.heizungsdiscount24.de/waermepumpen/junkers-bosch-2-stufige-solewasser-erdwaermepumpe-supraeco-t-220-2-22-kw.html

IEA. (2023, July). *Tracking clean energy progress 2023*. Assessing Critical Energy Technologies for Global Clean Energy Transitions.

IEA. (2024). *World energy outlook 2024*.

Ingersoll, L. R., & Plass, H. J. (1948). Theory of the ground pipe heat source for the heat pump. *Heating, Piping and Air Conditionning*, 119.

Jalaluddin, Miyara, A., Tsubaki, K., Inoue, S., & Yoshida, K. (2011). Experimental study of several types of ground heat exchanger using a steel pile foundation. *Renewable Energy*, *36*(2), 764–771. https://doi.org/10.1016/j.renene.2010.08.011

Jansen. (2025). *Maximum performance. Safety guaranteed. Jansen powerwave coax*. Retrieved October 30, 2025, from www.jansen.com

Katzenbach, R., Clauss, F., Waberseck, T., & Wagner, I. (2008). Coupled numerical simulation of geothermal energy systems. *International Association for Computer Methods and Advances in Geomechanics (IACMAG)*.

Kilfrost. (2025). *Kilfrost-Geo: Designed to increase performance and safety*. Retrieved October 30, 2025, from www.kilfrost.com

Kong, G. qiang, Cao, T., Hao, Y. hu, Zhou, Y., & Ren, L. wei. (2021). Thermomechanical properties of an energy micro pile-raft foundation in silty clay. *Underground Space (China)*, *6*(1), 76–84. https://doi.org/10.1016/j.undsp.2019.09.005

Kundu, P. K., Coren, I. M., & Dowling, D. R. (2012). *Fluid mechanics* (5th ed.). Academic press. www.AnnualReviews.org.

Laloui, L., Nuth, M., & Vulliet, L. (2006). Experimental and numerical investigations of the behaviour of a heat exchanger pile. *International Journal for Numerical and Analytical Methods in Geomechanics*, *30*(8), 763–781. https://doi.org/10.1002/nag.499

Lautkankare, R., Salomaa, N., Martinkauppi, B., & Slobodenyuk, A. (2020). Underground parking lot at Turku market square - Zero energy parking hall and the biggest solar energy storage in the world. *E3S Web of Conferences*, *172*, 16008. https://doi.org/10.1051/e3sconf/202017216008

Loveridge, F., Brettmann, T., Beck, A. H., & Powrie, W. (2014, May). Assessing the applicability of thermal response testing to energy piles. *Global Perspectives on the Sustainable Excecution of Foundation Works*. http://eprints.soton.ac.uk/id/eprint/361725

Loveridge, F., McCartney, J. S., Narsilio, G. A., & Sanchez, M. (2020). Energy geostructures: A review of analysis approaches, in situ testing and model scale experiments.

Geomechanics for Energy and the Environment, *22*. https://doi.org/10.1016/j.gete.2019.100173

Lupattelli, A., Bourne-Webb, P. J., Bodas Freitas, T. M., & Salciarini, D. (2023). A Numerical study of the behavior of micropile foundations under cyclic thermal loading. *Applied Sciences (Switzerland)*, *13*(17). https://doi.org/10.3390/app13179791

Martin. Ziegler, David. Koppman, Renate. Pechnig, & D.N. Knapp. (2019). Energy sheet pile walls – Experimental and numiercal investigation of innovative energy geostructures. *Proceedings of the XVII ECSMGE-2019* . https://api.semanticscholar.org/CorpusID:204266509

Maatouk, C. (2016, July). Improvement of thermal conductivity of grout mixture for geothermal heat pump systems. *16th International Refrigeration and Air Conditioning Conference*. http://docs.lib.purdue.edu/iracc

Magnussen, E., Lin Tuv, R., Klincaraite, J., Erichsen, K. A., Bakken, J. E., Karlsen, P., & Vågenes, S. (2024). *Field and laboratory investigations geotechnical investigation report NTNU campus Dragvoll Tiller-Flotten*.

McCartney, J. S., & Murphy, K. D. (2017). Investigation of potential dragdown/uplift effects on energy piles. *Geomechanics for Energy and the Environment*, *10*, 21–28. https://doi.org/10.1016/j.gete.2017.03.001

Mimouni, T., & Laloui, L. (2015). Behaviour of a group of energy piles. *Canadian Geotechnical Journal*, *52*(12), 1913–1929. https://doi.org/10.1139/cgj-2014-0403

Nagano, K. (2007). 6. Energy pile system in new building of Sapporo city university. In *Thermal Energy Storage For Sustainable Energy Consumption* (Vol. 234). https://doi.org/https://doi.org/10.1007/978-1-4020-5290-3_16

Norsk Klimaservicesenter. (2022, April). *Climate profile Sør-Trøndelag*. https://klimaservicesenter.no/kss/klimaprofiler/sor-trondelag

Ogunleye, O., Singh, R. M., Cecinato, F., & Chan Choi, J. (2020). Effect of intermittent operation on the thermal efficiency of energy tunnels under varying tunnel air temperature. *Renewable Energy*, *146*, 2646–2658. https://doi.org/10.1016/j.renene.2019.08.088

Olgun, C. G., Ozudogru, T. Y., Abdelaziz, S. L., & Senol, A. (2015). Long-term performance of heat exchanger piles. *Acta Geotechnica*, *10*(5), 553–569. https://doi.org/10.1007/s11440-014-0334-z

Pal, S., Malviya, S. K., Pal, S. K., & Samantaray, A. K. (2009). Optimization of quality characteristics parameters in a pulsed metal inert gas welding process using grey-based Taguchi method. *International Journal of Advanced Manufacturing Technology*, *44*(11–12), 1250–1260. https://doi.org/10.1007/s00170-009-1931-0

Park, H., Lee, S. R., Yoon, S., & Choi, J. C. (2013). Evaluation of thermal response and performance of PHC energy pile: Field experiments and numerical simulation. *Applied Energy*, *103*, 12–24. https://doi.org/10.1016/j.apenergy.2012.10.012

Peace, G. S. (1993). *Taguchi methods: a hands-on approach*. Addison-Wesley.

Poulos, H. G., Carter, J. P., & Small, J. C. (2001). Foundations and retaining structures - research and practice. *In Proceedings of the 15th International Conference on Soil Mechanics and Foundation Engineering* (Vol. 4, pp. 2527-2606).

Prodan, I., Bujor, O., Popa, A., & Ban, H. (2020). A case study of isolated foundations on energy piles - from design to implementation. In *Challenges and innovations in geomechanics* (Vol. 126, pp. 1085–1092).

Ren, L. wei, Xu, J., Kong, G. qiang, & Liu, H. long. (2020). Field tests on thermal response characteristics of micro-steel-pipe pile under multiple temperature cycles. *Renewable Energy*, *147*, 1098–1106. https://doi.org/10.1016/j.renene.2019.09.084

REN21. (2022). *Renewable 2022 global status report*.

Ronchi, F., Salciarini, D., Cavalagli, N., & Tamagnini, C. (2018). Thermal response prediction of a prototype Energy Micro-Pile. *Geomechanics for Energy and the Environment*, *16*, 64–82. https://doi.org/10.1016/j.gete.2018.07.001

Rotta Loria, A. ., & Laloui, L. (2017). Thermally induced group effects among energy piles. *Géotechnique*, *67*(5), 374–393.

RS online. (2025). *Correge PT100 RTD Sensor, 3mm Dia, 30mm Long, 4 Wire, Probe, Classe A +250°C Max*. Retrieved June 24, 2025, from https://benl.rs-online.com/web/p/rtd-sensors/3706571

RS online. (2025). *RS PRO PT100 RTD Sensor, 6mm Dia, 50mm Long, 3 Wire, G1/2, Class A +250°C Max*. Retrieved June 24, 2025, from https://uk.rs-online.com/web/p/rtd-sensors/2000593

Sabatini, P. J., Tanyu, B., Armour, T., Groneck, P., & Keeley, J. (2005). *Micropile design and construction reference manual*.

Sadeghi, H., Ijaz, A., & Singh, R. M. (2022). Current status of heat pumps in Norway and analysis of their performance and payback time. In *Sustainable Energy Technologies and Assessments* (Vol. 54). Elsevier Ltd. https://doi.org/10.1016/j.seta.2022.102829

Salciarini, D., Ronchi, F., Cattoni, E., & Tamagnini, C. (2015). *Thermomechanical Effects Induced by Energy Piles Operation in a Small Piled Raft*. https://doi.org/10.1061/(ASCE)

Salciarini, D., Ronchi, F., & Tamagnini, C. (2017). Thermo-hydro-mechanical response of a large piled raft equipped with energy piles: a parametric study. *Acta Geotechnica*, *12*(4), 703–728. https://doi.org/10.1007/s11440-017-0551-3

Sani, A. K., Singh, R. M., Tsuha, C. de H. C., & Cavarretta, I. (2019). Pipe–pipe thermal interaction in a geothermal energy pile. *Geothermics*, *81*, 209–223. https://doi.org/10.1016/j.geothermics.2019.05.004

Sanner, B., Hellström, G., Spitler, J., & Gehlin, S. (2005). Thermal response test, current status and world-wide application. *Proceedings World Geothermal Congress*, 24–29.

Separatus AG. (2025). *Separatus, the simple smart system*. Retrieved October 30, 2025, from www.separatus.ch

Separatus AG. (2025). *Data sheet BHE, Technical data*. Retrieved October 30, 2025, from www.separatus.ch

Sethi, R., & Casasso, A. (2020). Volume II: Low Enthalpy Geothermal Energy. In *Volume II: Low Enthalpy Geothermal Energy*. https://doi.org/10.3390/books978-3-03936-285-1

Simonhjell, J. S. (2024). *Quick clay indication and soil stratigraphy studies using R-CPTU: investigating efficiency and limitations*.

Sisgeo. (2025). *Temperature gauges. Strain gauges and thermometers*. Retrieved October 30, 2025, from www.sisgeo.com

Sisgeo. (2025). *Vibrating wire strain gauges and rebars. User manual*. Retrieved October 30, 2025 from www.sisgeo.com

Śliwa, T., Kowalski, T., Stryczek, S., Wiśniowski, D., Bieda, A., Piwowarczyk, S., Beszłej, J., Naklicki, M., & Sapińska-Śliwa, A. (2017). The impact of graphite on the thermal conductivity of solidified grout. *AGH Drilling, Oil, Gas*, *33*(4), 811. https://doi.org/10.7494/drill.2017.34.4.811

Suryatriyastuti, M., Mroueh, H., Burlon, S., & Habert, J. (2013). Numerical analysis of the bearing capacity of thermoactive piles . In L. Laloui & A. Di Donna (Eds.), *Energy Geostructures* (pp. 139–155). https://doi.org/https://doi.org/10.1002/9781118761809.ch7

Sutman, M., Guney Olgun, C., Brettmann, T., & Student, P. D. (2015). *Full-Scale Field Testing of Energy Piles*.

Sutman, M., Speranza, G., Ferrari, A., Larrey-Lassalle, P., & Laloui, L. (2020). Long-term performance and life cycle assessment of energy piles in three different climatic conditions. *Renewable Energy*, *146*, 1177–1191. https://doi.org/10.1016/j.renene.2019.07.035

Tomlinson, M., & Woodward, J. (2015). *Pile design and construction practice* (sixth).

Tveito, O. E., & Lundstad, E. (2016). *Homogenization of daily mean temperature in Norway*.

UNEP. (2021). *2021 Global status report for buildings and construction: towards a zero-emission, efficient and resilient buildings and construction*. www.globalabc.org.

UNEP. (2025). *Global status report for buildings and construction 2024/2025*. United Nations Environment Programme. https://doi.org/10.59117/20.500.11822/47214

Varmeshop. (2025). *HX 35 ethylene glycol/cold carrier alcohol 25 liters for boreholes etc.* Retrieved June 20, 2025, from www.varmeshop.no

Viggiani, C., Mandolini, A., & Russo, G. (2012). *Piles and Pile Foundations*.

Yimsiri, S., & Ratananikom, W. (2025). Evaluation of ultimate pile capacity based on non-failed load tests: A case study of piles in Bangkok subsoil. *KSCE Journal of Civil Engineering*, *29*(7). https://doi.org/10.1016/j.kscej.2024.100153

You, S., Cheng, X., Guo, H., & Yao, Z. (2014). In-situ experimental study of heat exchange capacity of CFG pile geothermal exchangers. *Energy and Buildings*, *79*, 23–31. https://doi.org/10.1016/j.enbuild.2014.04.021

Yozy Kepdib, M. F., Singh, R. M., Madiai, C., & Facciorusso, J. A. (2025). Heating and cooling geothermal systems in urban settings: The potential of energy micropiles. In *Renewable and Sustainable Energy Reviews* (Vol. 208). Elsevier Ltd. https://doi.org/10.1016/j.rser.2024.114966

Yozy Kepdib, M. F., Singh, R. M., Madiai, C., & Facciorusso, J. A. (2025). Numerical study of the thermal performance of three different energy micropiles in hot climates. *Renewable Energy*, *249*. https://doi.org/10.1016/j.renene.2025.123188

Zhang, C., Guo, Z., Liu, Y., Cong, X., & Peng, D. (2014). A review on thermal response test of ground-coupled heat pump systems. *Renewable and Sustainable Energy Reviews*, *40*, 851–867. https://doi.org/10.1016/j.rser.2014.08.018

APPENDIX

Specifications and Compliance Certificate

***WE HEREBY CERTIFIED** that the manufactured instruments listed below,*
in the amount specified in the TABLE A, and furnished to

Customer	**NORWEGIAN UNIVERSITY OF SCIENCE AND TECHNOLOGY - NTNU**		
Address	**Department of Civil and Environmental Engineering Hogskoleringen 7a 7491 Trondheim**		
Reference Sisgeo Job No.:	**OV24-00646**	*Data:*	**18/06/24**

Complies with International System of Units (SI) and with all aspects of the requirements and specifications of your

Purchase Order / Contract	**No:e-mail**	**Ref.:Rao Martand Singh**

***WE FURTHER CERTIFY** that the items listed in the TABLE A have been manufactured, tested and calibrated in compliance with the relevant specifications and drawings, according to the CERTIFIED Quality System of Sisgeo, in conformance to the standards UNI EN ISO 9001, with reference to the following documents:*

IST09/02	**Standard practice for cable sealing**	**IST10/20**	**Standard practice for acceptance**
IST10/34	**Standard practice for VW gauges temperature aging process**	**IST10/55**	**Standard practice for assembly**
IST15/07	**Standard practice for packaging**		

" TABLE A "

Instrument Description	**VW EMBEDMENT STRAIN-GAUGE**		
Model	**0VK4200VC00**	*Quantity*	**30**
Serial Number		*Batch Number*	27/24
Country of Origin	**ITALY-EC**	*Traceable to*	**IST 8/01**
OUTFIT *Model*	*Serial Number*	*Equipment Description*	

Gauge Factor	**3.814**
Wiring	**Red/Black = Gauge - White/Green = Thermistor**

TECHNICAL SPECIFICATIONS

***WE FURTHER CERTIFY** that the technical specifications of the instruments are in accordance to the last revision of the relative technical data sheet consultable on our web site https://www.sisgeo.com/it/, if available*

SISGEO S.r.L.	*Production*	*Product Quality Engineer*	*Data:24/07/2024*

EU Declaration of Conformity

We

Manufacturer:	SISGEO S.r.l. Via F. Serpero, 4/F1 20060 MASATE (MI) – ITALY
Telephone number:	+39-02-95764130
E-mail address:	info@sisgeo.com

declare under our sole responsibility that the following equipment

Object of declaration	VW EMBEDMENT STRAIN-GAUGE
Model:	0VK4200VC00
Batch	27/24
Serial number:	
Reference Sisgeo Job No.:	**OV24-00646**

Intended use:

Vibrating wire strain gauges provide measurements of strain in steel or concrete. The measurements are used to calculate structural loads or stresses.

Is in conformity with the essential requirements of the following directives:

ROHS Directive 2015/863/UE

EMC Directive 2014/30/EU

The product has been tested according to the following standards or technical specifications:

EN IEC 63000:2018
EN 61326-1 (2013)

Notified body (where applicable):	☒ **Not applicable** ☐ **Applicable**

Signed for and on behalf of:

Masate	**24/07/2024**	[signature]
City	**Date**	**Romano Lamperti, CEO**

COMPANY WITH QUALITY SYSTEM CERTIFIED BY DNV ISO 9001

SISGEO S.r.l.
Via F. Serpero, 4/F1
20060 Masate – (MI)
Italia

Tel.+39-02 95764130
Fax +39-02 95762011
E-mail:info@sisgeo.com
http://www.sisgeo.com

Cap. Soc. 99.000 Euro int.versato
Cod. Fisc. e P.IVA. n. 10732420152
VAT No.:IT 10732420152
Trib. Milano: 333230 - REA: 1413159

La borsa di dottorato è stata cofinanziata con risorse del
Programma Operativo Nazionale Ricerca e Innovazione 2014-2020, risorse FSE REACT-EU
Azione IV.4 “Dottorati e contratti di ricerca su tematiche dell’innovazione”
e Azione IV.5 “Dottorati su tematiche Green”